

7. SITE 977¹

Shipboard Scientific Party²

HOLE 977A

Date occupied: 2315, 8 June 1995
Date departed: 1430, 15 June 1995
Time on hole: 6 days, 15 hr, 15 min
Position: 36°01.907'N, 1°57.319'W
Drill pipe measurement from rig floor to seafloor (m): 1995.5
Distance between rig floor and sea level (m): 11.54
Water depth (drill pipe measurement from sea level, m): 1984.0
Total depth (from rig floor, m): 2594.0
Penetration (m): 598.5
Number of cores (including cores having no recovery): 63
Total length of cored section (m): 598.5
Total core recovered (m): 545.49
Core recovery (%): 91.14
Oldest sediment cored:
Depth (mbsf): 550.4 (Core 58X)
Nature: Clay
Age: middle Miocene
Hard rock:
Depth (mbsf): 550.4–598.5
Nature: Volcanic pebbles

Principal results: Site 977 (proposed Site Alb-4a) is located south of Cabo de Gata in the Eastern Alboran Basin, halfway between the Spanish and Algerian coasts, at a water depth of 1984 m. The site is to the south of the Al-Mansour Seamount in a 36-km-wide graben that is bounded by the Yusuf Ridge to the south and the Maimonides Ridge to the north. Seismic records at Site 977 show a lower sequence of tilted and hummocky reflectors with several internal unconformities. This sequence likely represents synrift sediments that filled the graben and is overlain by uniform, mostly horizontally layered Pliocene–Pleistocene sediments. Our main drill objective was to penetrate and sample the unconformity between these two seismic units, at about 650 mbsf, which was suspected to represent both the seismic “M”-reflector and the bottom of the “postrift” sequence. Paleooceanographic objectives included documentation of the Atlantic-Mediterranean water exchange from the Miocene to the Pleistocene and productivity patterns in the Eastern Alboran Sea. Productivity fronts develop today along the path of Atlantic water inflow and have possibly changed their position and intensity during the past as the pattern of water circulation changed.

Site 977 penetrated 598.5 m of Miocene?–Pliocene to Holocene sediments. The Pliocene/Pleistocene boundary is at 266.95 mbsf. The lowermost section of Site 977 not only contains Pliocene planktonic foraminifer marker species but also uppermost Miocene nannofossil marker species.

Thus, the biostratigraphic data are not conclusive as to whether the Miocene/Pliocene boundary was reached at this site. A short hiatus occurred in the lower Pliocene (Zones NN13, MPL3–MPL2) between 490.59 and 490.63 mbsf. Benthic foraminifers comprise <1%–2% of the total foraminiferal assemblage. The presence of frequently abraded shelf taxa suggests contamination through rare downslope sediment transport. Average sedimentation rates at Site 977 are 154 m/m.y for the Pleistocene–Holocene and 96 m/m.y. for the Pliocene.

The sedimentary sequence recovered at Site 977 was subdivided into two lithostratigraphic units based on downhole changes in sedimentary structure and grain size.

Unit I (0–532.9 mbsf). Unit I contains Pliocene–Pleistocene sediments that comprise an open-marine, hemipelagic facies. The sediments consist predominantly of nannofossil clay to nannofossil-rich silty clay and are slightly to moderately bioturbated throughout (*Chondrites*, *Planolites*, *Zoophycos*). Carbonate content ranges between 21% and 61%. The carbonate fraction consists of nannofossils (70%), micrite (19%), bioclasts (6%), and foraminifers (5%). Minor lithologies include diatom and nannofossil oozes, and nannofossil-rich diatomaceous sandy silty clay. Sand- and silt-rich layers are intercalated with the clay-rich sediments. Sharp basal contacts are common. Intervals of slumping are found throughout the unit.

Thirty-nine organic-rich layers (ORLs) occur in Unit I some of which resemble sapropels recovered at previous Sites 974 and 975. ORLs are greenish in color and exhibit low magnetic susceptibilities. Organic carbon contents of ORLs vary between 0.8% and 1.5%, carbon concentrations >2% are measured for some discrete ORLs (sapropels?). The appearance of ORLs at Site 977 is important in that it suggests that organic-rich sedimentation occurred basin-wide in the western Mediterranean and organic carbon concentrations in some ORL reach levels that are similar to those found in eastern Mediterranean sapropels. Smear-slide analysis shows that ORLs are enriched in opaque minerals and, locally, micrite. Fe-bearing, Mn-rich dolomite (kutnohorite, up to 30%) or siderite occurs at the top of many ORLs.

Unit I has been further subdivided into three subunits based on changes in sedimentary structure.

Subunit IA (Hole 977A, 0.0–417.4 mbsf). Visible structure in Subunit IA sediments is minimal. Five minor slump intervals occur in this subunit with associated intraclastic breccias. The breccias show inverse to normal grading with angular to subrounded clasts ranging to pebble-size. Color banding and mottling are developed in sediments above and below the slumped intervals.

Subunit IB (417.4–490.6 mbsf). The subunit contains parallel and cross-laminated to bedded clays with frequent slumps and intraclastic breccias. It is Pliocene in age and represents an open-marine, hemipelagic facies. Zones of intense burrowing can be found throughout the unit, predominantly of *Zoophycos* and *Planolites*. Slumps are recognized from folding of fine laminations. The base of this subunit is just below a hiatus spanning at least lower Pliocene Zone NN13.

Subunit IC (490.6–532.9 mbsf). This subunit contains few sedimentary structures, laminations are rare, and soft sediment deformation has not been recognized. Bioturbation (*Zoophycos*, *Chondrites*, *Planolites*) ranges from slight to intense.

Unit II (532.9–598.5 mbsf). This unit comprises partly cemented sandy gravel that is of Lower Pliocene to Miocene? age. Recovery was

¹Comas, M.C., Zahn, R., Klaus, A., et al., 1996. *Proc. ODP, Init. Repts.*, 161: College Station, TX (Ocean Drilling Program).

²Shipboard Scientific Party is given in the list preceding the Table of Contents.

less than 1%, with only 2 cm of granule-rich sand and 40 cm of gravel recovered from a cored interval of 57.8 m. The gravel consists predominantly of volcanic clasts (rhyodacite and rare shoshonitic to calc-alkaline basalt/andesite) and few sedimentary clasts (dolomitic mudstone and quartz sandstone cemented by quartz and chlorite). These are coated by a calcareous cement suggesting that the clasts have been derived from the partly cemented sandy gravel.

Log data at Site 977 were acquired using quad combo and Formation MicroScanner (FMS). From 140 to 323 mbsf, the borehole was out of caliper (washed out). The FMS was run below this interval and obtained excellent images in the lower part of the hole including the transition zone between clays and sandy conglomerates. After post-cruise processing, the logs will provide information about the lithology and structure of the gravel/sand interval below 531 mbsf in which core recovery was extremely low.

Sediments at Site 977 average 0.5% total organic carbon (TOC) and may reach 2.5% in organic-rich layers (ORLs). Organic C/N ratios of 28 ORLs containing a minimum of 1% TOC average 10.1, which is a value intermediate between unaltered algal organic matter and fresh land-plant material. These organic-carbon-rich sediments likely contain partially degraded algal material with some admixed continental organic matter. Rock-Eval and elemental source characterization suggests that marine organic matter in ORLs has been heavily oxidized. Rock-Eval T_{max} values indicate that organic matter in the upper section is thermally immature with respect to petroleum generation, whereas it is overmature in the deeper sediments. From this we infer that heat flow was higher in the past at Site 977.

Concentrations of headspace methane are high at Site 977. The source of the methane is probably from in situ microbial fermentation of marine organic matter. Concentrations of propane, *iso*-butane, and *iso*-pentane exceed those of ethane in sediments from about 200 to 450 mbsf. C_3 , C_4 , and C_5 gases were likely produced by thermal degradation of sedimentary organic matter during some former period of elevated heat flow at this site.

Interstitial water profiles at Site 977 are dominated by organic matter degradation and carbonate diagenesis. Rapid sediment accumulation rates at this site ensured that organic matter was buried more rapidly than dissolved oxygen can diffuse from the overlying seawater. Calcium and magnesium decrease in a zone of increased alkalinity suggesting that dolomite or high magnesium calcite has precipitated from solution. Silica increases rapidly in the upper few meters, then gradually decreases with depth except for a peak at 103.45 mbsf, which likely comes from dissolution of diatomaceous ooze at 117.50 mbsf. Pore-water salinity remains below seawater concentrations until 362.30 mbsf, then increases to 46 g/kg at 506.50 mbsf. Lithium concentrations increase from surface concentrations to 202 μ M at 477.70 mbsf. This may reflect a lateral migration of evaporitic brines from another region of the basin.

Downhole temperature and shipboard thermal conductivity measurements give a heat flow of 102 mW/m². This value is comparable to the range of 97–112 mW/m² in the region around Site 977.

Magnetic inclinations are mostly positive at Site 977. Some negative inclinations are recorded but declinations remain constant in these sections compared to those with positive inclination. This suggests that a strong overprint obscures the magnetic signal at this site. Therefore it was not possible to obtain a magnetostratigraphy at Site 977.

Changes in susceptibility in the upper 60 mbsf are possibly due to higher concentrations of terrigenous components. Thermal conductivity is between 1.0 and 1.5 W/(m·K). Bulk density, porosity, and void ratio increase rapidly with depth in the uppermost 50 mbsf, and at a slower rate below that.

The post-Messinian stratigraphy established at Site 977 will provide time control on the seismic facies in the Eastern Alboran Sea. This will yield information on the timing of extensional structures identified in seismic data, and on the tectonic subsidence history of the basin. The seismic line acquired by the *JOIDES Resolution* during the site approach shows that the Pleistocene deposits recovered at this site are faulted. The stronger

seismic reflector recognized in the area likely corresponds to the gravel-bearing interval that has been sampled at 598.5 mbsf. This seismic reflector correlates with the top of Messinian evaporites ("M"-reflector) at Sites 974 and 975. Drilling results at Site 977 suggest that in the Eastern Alboran Basin the "M"-reflector corresponds to a strong erosional event, possibly from the flooding of the Mediterranean during the early Pliocene.

The recovery of organic-rich layers at Site 977 is an intriguing discovery, in that intervals with organic carbon concentrations that, in some cases, reach levels found in sapropels from the eastern Mediterranean are now documented across the western Mediterranean Sea. Establishing the timing of these events and coeval environmental conditions at Site 977 in relation to those at previous Sites 974 and 975 in the Tyrrhenian and Balearic Seas will yield information on physical and biogeochemical boundary conditions in the western Mediterranean during these periods.

BACKGROUND AND OBJECTIVES

Sites 977 and 978 (24 km apart) are located in the Eastern Alboran Basin (EAB), south of the Cabo de Gata, midway between the Spanish and Algerian coasts (Fig. 1). These sites are situated about 90 km east-northeast of the Alborán Island, in a 36-km-wide graben bounded by the Yusuf Ridge to the south and the Maimonides Ridge to the north. The graben widens toward the South Balearic Basin to the east. Al-Mansour Seamount, an elliptical and isolated volcanic high, lies in the center of the graben, dividing it into two east-west-trending sub-basins. Sites 977 and 978 lie south and north of the Al-Mansour Seamount in these sub-basins in water depths of 1984 m and 1942.4 m, respectively (Figs. 1, 2).

The position of the sites was selected on *Conrad* Line 823 from the preexisting site-survey data (Watts et al., 1993). During the site approach, a *JOIDES Resolution* geophysical survey was made and Site 977 positioned at 1740 hr (June 8) on this seismic profile (see "Underway Geophysics" chapter, this volume), near the intersection with *Conrad* multichannel seismic line 823. Site 978 was drilled at shotpoint 2442 of the same seismic line 823 (Fig. 3).

The EAB appears to have a different structural pattern than the Western Alboran Basin (WAB). The EAB is underlain by Miocene to Holocene east-west or southeast-northwest-trending basement ridges and basins, and it seems to be affected by folding and strike-slip tectonics from the late Miocene to the Pleistocene (Fig. 4). Seismic data document that the EAB has thinner, and probably younger, sedimentary fill, and exhibits fewer obvious extensional structures than the WAB. The region has also experienced a post-late-Miocene compressive reorganization (see "Introduction" chapter, this volume). The EAB has been interpreted by some (Platt and Vissers, 1989; Comas et al., 1992) to have formed from rifting and crustal extension, which may have started when the region was still above sea level (Watts et al., 1993). Others have interpreted the EAB as originating from Miocene crustal-level strike-slip faulting (de Larouzière et al., 1988). Seismic data indicate the existence of very recent folding and strike-slip faulting that deforms the present seafloor and has created small pull-apart basins (Maufrett et al., 1987; Comas et al., 1992; Maufrett et al., 1992; Woodside and Maldonado, 1992; Watts et al., 1993).

Sites 977 and 978 were selected because seismic profiles show a lower sequence of tilted, hummocky reflectors with several internal unconformities. This sequence may represent synrift sediments that filled the graben. This tilted sequence is overlain by relatively uniform, mostly flat-layered reflectors, which may correspond to Pliocene–Pleistocene sediments. Our main objective was to penetrate and sample the unconformity between these two seismic units. This unconformity is suspected to be the "M"-reflector that lies at about 650 mbsf (Fig. 3). Other primary objectives included sampling synrift sediments to determine the age and nature of the internal unconformities as well as the relative proportions of synrift and postrift

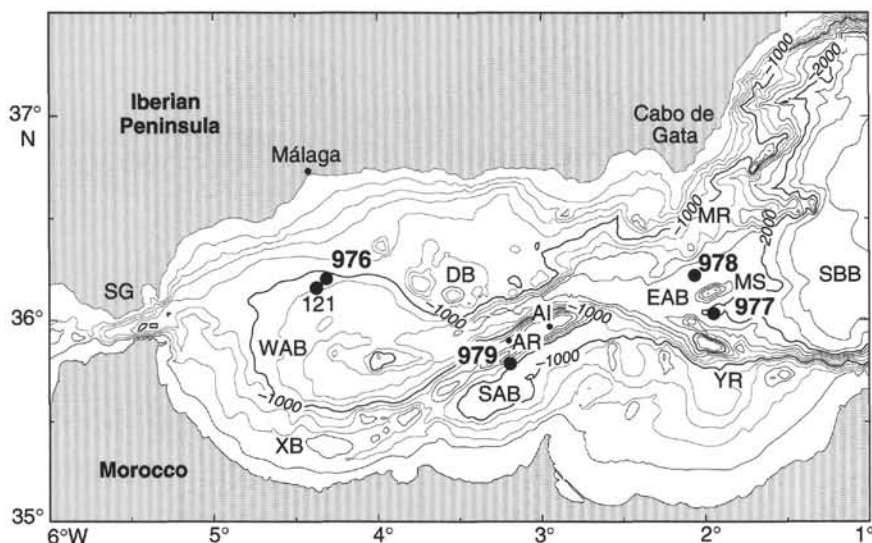


Figure 1. Location of Leg 161 Sites 976, 977, 978, 979, and DSDP Site 121 in the Alboran Sea. Contours in meters, contour interval is 200 m. AI = Alborán Island, AR = Alboran Ridge, DB = Djibouti Bank, EAB = Eastern Alboran Basin, MR = Maimonides Ridge, MS = Al-Mansour Seamount, SAB = Southern Alboran Basin, SBB = South Balearic Basin, SG = Strait of Gibraltar, WAB = Western Alboran Basin, XB = Xauen Bank, YR = Yusuf Ridge.

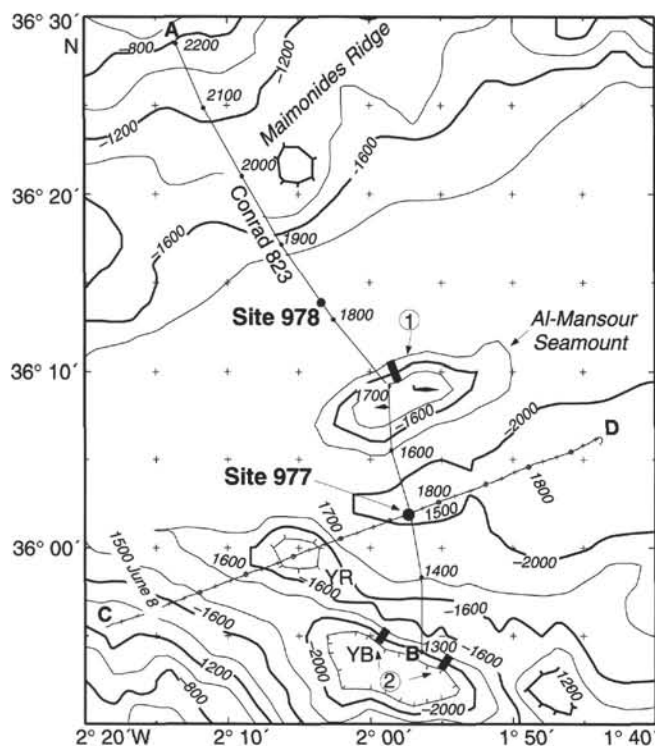


Figure 2. Close-up of Figure 1 showing position of Sites 977 and 978. Multi-channel seismic reflection line *Conrad 823* (A–B, annotated in shotpoints) is shown in Figure 3 and *JOIDES Resolution* seismic profile (C–D, annotated in time) is included in the back-pocket foldout (Fig. 1 of “Underway Geophysics” chapter, this volume). Location of submersible *Cyana* dive sites CYA-5 and -6 (2) and CYA-7 (1) are shown. YR = Yusuf Ridge, YB = Yusuf Basin.

sediments. In addition, Sites 977 and 978 drilling results will permit more accurate seismic correlation of the Alboran Sea basin with the South Balearic Basin.

Migrated reflection profiles indicate that the basement cannot be clearly identified in the graben where Sites 977 and 978 are located. At these sites, there may be a substantial sedimentary section beneath the upper synrift units, and sampling basement is not practical. How-

ever, submersible sampling has provided information on the nature of the acoustic-basement highs that bound these sites. Samples taken by the submersible *Cyana* (CYANALBORAN cruise) from the basement escarpments on the northern sides of Al-Mansour Seamount and Yusuf Basin yield calc-alkaline to alkaline volcanic rocks (Comas et al., in press).

By drilling in the Eastern Alboran Sea we sought to determine:

1. The stratigraphy of the EAB sediment-fill, variation in sedimentation, sedimentary environment, and paleogeography. This will calibrate the stratigraphy to seismic facies to provide stratigraphic control and timing of extensional structures identified from seismic data. We also intend to correlate the sediments at Sites 977 and 978 with the sedimentary sequence cored at Site 976 in the WAB; this is not possible from seismic data as these basins are separated by structural highs.
2. The subsidence history of the EAB, when combined with seismic and commercial well data, can yield information about the magnitude of the extension and the relative proportions of syn-rift and post-rift subsidence, and the total subsidence. Comparing the subsidence histories of the WAB (Site 976) and the EAB (Sites 977 and 978) will have strong implications for constraining the tectonic and structural evolution for the entire Alboran Sea. Back-stripping of biostratigraphic data from commercial wells can constrain models that compare crustal thickness, based on seismic and gravity-anomaly data (Docherty and Banda, 1992; Watts et al., 1993). Comparison of the calculated and observed thicknesses should permit us to determine the initial thermal structure and elevation, and the processes that have modified the crust since rifting began. Comparing these data with back-stripped subsidence curves computed for onshore Betic Neogene basins (Cloetingh et al., 1992) will quantify the amount of extension for the Miocene Alboran Basin as a whole.
3. The nature and role of volcanism during the later structural reorganization of the basin. The age and chemistry of volcanic and volcanoclastic products within the sedimentary sequence, if any, will provide direct constraints on the thermal and structural evolution of the underlying mantle.
4. The extent of deformation in the basin during the postulated late Miocene to Holocene contractional reorganization that produced folding, strike-slip faulting, block rotation, and pull-apart structures, and contemporaneous Alboran Basin subsidence. Constraining the Pleistocene–Pliocene stratigraphy to

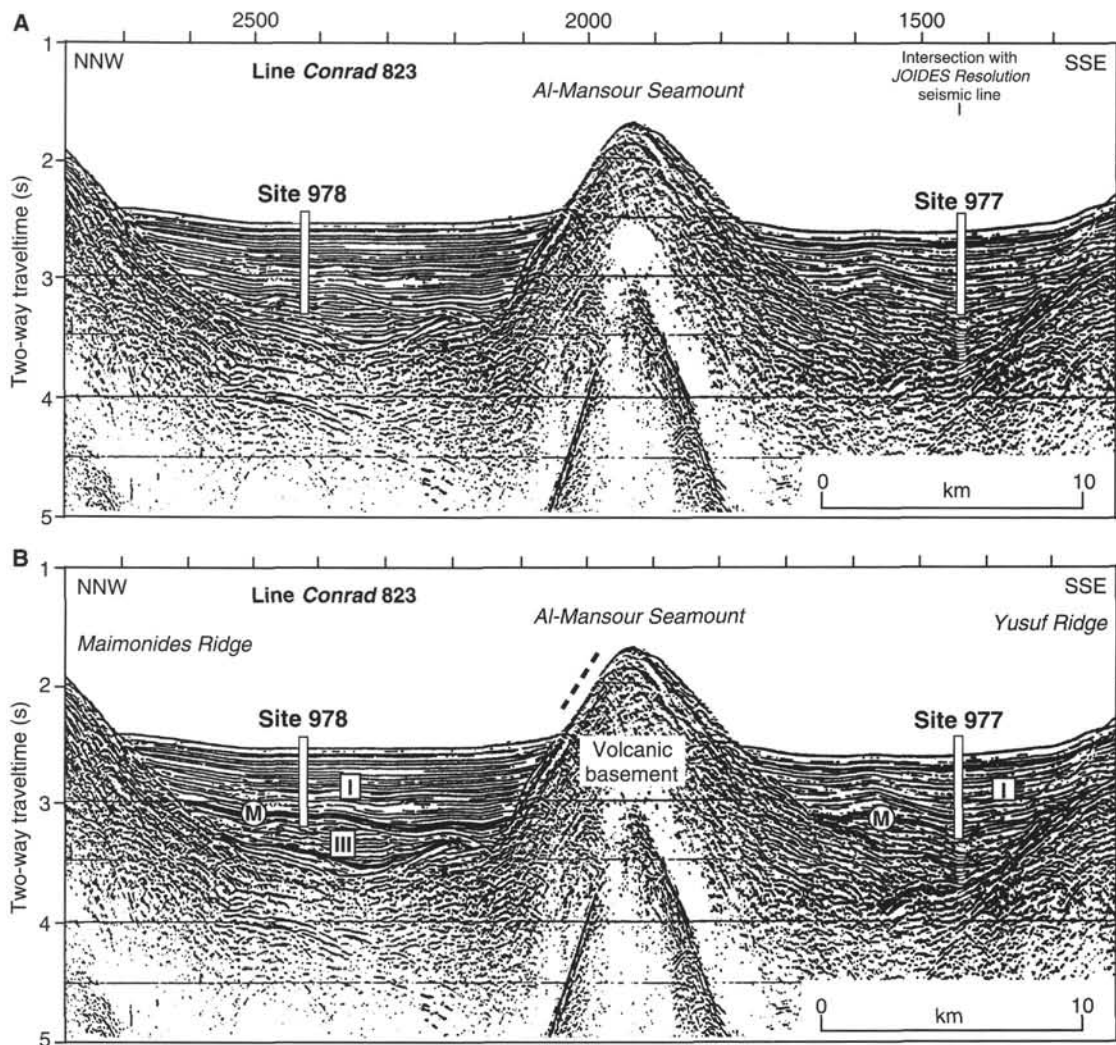


Figure 3. Location of Sites 977 and 978 on migrated MCS profile *Conrad 823*. Al-Mansour Seamount divides the graben into two sub-basins where Site 977 and Site 978 are located. **A.** Original seismic reflection profile. Intersection with the *JOIDES Resolution* single-channel line is shown. **B.** Interpreted profile based on seismic sequence analysis and stratigraphic subdivision proposed by Comas et al. (1992). (I and III are lithoseismic units from Comas et al., 1992; see "Introduction" chapter, this volume). M = top of Messinian, or "M"-reflector. Location of line shown is in Figure 2. Dashed line on the northern side of Al-Mansour Seamount shows approximate location of *Cyana-7* submersible sampling.

times of the later tilting and uplift of the volcanic ridges, and associated folding, will allow accurate interpretation of this latest stage of basin deformation.

5. The character of Atlantic-Mediterranean water exchange from the Miocene to the Pleistocene, also addressed at Site 976. In addition, productivity patterns in the EAB were to be documented at both sites. Today, productivity fronts develop in the EAB along the flow path of the Atlantic water inflow in response to seasonal temperature and wind-field fluctuations that determine regional biological productivity rates (Minas et al., 1991; Tintoré et al., 1995). Glacial-interglacial fluctuations in biological productivity have been inferred from paleoceanographic records throughout the Alboran Sea (Abrantes, 1988; Vergnaud-Grazzini and Pierre, 1991) and are likely driven by changes of water circulation and the intensity of associated productivity fronts. Export of nutrients contained in the eastward-flowing Atlantic surface current may have also influenced productivity patterns in the western Mediterranean. Monitoring the timing of productivity events in relation to similar events at Sites 974 and 975 in the Tyrrhenian and Bale-

aric Seas is therefore another important paleoceanographic objective.

OPERATIONS

Transit Site 976 to Site 977 (Alb-4A)

After the 99-nmi transit to Site 977 (~8 hr; ~12 nmi/hr), we conducted a seismic survey over the site. We then positioned the ship over Site 977 and deployed a beacon at 2315 hr, 8 June and a backup beacon at 0200 hr, 9 June. The elevation of the DES above sea level was 11.54 m for Hole 977A.

Hole 977A

We used the same APC/XCB BHA as had been run throughout the leg with a rerun Security S87F bit. Since the site was in close proximity to a communication cable, the VIT was deployed as a precautionary measure while spudding Hole 977A. Hole 977A was spudded at 1100 hr, 9 June. Core 977A-1H was taken at 1990.0 m and

Table 1. Site 977 coring summary.

Core	Date (June 1995)	Time (UTC)	Depth (mbsf)	Length cored (m)	Length recovered (m)	Recovery (%)
161-977A-						
1H	9	0915	0.0–4.0	4.0	3.97	99.2
2H	9	1005	4.0–13.5	9.5	9.88	104.0
3H	9	1115	13.5–23.0	9.5	10.11	106.4
4H	9	1250	23.0–32.5	9.5	9.93	104.0
5H	9	1330	32.5–42.0	9.5	9.89	104.0
6H	9	1420	42.0–51.5	9.5	10.13	106.6
7H	9	1505	51.5–61.0	9.5	10.03	105.6
8H	9	1545	61.0–70.5	9.5	10.01	105.3
9H	9	1640	70.5–80.0	9.5	10.23	107.7
10H	9	1720	80.0–89.5	9.5	9.97	105.0
11H	9	1815	89.5–99.0	9.5	10.10	106.3
12H	9	1915	99.0–108.5	9.5	10.20	107.3
13H	9	2015	108.5–118.0	9.5	9.93	104.0
14H	9	2045	118.0–127.5	9.5	10.10	106.3
15H	9	2140	127.5–137.0	9.5	10.12	106.5
16H	9	2215	137.0–146.5	9.5	10.09	106.2
17H	9	2300	146.5–156.0	9.5	10.03	105.6
18X	10	0000	156.0–165.6	9.6	9.87	103.0
19X	10	0200	165.6–175.2	9.6	9.86	103.0
20X	10	0245	175.2–184.9	9.7	9.91	102.0
21X	10	0430	184.9–194.4	9.5	9.89	104.0
22X	10	0530	194.4–204.0	9.6	9.87	103.0
23X	10	0630	204.0–213.6	9.6	9.86	103.0
24X	10	0715	213.6–223.2	9.6	6.73	70.1
25X	10	0805	223.2–232.9	9.7	9.91	102.0
26X	10	0855	232.9–242.6	9.7	9.59	98.8
27X	10	1005	242.6–252.2	9.6	9.93	103.0
28X	10	1135	252.2–261.8	9.6	9.86	103.0
29X	10	1315	261.8–271.4	9.6	9.85	102.0
30X	10	1450	271.4–281.0	9.6	9.87	103.0
31X	10	1625	281.0–290.5	9.5	9.91	104.0
32X	10	1825	290.5–300.1	9.6	9.92	103.0
33X	10	2000	300.1–309.7	9.6	9.65	100.0
34X	10	2214	309.7–319.4	9.7	9.93	102.0
35X	11	0010	319.4–328.9	9.5	9.92	104.0
36X	11	0200	328.9–338.5	9.6	9.88	103.0
37X	11	0330	338.5–348.2	9.7	9.85	101.0
38X	11	0515	348.2–357.9	9.7	9.89	102.0
39X	11	0645	357.9–367.5	9.6	9.86	103.0
40X	11	0830	367.5–377.1	9.6	9.90	103.0
41X	11	0950	377.1–386.7	9.6	9.81	102.0
42X	11	1125	386.7–396.4	9.7	9.89	102.0
43X	11	1245	396.4–406.0	9.6	9.90	103.0
44X	11	1350	406.0–415.6	9.6	9.83	102.0
45X	11	1505	415.6–425.3	9.7	9.83	101.0
46X	11	1645	425.3–434.9	9.6	9.83	102.0
47X	11	1815	434.9–444.5	9.6	9.92	103.0
48X	11	1950	444.5–454.1	9.6	9.89	103.0
49X	11	2140	454.1–463.7	9.6	9.93	103.0
50X	12	0000	463.7–473.3	9.6	9.96	104.0
51X	12	0130	473.3–482.9	9.6	6.29	65.5
52X	12	0330	482.9–492.5	9.6	10.00	104.1
53X	12	0445	492.5–502.1	9.6	9.95	103.0
54X	12	0620	502.1–511.8	9.7	9.90	102.0
55X	12	0810	511.8–521.4	9.6	9.96	104.0
56X	12	1030	521.4–531.0	9.6	9.87	103.0
57X	12	1145	531.0–540.7	9.7	1.90	19.6
58X	12	1330	540.7–550.4	9.7	0.00	0.0
59X	12	1620	550.4–560.0	9.6	0.05	0.5
60X	12	1830	560.0–569.6	9.6	0.23	2.4
61X	12	2030	569.6–579.2	9.6	0.07	0.7
62X	12	2330	579.2–588.9	9.7	0.02	0.2
63X	13	0500	588.9–598.5	9.6	0.03	0.3
Coring totals:				598.5	545.49	91.1

Note: See also detailed coring summary on the CD-ROM, back pocket, this volume.

came stuck again. We ran the quad combo and the FMS tool, but did not run the geochemical tool because there was difficulty re-entering the drillpipe with the FMS tool. Both logs were run to 564.5 mbsf (2560 m) and will help provide information about the extremely low-recovery interval below 531 mbsf.

After logging, we deployed a FFF. The VIT was used to observe the BHA being withdrawn from the seafloor to ensure that the FFF was not dragged out of the hole. The bit cleared the FFF at 0700 hr, 14 June 95. The RCB BHA was assembled and run to the seafloor. The BHA consisted of the same components as used at earlier sites, except that the jars, damaged during Hole 976E operations, were not

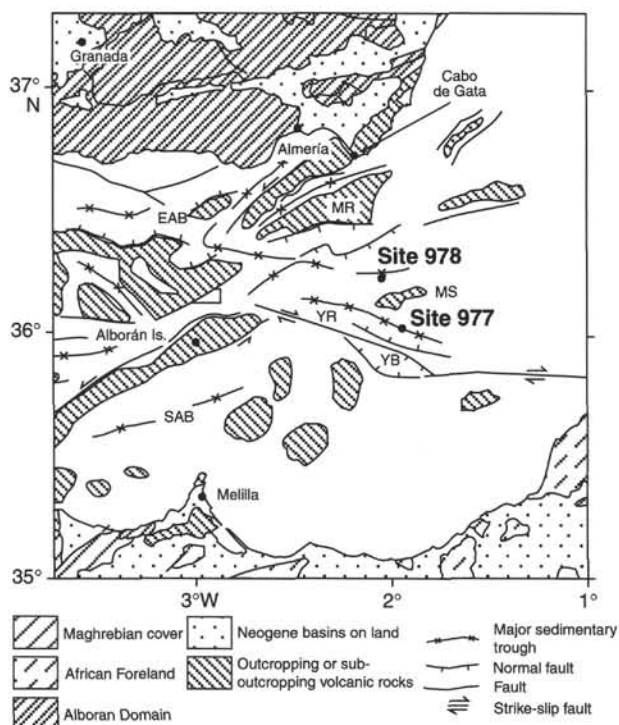


Figure 4. Tectonic sketch of the East Alboran Basin around Sites 977 and 978 (from Comas et al., 1993). Explanation for legend in "Introduction" chapter, this volume. YR = Yusuf Ridge; YB = Yusuf Basin; EAB = Eastern Alboran Basin; MS = Al-Mansour Seamount; SAB = Southern Alboran Basin, MR = Maimonides Ridge.

recovered 3.97 m; therefore, the seafloor was defined to be at 1984.0 mbsf. APC Cores 1H through 17H were taken to 156.0 mbsf (2151.5 mbrf) and recovered 164.72 m (106%; Table 1; see also detailed coring summary on the CD-ROM, back pocket, this volume). Cores 3H through 17H were oriented using the Tensor tool. ADARA temperature measurements were taken during Cores 3H, 6H, 9H, and 12H. Some core expansion was observed beginning with Core 12H. The maximum C_1 detected in the upper 156 mbsf was 35,695 ppm with a poorly defined second high of 31,564 at about 310 mbsf. No trends in the gas analyses caused safety concerns significant enough for us to consider abandoning the hole.

XCB Cores 977A-18X to 63X were taken from 156.0 to 598.5 mbsf (2151.5 to 2594.5 mbrf) coring 442.5 m and recovering 380.77 m (86.05%). From 156.0 to 531.0 mbsf, XCB recovery was over 100% in stiff, hard clay. Starting at Core 57X (531.0 mbsf), we encountered a conglomeratic interval (cobble, gravel, and sand) and recovery from 531.0 to 598.5 mbsf fell to less than 4%. Before allowing the whole BHA to penetrate this interval, we made a short wiper trip back up to 482.58 mbsf. Immediately after cutting the next core (63X), the pipe became stuck before the connection could be made and the core barrel withdrawn. We worked the pipe for over two hours until it finally became free. This zone seemed slightly over-pressured. When the mud pumps were turned off the pipe was worked free. It appeared that the added flow from the bit was causing the hole to pack off.

At this point, we decided to log instead of trying to fight the hole conditions since the bit had already accumulated over 86 hours and the weaker non-magnetic drill collar was in the BHA. Therefore, we made a wiper trip to 49.5 mbsf (2045 mbrf) and positioned the bit at this depth for logging. Fill was tagged at 578.5 mbsf (2574 mbrf), but we did not attempt to ream it out due to the BHA conditions described above and the amount of time that might be lost if the drill pipe be-

included. It took about 15 minutes to locate the funnel, which was reentered at 1800 hr, 14 June. Several attempts were needed to raise and lower the BHA until the original hole was found and the BHA could be lowered without bowing the pipe.

Once in the hole, the bit encountered fill at 533.21 mbsf (2523.21 mbrf). We then picked up the top drive and easily washed and reamed to 595.18 mbsf (2590.68 mbrf) in less than 2 hours. The last 3 m of fill, however, could not be penetrated without the drill pipe becoming stuck. Every time the bit was gently placed on top of the fill, the torque increased to 600–700 amps, rotation stopped, and pressure increased. We suspect that the hole was packing off, because the only way to free the pipe was by completely turning off the mud pumps. We spent over 8 hours attempting to ream out this last 3 m without success. During the last attempt, the weight indicator began fluctuating as if the bit was bouncing on the bottom. Since we were unable to advance, we decided to terminate the hole.

Before abandoning the site, we sent a request to ODP headquarters to offset from this hole, in the hope that moving out of the subsurface channel axis shown in seismic data might allow the bit to penetrate past this interval to the 1200 mbsf target depth. However, these offset locations were denied for safety concerns. Instead, we received approval for drilling close to Alb-4 (slightly modified to avoid drilling close to a submarine telecommunications cable). The bit cleared the seafloor at 1030 hr and cleared the rotary table at 1430 hr, 15 June. The two beacons were recovered while the pipe was being retrieved. After the BHA was recovered, we observed that one cone had broken off the new bit and that the welded collar around the location of the dogs on the MBR was heavily damaged. The rig floor was secured and we began the transit to ALB-4B (Site 978) at 1430 hr, 15 June.

LITHOSTRATIGRAPHY

The sedimentary sequence recovered at Site 977 has been subdivided into two lithostratigraphic units based on downhole changes in sedimentary structures and sediment grain size. Unit I has been further subdivided into three subunits (IA, IB, IC) based on association of sedimentary structures and specific lithologies (Table 2; Fig. 5). Subunit boundaries closely correspond with changes in physical properties (see "Physical Properties" section, this chapter). The boundary between Subunit IB and Subunit IC is marked by a hiatus encompassing at least part of NN13 Biozone.

Unit I

Hole 977A, 0.0–32.9 mbsf, Section 977A-1H-1, 0 cm, to Section 977A-57X-CC, 46 cm.

Unit I comprises 532.9 m of open marine, hemipelagic facies that is Pleistocene to early Pliocene in age. The dominant lithologies are nannofossil-rich to nannofossil and calcareous silty clay and clay. These sediment types are found in each of the subunits in Unit I.

Carbonate content (Fig. 6, see also "Organic Geochemistry" section, this chapter) of the dominant lithologies ranges between 21% and 76%, but most sediments have between 30% and 50% CaCO₃. Smear-slide analysis shows that the carbonate fraction comprises nannofossils (70%), micrite (20%), bioclasts (6%) and foraminifers (4%). Minor silt- to sand-sized, non-carbonate components in the major lithologies include quartz, feldspar, mica, diatoms, sponge spicules, organic matter, and opaque and accessory minerals. The content of terrigenous components (quartz + feldspar + mica fraction) in this unit is shown in Figure 7. Dolomite, ankerite and siderite were noted in smear-slide samples, and kutnohorite (CaMn(CO₃)₂) was identified by X-ray diffraction.

Minor lithologies in Unit I include diatom and nannofossil ooze, nannofossil-foraminifer clay and ooze, nannofossil-rich diatomaceous silty clay, and organic-rich layers (ORLs). ORLs com-

prise 8.5% of the stratigraphic section between the seafloor and the top of Core 977A-26X (232.9 mbsf). At least 40 ORLs are identified in Subunit IA (Table 3) on the basis of their greenish color, magnetic susceptibility and total organic-carbon content (TOC). The ORLs range in thickness from 3 cm to 363 cm. Some ORLs are similar to those at Sites 974 and 975 (see "Lithostratigraphy" sections, Site 974 and Site 975 chapters, this volume); two are depicted in Figures 8, 9. Others are more dispersed. The characteristic, low susceptibility signals of two ORLs are shown in Figure 10. The ORLs are classified as Types I through V according to their TOC. The less organic-carbon-rich Type III ORLs have TOCs about twice that of the background sediment (0.45%; Fig. 11). Smear-slide analyses of 28 of the ORLs show that they are calcareous silty clay and nannofossil-rich to nannofossil and calcareous clay. Relative to the background lithologies, ORLs are enriched in opaque minerals, organic matter and, locally, micrite. At the top of several ORLs, where maxima in magnetic susceptibility are present, kutnohorite is present (up to 30%) or siderite is found (Table 4).

Minor sand- and silt-rich lithologies are intercalated with the clay-rich sediments. Most of these are centimeter-scale layers; a few are laminae. Sharp basal contacts are common and scour-and-fill bases are present (Fig. 12). Load (sand pillow) structures are recognized at the base of several layers (Fig. 8). Some silty sand, sandy silt and silt layers show normal grading. Reverse grading was found in one instance. Smear slide examination of the sand-sized fraction indicates two broad compositions. The calcareous composition contains foraminifer-rich types with subordinate nannofossils, bioclasts, and terrigenous components. The siliciclastic composition comprises quartz-, feldspar-, mica-rich types with subordinate rock fragments, foraminifers and bioclasts. Siliciclastic sand-sized fractions are common in Pleistocene sediments at Site 977 (above 270.9 mbsf).

Subunit IA

Hole 977A, 0.0–417.4 mbsf, Core 977A-1H, 0 cm, to Section 977A-45X-2, 32 cm.

Subunit IA is characterized by common laminae and thin beds of foraminifer-rich sand and siliciclastic sand and by ORLs. Slight to moderate bioturbation also distinguishes Subunit IA. Slumps and associated intraclastic breccias are rarer than in Subunit IB.

There are few visible sedimentary structures in Subunit IA sediments; however, *Chondrites*, *Planolites*, and, less common, *Zoophycos* burrows are distinguishable. In intervals where burrowing is not clearer, disseminated pods of pyrite are interpreted to result from burrowing. Locally, burrows are completely pyrite filled. Color banding is rare and associated with either local concentrations of pyrite or soft-sediment deformation.

In Subunit IA, major and minor intervals of soft-sediment deformation (slumping), associated with levels of intraclastic breccia (Section 977A-11H-6, 19–99 cm and Section 977A-15H-5, 13–113 cm; Fig. 13), are present. Intraclastic breccias show inverse to normal grading with angular to subrounded clasts ranging to pebble-size. Color banding and mottling are developed in sediments above and below the slumped intervals.

The base of Subunit IA is located at the top of a slumped interval at 417.4 mbsf (Section 977A-45X-2, 32 cm), which in turn marks the top of an interval of parallel- and cross-laminated (centimeter-scale) clays.

Subunit IB

Hole 977A, 417.4–490.6 mbsf, Core 977A-45X, 32 cm, to Section 977A-52X-6, 21 cm.

Sedimentary structures and lithological association that characterize Subunit IB include alternations of nannofossil clay and calcareous clay laminae on the millimeter to centimeter scale (clay couplets),

Table 2. Lithostratigraphic units for Site 977.

Unit	Subunit	Series	Lithology	Sedimentary structures	Occurrence	Interval (mbsf)
I	IA	late Pliocene to Pleistocene	Major: Nannofossil clay Calcareous and nannofossil silty clay to clay Nannofossil-rich silty clay to clay	General: Bioturbation slight to moderate Laminae of foraminifer and siliciclastic sand to silt and silty clay Faint laminations	Core 977A-1H-1, 0 cm, to 45X-2, 32 cm	0.0–417.4
			Minor: Organic-rich layers (ORLs) Nannofossil ooze Diatom ooze Nannofossil-rich diatomaceous sandy silty clay Intraclastic breccia	Other: Soft sediment deformation (slumps) Some color banding		
	IB	early Pliocene to late Pliocene	Major: Nannofossil clay Calcareous silty clay to clay	General: Bioturbation moderate to intense Laminations Interbedded couplets	Core 977A-45X-2, 32 cm, to 52X-6, 21 cm	417.4–490.8
	IC	early Pliocene	Major: Nannofossil clay Calcareous silty clay to clay	General: Bioturbation slight to moderate Alternation of nannofossil clay and calcareous silty clay	Core 977A-52X-6, 39 cm, to 57X-CC, 46 cm	490.8–532.9
			Minor: Nannofossil-foraminifer ooze	Other: Slumping throughout Cross lamination		
II		Miocene to early Pliocene	Major: Partly cemented sand to gravel	General: Very poor recovery	Core 977A-57X-CC, 46 cm, to 63X-CC	532.9–598.5

cross lamination, and increased bioturbation. Abundant slumps and associated intraclastic breccia intervals serve as an additional criteria that distinguish Subunit IB from the underlying Subunit IC.

Sediments of Subunit IB are more heavily bioturbated than those of Subunit IA. *Zoophycos* and *Planolites* are dominant; *Chondrites* is also present. Locally, burrows are infilled by pyrite or foraminifers. In Core 977A-50X where clay couplets are well-developed, burrowing is absent. Pervasive burrowing influences sediment color as most burrows are darker than the surrounding sediment.

Distinctive sedimentary structures in Subunit IB include parallel lamination, cross lamination and centimeter-scale (parallel) bedding. In laminated intervals, normal grading is common. In the bedded intervals, grayish olive (10Y 4/2) nannofossil clay alternates with paler, light olive gray (5Y 5/2) calcareous clay. These couplets are characterized by thin nannofossil clay alternations (2–10 mm) above thicker (1–2 cm) lighter-colored calcareous clay (Fig. 14). Contacts of the latter are sharp at the base and diffuse to wavy at the top. Normal grading has been recognized in several of the beds of calcareous clay.

Soft-sediment deformation is common in Subunit IB. Slumps and, locally, intraclastic breccia are recognized (Figs. 14, 15). In Core 977A-48X-5, 139 cm, to 48X-CC, 39 cm, thinly interbedded, dark (grayish olive, 10Y 4/2) nannofossil clay and pale (dusky yellow green, 5GY 5/2) calcareous clay are folded and faulted by slumping. At the top of the slump is an intraclastic breccia (Section 48X-5, 39–139 cm) consisting of horizontally aligned, flattened clasts of thinly bedded nannofossil clay and calcareous clay similar in composition to both overlying and subjacent sediment. Slump-folds in the sediments are recognized elsewhere (Section 50X-5, 22 cm to -6, 103 cm; see "Structural Geology" section, this chapter).

The base of Subunit IB is located at 490.8 mbsf (Section 977A-52X-6, 39 cm) at the sharp contact between underlying nannofossil ooze and overlying nannofossil clay. The contact corresponds to a hiatus (Section 977A-52X-6, 19–23 cm) spanning at least lower Pliocene Zone NN13 (see "Biostratigraphy," this chapter).

Subunit IC

Hole 977A, 490.6–532.9 mbsf, Sections 977A-52X-6, 39 cm, to 57X-CC, 46 cm.

The nannofossil clay of Subunit IC contains only few sedimentary structures, including rare laminations and slight to intense bioturbation. Burrow types include *Zoophycos*, *Chondrites*, and *Planolites*. Locally, burrowing has imparted faint to indistinct layering/lamination in the sediment. Alternations of decimeter-scale darker (olive gray, 5Y 4/1) calcareous clay to silty clay and meter-scale lighter nannofossil clay (light olive gray, 5Y 6/1; medium olive gray, 5Y 5/1) are present throughout Subunit IC; contacts between these lithologies have been obscured by bioturbation.

The base of Subunit IC (Section 977A-57X-CC, 46 cm) is conformable and is placed at the top of a quartzo-feldspathic, granule-bearing sand with micrite (Section 977A-57X-CC, 46 cm).

Unit II

Hole 977A, 532.9–598.5 mbsf, Sections 977A-57X-CC, 46 cm, to 63X-CC.

Unit II comprises partly cemented sand and gravel (conglomerate?) of early Pliocene to Miocene age (see "Biostratigraphy" section, this chapter). Only 1 cm of granule-rich, quartzo-feldspathics and (Section 57X-CC, 46–47 cm) and 40 cm of gravel (Sections 59X-1, 0 cm, to 63X-1, 3 cm) were recovered from a drilled interval of 57.8 m (0.75% recovery). This suggests that sand and gravel comprise the upper part of the unit. Minimal recovery during drilling does not permit detailed description of the unit, including thickness of lithologies.

The gravel comprises volcanic and sedimentary clasts. The volcanic rocks are mainly rhyodacite (Fig. 16; phenocrystic: quartz, biotite

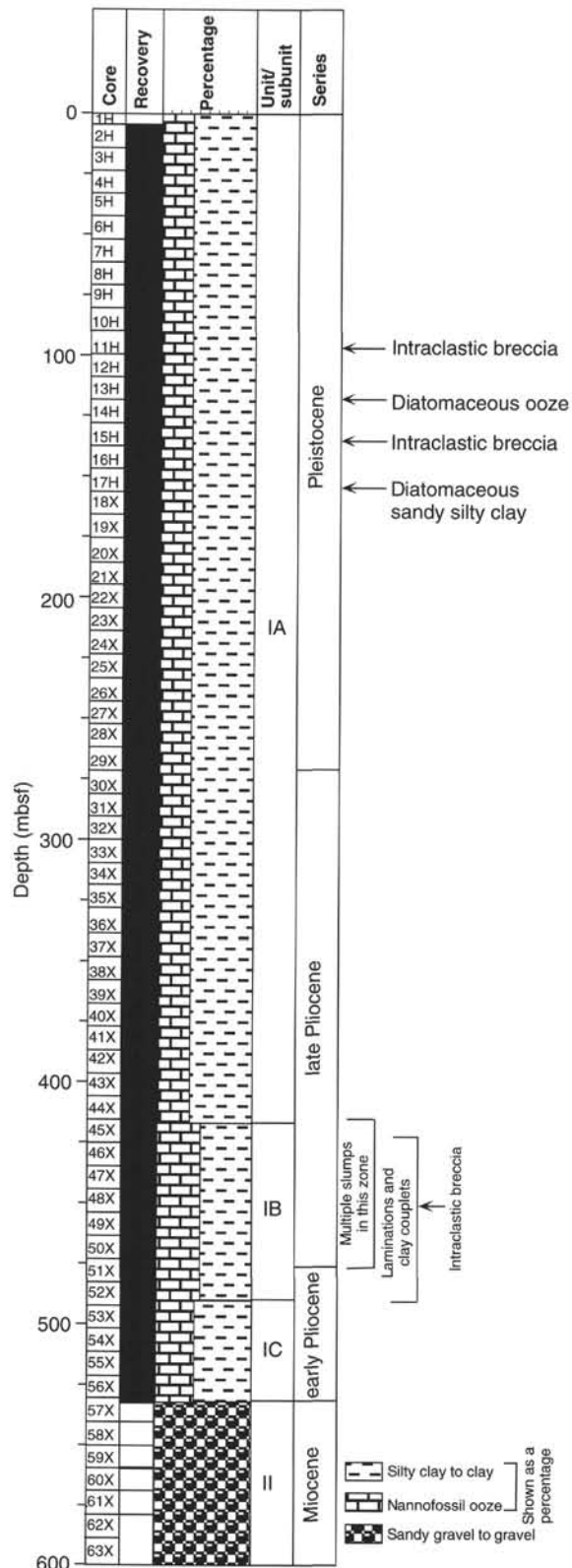


Figure 5. Generalized lithostratigraphic column and core recovery for Site 977.

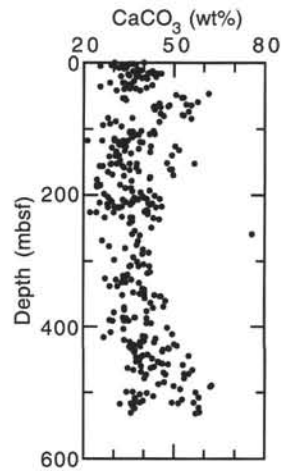


Figure 6. CaCO₃ content (wt%) plotted against depth (mbsf).

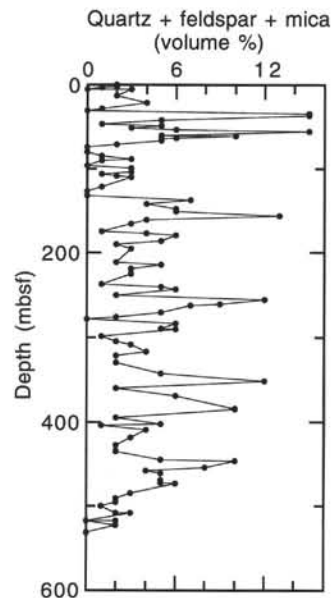


Figure 7. Quartz + feldspar + mica content (volume %) of the dominant lithologies plotted against depth (mbsf). Data are from smear slides for the dominant lithologies.

and plagioclase), with lesser (calc-alkaline to shoshonitic?) basalt/andesite (Fig. 17; phenocrystic: plagioclase in both; groundmass: quartz in andesite). Biotite in rhyodacite is locally altered to chlorite. Sedimentary rocks are dolomitic mudstone and quartz sandstone cemented by quartz and chlorite.

Clasts in the gravel vary from rounded to angular and are mostly pebble-sized (average clast size: 35 × 26 × 8 mm). Sub-rounded and rounded types are predominant (proportions: rounded = 30%, sub-rounded = 36%, subangular = 21%, and angular = 13%). A few clasts recovered were larger than the core diameter and thus have shapes generated by drilling (Fig. 16). The clasts are partly coated by a calcareous cement. Scalped indentations in the cement coating indicate former contacts with adjacent clasts. These outlines may have been produced when the slightly cemented gravel was disaggregated during drilling. Locally the gravel has remained cemented, as shown by the adhesion of some of the clasts (Fig. 16).

Table 3. Organic-rich layers (ORLs) from Site 977.

Core, section, interval (cm)	Top (mbsf)	Bottom (mbsf)	TOC (%)	Type	Key bed number
161-977D-					
1H-2, 43-72	1.930	2.220	0.87	III	L1
2H-2, 30, to 2H-3, 85	5.730	7.780	1.02 to 0.79	II	L2
2H-4, 62, to 2H-6, 75	9.050	12.180	1.07 to 0.87	II	L3
3H-4, 37-53.5	18.370	18.535	0.93	III	L4
3H-5, 25.5-45	19.755	19.950	1.13	II	L5
3H-5, 121, to 3H-6, 8	20.710	21.080	0.88	III	L6
4H-1, 33-63.5	23.330	23.635	1.13	II	L7
4H-1, 89-136	23.890	24.360	0.79	III	L8
4H-5, 146.5, to 4H-6, 13.5	30.465	30.635	0.98, 1.13	II	L9
5H-1, 34-65.5	32.840	33.155	1.00, 1.26	II	L10
5H-5, 42.5-55	38.925	39.050	1.07	II	L11
5H-5, 84-110	39.340	39.600	0.91	III	L12
7H-1, 62-107	52.120	52.570	0.84, 0.87	III	L13
7H-1, 120.5, to 7H-2, 39	52.705	53.390	0.86	III	L14
8H-5, 12-24	67.120	67.240	0.80	III	L15
9H-5, 73-95	77.230	77.450	1.71	II	L16
10H-1, 134.5, to 10H-2, 25	81.345	81.750	1.18	II	L17
10H-4, 11-39	84.610	84.890	1.01	II	L18
10H-7, 71, to 10H-CC, 5	89.710	89.810	1.39	V	L19
11H-2, 125-138	92.250	92.380		II	L20
11H-4, 47-56	94.470	94.560		V	L21
11H-4, 79-103	94.790	95.030	2.08	I	L22
12H-3, 90, to 12H-4, 67	102.900	104.170	0.58 to 0.87	III	L23
13H-1, 49.5-52.5	108.995	109.025	1.13	II	L24
13H-1, 72, to 13H-3, 134.5	109.220	112.845	0.82, 0.77	III	L25
14H-1, 6-9	118.060	118.090	1.50	II	L26
14H-1, 31-86	118.310	118.860	0.88	III	L27
14H-4, 112-134.5	123.620	123.845	1.47	II	L28
16H-3, 51, to 16H-4, 5	140.510	141.550	1.47	II	L29
17H-5, 130.5, to 17H-6, 38	153.805	154.380	0.74 to 1.42	II	L30
18X-1, 24-34	156.240	156.340	0.88	III	L31
18X-3, 10-32	159.100	159.320	1.20	II	L32
18X-6, 18-35	163.680	163.850	1.56	II	L33
19X-4, 74-100	170.840	171.100	1.25	II	L34
19X-5, 140, to 19X-6, 150	173.000	174.600	0.82	III	L35
21X-7, 21-32	194.110	194.220	1.34	II	L36
22X-6, 40-70	202.800	203.100	0.88	III	L37
23X-1, 56-73	204.560	204.730	1.50	II	L38
24X-1, 149, to 24X-2, 13.5	215.090	215.235	0.99	III	L39
25X-3, 71-100	226.940	227.230	0.96	III	L40

Notes: TOC as determined from the difference between total carbon and carbonate carbon (see "Organic Geochemistry" section, this chapter). Type: I = >2.0% TOC; II = 1.0%-2.0% TOC; III = 0.8%-1.0% TOC; IV = not used at Site 977; V = incomplete TOC at time of prep, identified by color only. TOC analyses were done at specific depths within each ORL interval and may not be representative of the TOC in the entire ORL. For exact location of TOC analysis, see Table 10. This table is also on the CD-ROM, back pocket, this volume.

Discussion

The Pliocene-Pleistocene hemipelagic sediment of Unit I comprises a 530-m-thick sequence of mainly nannofossil-rich to nannofossil and calcareous silty clay and clay. The thickness of Unit I is typical of Pliocene-Pleistocene margin-to-basin sequences elsewhere in the central and western Mediterranean. In these sequences sediment accumulation rate has been shown to be higher in more distal regions beyond the base of slope than in more proximal slope settings. Turbidity current bypass of the slope, in part associated with mass flow, has been proposed to account for this relationship (Stanley, 1983).

The minor sand- and silt-rich layers in Unit I document periodic input of coarser sediments. Calcareous sand fractions in different lithologies could represent deposits formed in situ from winnowing by bottom currents of the fine-grained carbonate and clay fraction; Comas and Maldonado (1988) have described foraminifer sands from the Iberian Abyssal Plain as foraminifer sandy contourites. These appear in Unit I as discrete beds or lenses that are generally structureless, with minimal grading, and sharp basal and upper contacts.

Siliciclastic lithologies consisting of quartz-, feldspar-, mica-rich types with subordinate rock fragments, foraminifers, and bioclasts that have sharp bases, scour-and-fill and load structures, and graded bedding. Top-cut-out sequences of the turbidites may represent sequences of mud turbidites (Fig. 12). The top-cut-out sequences com-

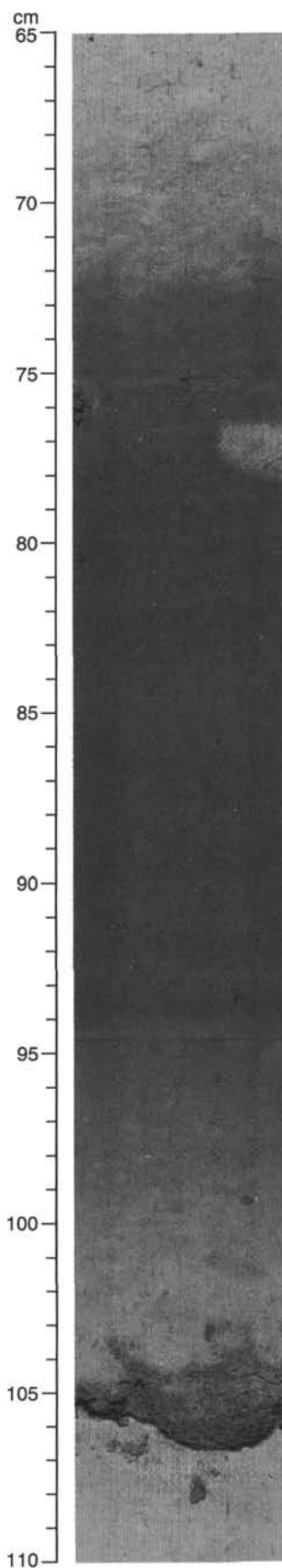


Figure 8. Organic-rich layer L16, homogeneous type, Section 977A-9H-5, 65-110 cm (see Table 3).

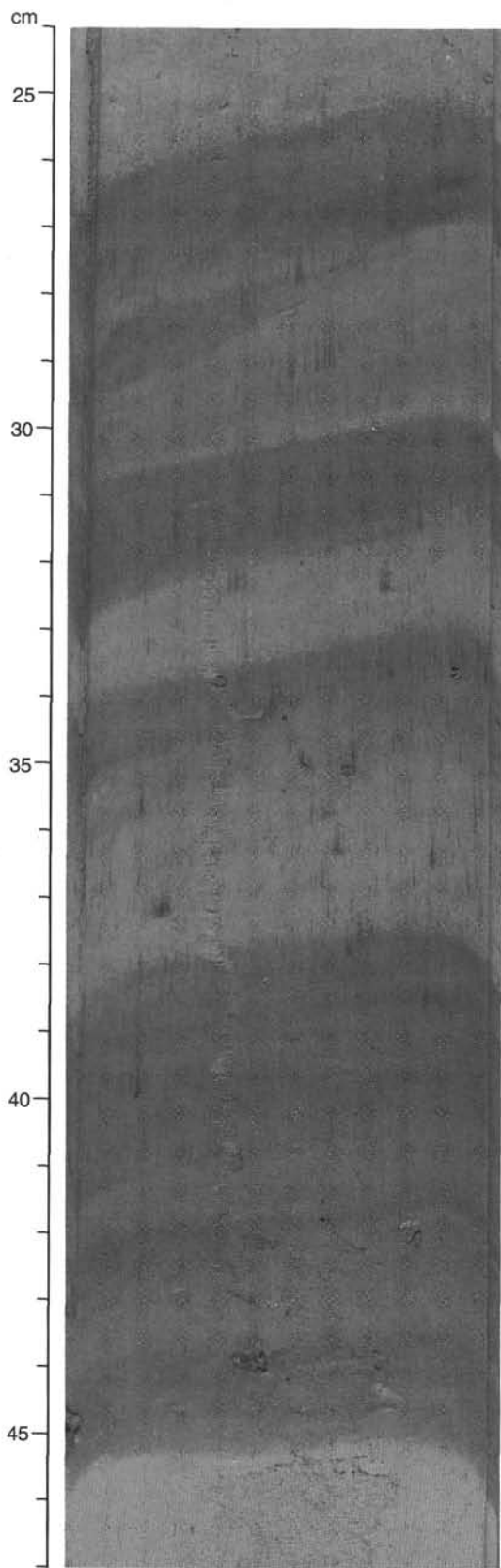


Figure 9. Organic-rich layer L5, color-banded type, Section 977A-3H-5, 24–47 cm (see Table 3).

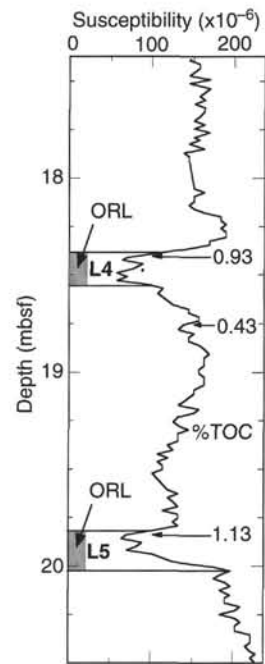


Figure 10. Plot of susceptibility against location (mbsf) in Core 977A-3H. Key beds L4 and L5 are marked. TOC for key beds L4 and L5 and intervening background sediment are marked.

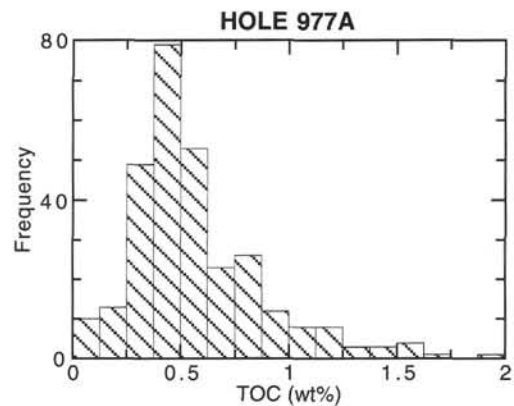


Figure 11. Frequency plot of TOC (wt%) for all analyzed sediment at Site 977.

prise only the basal silt, the convolute to irregular, and the regular-parallel to indistinct-silt laminae intervals of the mud turbidite facies model of Stow and Piper (1984; facies 4–6). Other sequences containing the graded turbidite mud and ungraded turbidite mud intervals (facies 1–3 of Stow and Piper, 1984). Some of the layers, however, may be base-cut-out sequences (Fig. 18). Gradations between these types are likely.

Much of the sediment at Site 977 appears to be hemipelagites (Stow and Piper, 1984). The average sedimentation rate of 15 cm/k.y. for the Pliocene–Pleistocene sequence at Site 977 is fairly typical of the rates observed in modern hemipelagic settings (Scholle and Ekdale, 1983). Variations in carbonate content are present in hemipelagites and turbidites of Site 977. First, the interval from 40 to 80 mbsf, shows elevated carbonate content; second, a gradual increase in carbonate content with depth begins about 410–420 mbsf, and third, sediments of Subunit IC show grouping into low and high car-

Table 4. Table of carbonate minerals (identified by X-ray diffraction) associated with peaks in magnetic susceptibility.

Core, section, interval (cm)	Sedimentary association	Smear-slide notes	Minerals
161-977A-			
17H-5, 129–131	Brown, oxidized layer at top of ORL	Lens-shaped micrite	Kutnohorite, ankerite?, dolomite?
24X-1, 144–146	Top of ORL	Lens-shaped micrite	Kutnohorite, dolomite, siderite
27X-1, 55–57	Silty parting of calcareous silty clay	High-relief, rounded grains	Siderite, dolomite, mica
28X-3, 24–26	Interval in calcareous silty clay	No smear	Siderite, dolomite
38X-6, 26–28	Highly bioturbated interval in calcareous silty clay	No smear	Siderite, dolomite
39X-4, 70–92	Highly bioturbated greenish interval	No smear	Siderite, dolomite
51X-1, 119–120	Dark, pyritized layer in calcareous clay	High-relief, rounded grains	Ankerite, dolomite?, trace siderite
52X-5, 94–95	Burrowed nannofossil clay	No smear	Dolomite

bonate content intervals (Fig. 6; see “Lithostratigraphy,” Site 978 chapter, this volume).

Influx of terrigenous components at Site 977, as reflected by the quartz + feldspar + mica fraction, has varied throughout the Pliocene–Pleistocene (Fig. 7). Peaks in this fraction could relate to sea-level lowstands (see also “Site 976” chapter, “Lithostratigraphy” section, this volume), increased weathering and runoff, tectonic influences, or the frequency of turbidity currents. As described earlier, the quartz-, feldspar-, mica-rich lithologies are most abundant in the Pleistocene (although they extend into at least the late Pliocene) and are interpreted to be the basal/graded intervals of (thicker) muddy turbidites. Possible sources of the terrigenous components include the African and Spanish continental margins. Lack of a volcanogenic component in Unit I sediments, despite proximity to the Al-Mansour seamount, suggests that the continental margins are the most important contributors of the terrigenous component at Site 977.

The restriction of ORLs to the Pleistocene section at Site 977 is similar to the frequency distribution seen at Site 974 (29 of 36 ORLs are Pleistocene in age) and Site 975 (33 of 37 ORLs are Pleistocene in age). Figure 19 depicts the abundance of ORLs to 300 mbsf. Also depicted are sedimentation rates over the same interval. There appears to be little correlation between ORLs and sedimentation rate. Some of the ORLs at Site 977 have silty partings/laminae and show microbioturbation features at the top followed by coarser-scale bioturbation above this zone (Fig. 20) and therefore resemble base-cut-out turbidites. Slumps/mass flows and turbidites in northwest African continental rise and Madeira abyssal plain sediments have been shown to have enhanced organic matter preservation in sediments with an otherwise limited potential for preservation of organic carbon (Rullkötter et al., 1982).

Slumps and associated intraclastic breccias in Unit I likely relate to sediment slides. Such slides initiate slumping that can result in soft-sediment deformation ranging from little-deformed to intensely folded, faulted, and brecciated sediment (Pickering et al., 1989). This full range of features can be seen in single deposits at Site 977 (Figs. 14, 15). The occurrence of virtually identical lithologies within, above, and subjacent to the slumps found at Site 977 suggests a proximal source rather than transport from great distance.

In summary, the Pliocene–Pleistocene sediments at Site 977 have been deposited through hemipelagic, turbidity and contour current, and mass flow processes. This facies association is typical of basin (or basin plain) areas adjacent to slopes with some tectonic activity. The concentration of siliciclastic lithologies in the Pleistocene to late Pliocene sequence suggests a possible climatic influence on the origin of the mud turbidites.

Unit II sediments comprise slightly-cemented sandy gravel to gravel. Seismic profiles in the vicinity of Site 977 illustrate that the base of the recovered sequence at Site 977 is located in what is interpreted to be a paleo-channel (see “Background and Objectives” section, this chapter). The occurrence of sandy gravel and gravel and the channel-like form of these sediments (see seismic line) suggest that Unit II sediments represent channel fill.

Composition of the volcanic pebbles in the gravel may eventually give some indication as to potential source. Preliminary study shows

that rhyodacite pebbles in the gravel are macroscopically and microscopically similar to rhyodacites sampled by diving at the Yusuf Ridge and Al-Mansour seamount (Comas et al., in press). Miocene-age volcanic rocks from the Cabo de Gata (Bellon et al., 1983) and from the Alboran Ridge (Hernandez-Pacheco and Ibarrola, 1970) are compositionally similar to the basalt/andesite pebbles recovered. Thus, two probable source areas for the volcanic pebbles could be involved: one proximal (Yusuf Ridge, Al-Mansour Seamount), and one more distal (Alboran Ridge, Cabo de Gata). In the latter case, the “Almería channel” on the south Spanish Margin may have served as a pathway for sediment transport to the Alboran Basin during its inception in the Miocene (Alonso and Maldonado, 1992).

BIOSTRATIGRAPHY

Calcareous Nannofossils: Abundance and Preservation

Cores recovered at Site 977 contain common to abundant calcareous nannofossils, except for Sample 977A-60X-CC, which contains few nannofossils. Preservation is good, or moderate to good, in all cores except in the lower Pliocene interval from Samples 977A-52X-CC to 977A-60X-CC, where preservation is moderate or poor to moderate. A poor to moderate nannofossil assemblage was also obtained by scraping two lithified pebbles from Section 977A-60X-1.

Biostratigraphy

Hole 977A (Fig. 21)

The stratigraphic interval in this hole ranges from Serravallian (Zone NN7) to uppermost Pleistocene–Holocene (Subzone NN21B). All zones and subzones from NN14 to NN21B are present.

In nannofossil biostratigraphy, the Pliocene/Pleistocene boundary is approximated by the first appearance of *Gephyrocapsa oceanica*, which also marks the NN19B/NN19A Subzonal boundary. This boundary occurs between Samples 977A-29X-1, 65–67 cm (262.46 mbsf) and 29X-2, 65–67 cm (263.96 mbsf), but we place it at 270.87 mbsf (Fig. 21), based on foraminiferal data (see “Planktonic Foraminifers” section, this chapter).

The lower/upper Pliocene boundary is between Samples 977A-51X-2, 21–22 cm (475.01 mbsf) and 51X-3, 18–19 cm (476.48 mbsf). A hiatus spanning at least part of the lower Pliocene Zone NN13 occurs between Samples 977A-52X-6, 19 cm (Zone NN14; 490.59 mbsf) and 52X-6, 23 cm (Zone NN12; 490.63 mbsf).

The intervals from Samples 977A-57X-1, 25–26 cm (531.13 mbsf) to 57X-CC, 45 cm (532.90 mbsf) is assigned to the lowermost Pliocene (NN12), based on the absence of *Pontosphaera japonica*. Very rare occurrences of Messinian nannofossils are recorded within this interval: *Cryptococcolithus mediaperforatus*, *Hayella challengeri*, *Helicosphaera orientalis*, *Helicosphaera stalis stalis*, *Hughesius gizoensis*, *Reticulofenestra rotaria*, *Syracosphaera fragilis*, and *Tetralithoides symeonidesii*. Because the occurrence of these latter species is inconsistent, their presence may be explained by Messinian sediment reworking.

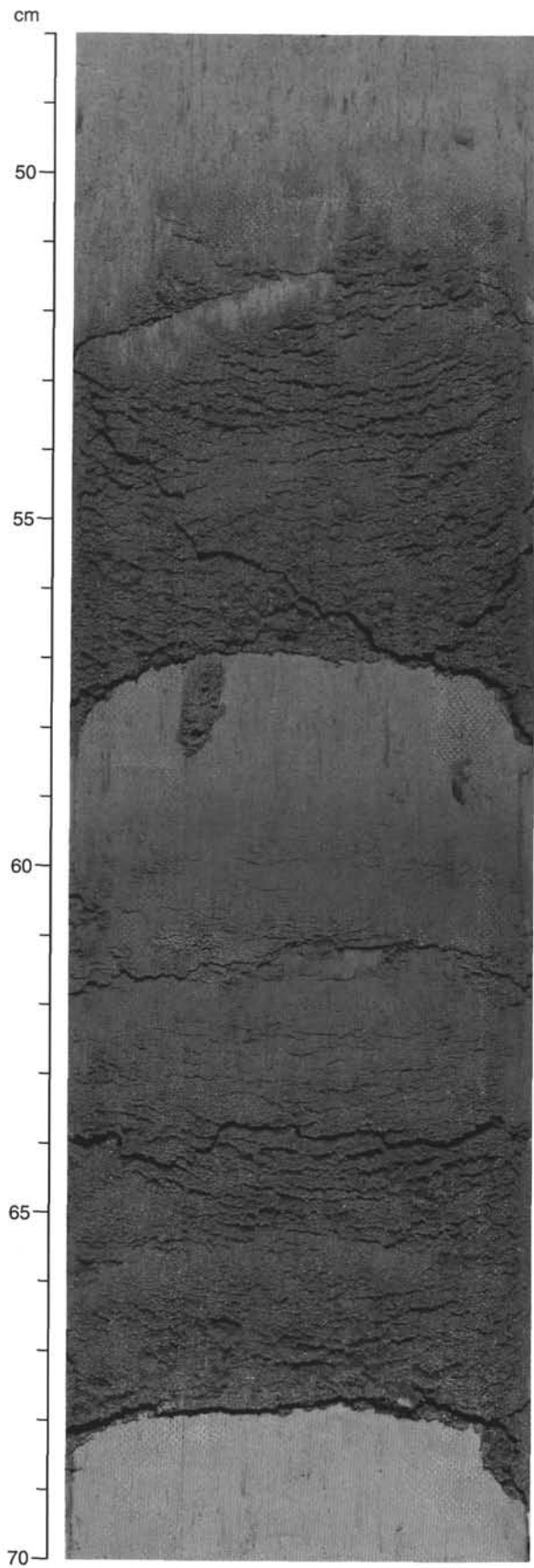


Figure 12. Example of Group 2 lithologies in Unit 1, Section 977A-15H-2, 48–70 cm. Adjacent sandy silt intervals represent two distinct layers. Note sharp base in both. Lower layer has a gradational top. The upper layer has a sharper, though somewhat irregular top.

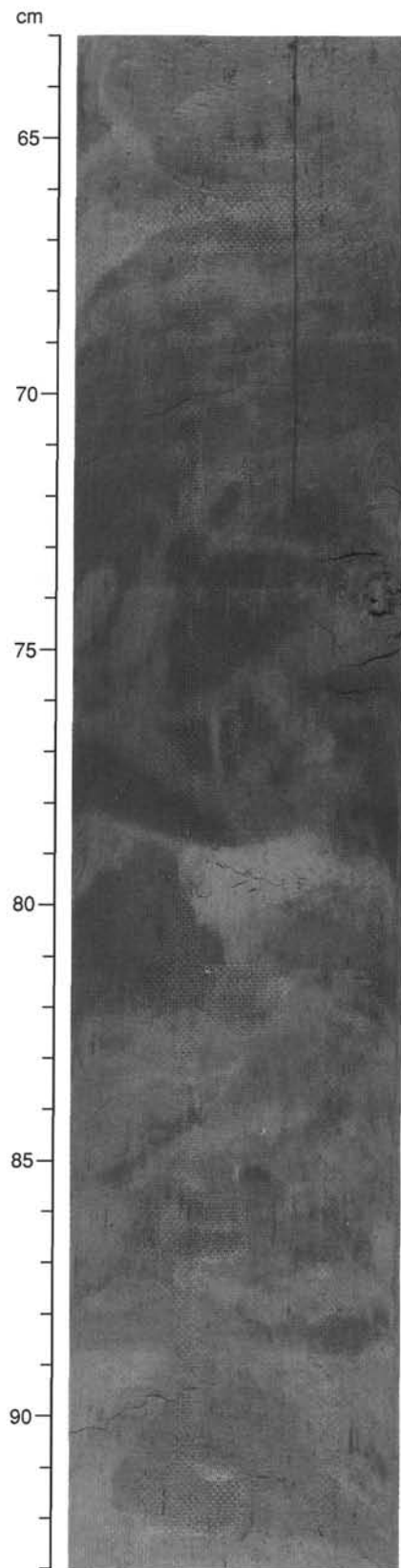


Figure 13. Intraclastic breccia in Section 977A-11H-6, 63–93 cm (see Table 2). Distinct light gray, medium gray, and dark gray clasts can be distinguished, particularly at 78–83 cm. Some clasts are composed of bioturbated lithologies.

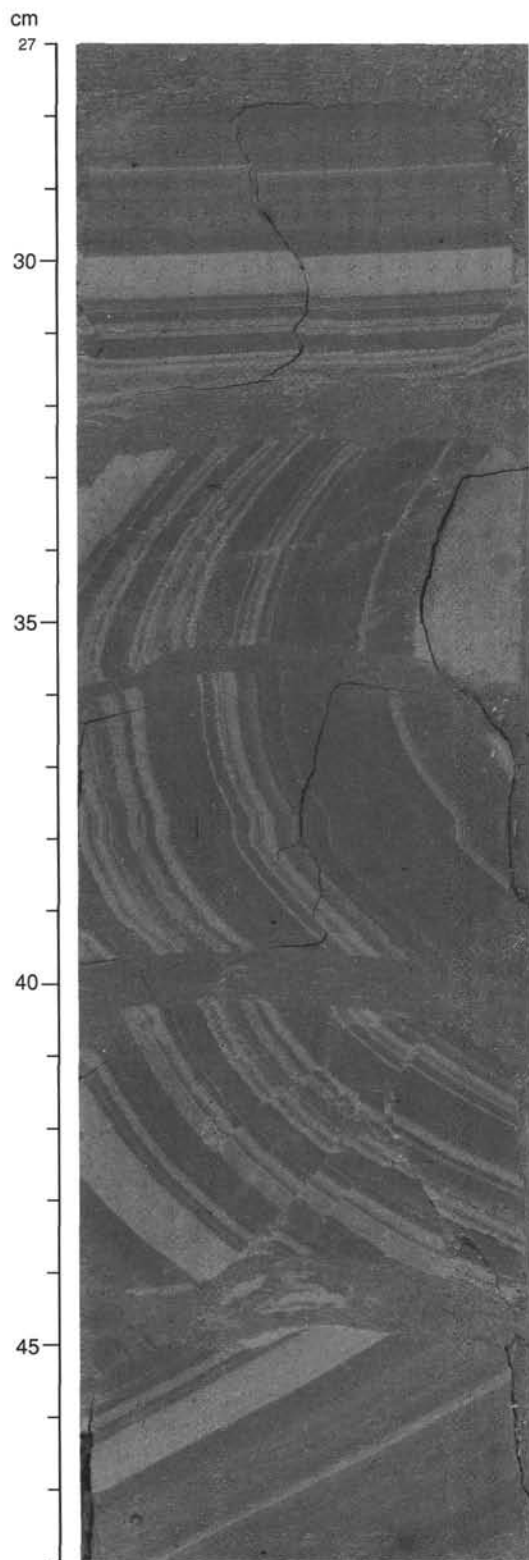


Figure 14. Slump fold in Pliocene clay in Section 977A-48X-6, 27–48 cm. Thinly interbedded, dark (grayish olive, 10Y 4/2) nannofossil clay and pale (dusky yellow green, 5GY 5/2) calcareous clay are folded and faulted by slumping. The structure has been separated into sections (“biscuits”) and rotated by drilling-induced deformation. Very short wavelength crenulations are present in the white laminations, probably caused by later compaction.

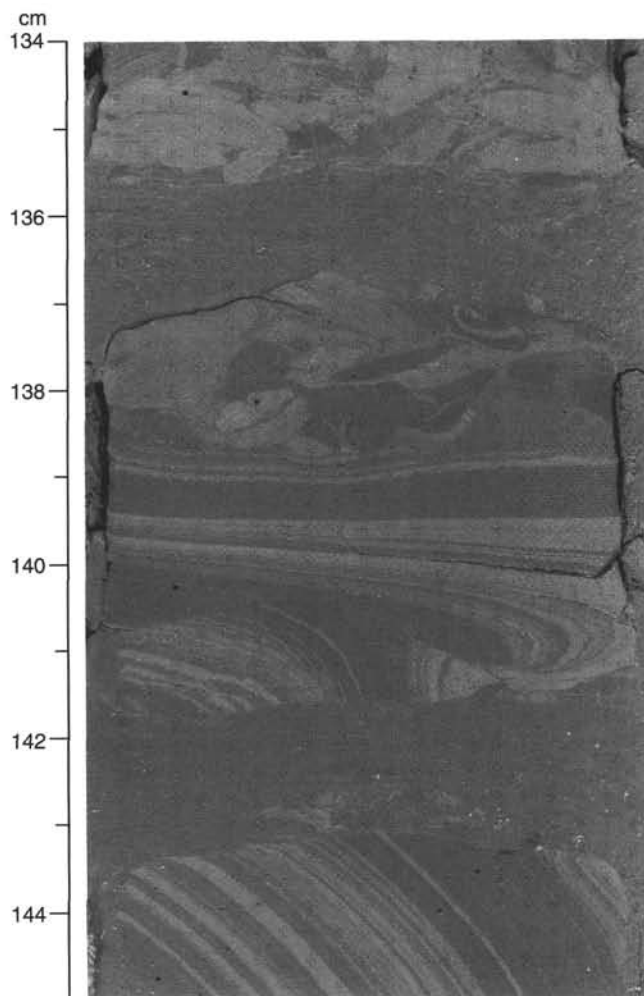


Figure 15. Transition from intraclastic breccia to slump in Section 977A-48X-5, 134–145 cm. From top to bottom: intraclastic breccia overlying sub-horizontal to folded, thinly interbedded nannofossil clay and pale calcareous clay.

Scrapings from Sample 977A-60X-1, Piece 4 (560.10 mbsf) yielded an assemblage containing *Cyclicargolithus floridanus*, *H. orientalis*, and *Calcidiscus macintyreii*; this sample is assigned to Zone NN7 (Serravallian).

Planktonic Foraminifers: Abundance and Preservation

Planktonic foraminifers are abundant and well preserved through the Pleistocene in Hole 977A. In the Pliocene interval, foraminifers are abundant and preservation is generally good, although in some samples signs of enhanced dissolution and fragmentation exist. In Samples 977A-48X-5, 4–6 cm (450.56 mbsf) to 57X-CC (532.90 mbsf) most foraminifers show overgrowth and recrystallization. In Core 57X, foraminifers are very poorly preserved, fragmented, deformed, or flattened. This site is mostly pelagic with minimal amounts of detrital material and displaced fauna.

Biostratigraphy

Biozones, the distribution of marker species, and sampling intervals are shown in Figure 22.

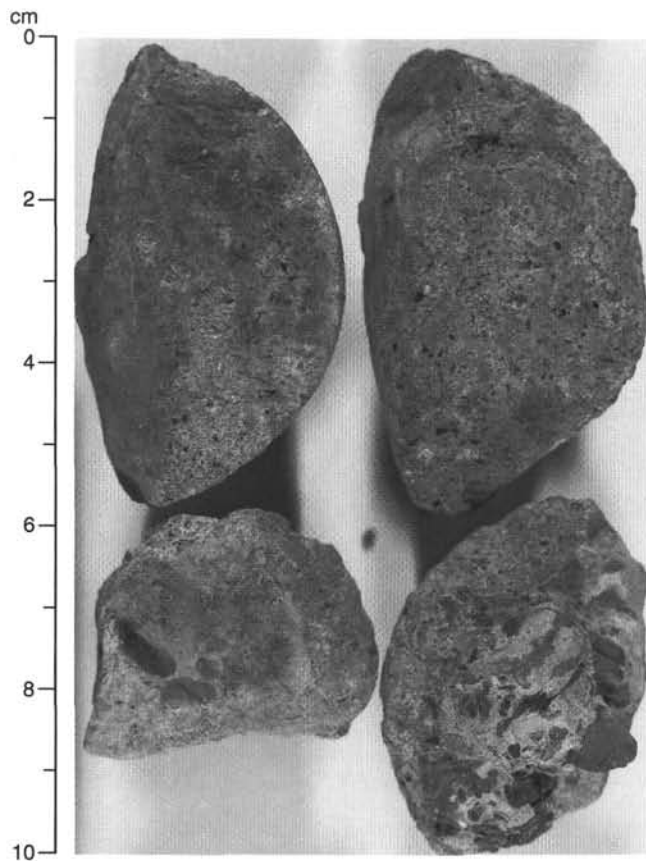


Figure 16. Angular to subrounded rhyodacite pebbles (average grain size of $50 \times 34 \times 17$ mm), Section 977A-60X-1, Pieces 1A, B (the text refers to the shape of pebble in the lower left part of the photograph). The fresh pale olive gray to light greenish gray, aphanitic to fine-grained groundmass contains equigranular biotite (≤ 4 mm), plagioclase, and quartz (≤ 3 mm). Limestone and quartzite clasts (up to $12 \times 7 \times 4$ mm) are cemented to the top/base of pebble in lower right.

Site 977A (Fig. 22)

A lowermost Pliocene (MPL1)–Pleistocene sedimentary sequence (533 m thick) was recovered from the seafloor through 532.88 mbsf (Sample 977A-57X-CC, 45–46 cm). Below this a thin layer of conglomerate was recovered. All Pliocene–Pleistocene foraminiferal biozones and marker species are represented.

The Pleistocene is well represented by both *Globorotalia truncatulinoides excelsa* and *Globigerina cariacensis* Zones. The marker species are common only in some samples. Fifteen samples in Cores 977A-29X and 30X were studied to constrain the Pliocene/Pleistocene boundary based on the first increase of *Neogloboquadrina pachyderma* (sinistral coiling). This event occurs in Sample 977A-29X-4, 65–67 cm (266.95 mbsf). The other taxa commonly recorded in the Pleistocene are *Globorotalia inflata*, *Neogloboquadrina dutertrei*, and *Globigerinoides ruber*. The *Globorotalia crassaformis* group occurs irregularly.

The Pliocene is represented by all biozones (MPL6 through MPL1). *Globorotalia bononiensis*, which characterizes Zone MPL5a, is consistently present throughout the zone. Between Zone MPL3 and MPL2 there is a hiatus that is only suspected in the foraminiferal data (Zone MPL3 is very short). Sedimentation rate and nannofossil data (part of NN13 is missing) confirm this hypothesis. *G. punctulata* in Sample 52X-6, 11–13 cm (490.51 mbsf) is not likely its first occurrence. *Globorotalia margaritae* is never common

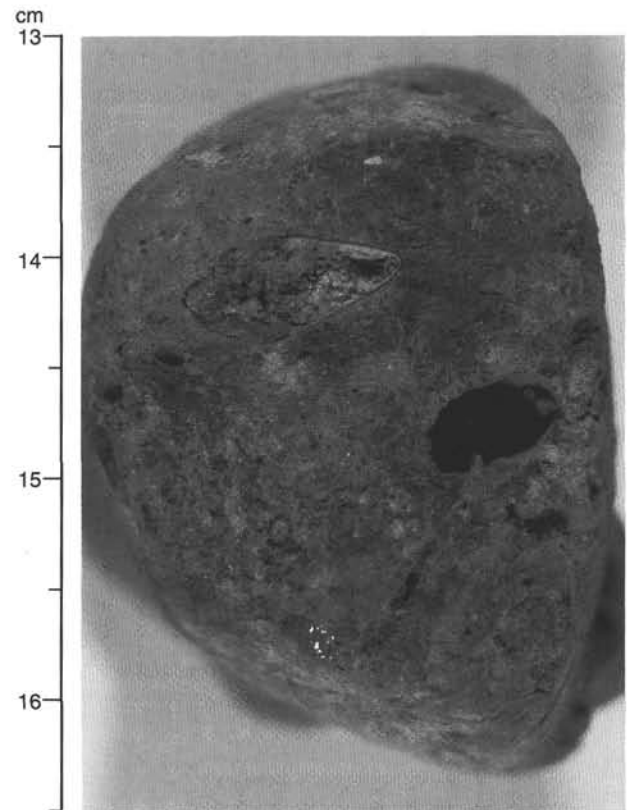


Figure 17. Basalt/andesite (calc-alkaline to shoshonitic) pebble, Section 977A-60X-1, Piece 3. Dark gray, subrounded pebble is porphyritic with pyroxene (< 3 mm), plagioclase (< 1 mm), olivine (< 1 mm), and vitric single- and compound-vesicles ($< 12 \times 5 \times 3$ mm) contained in a fine-grained, greenish gray holocrystalline (plagioclase) groundmass. The pebble is partly coated with fine-grained calcareous cement.

and, at times, is missing. As a result, the recognition of Zone MPL1 was difficult, in spite of the numerous examined samples. The abundance of *Orbulina*, *Globigerinoides*, and *Globigerina* genera, which characterize the lowermost Pliocene in other parts of the Mediterranean basin, suggests Cores 977A-56X and 57X belong to the lowermost Pliocene (MPL1), despite the scarcity of the marker species, the poor preservation, and the poorly diversified assemblage. Rare specimens of typical *G. margaritae* associated with more inflated forms (close to *G. cibaoensis*) occur within this interval. Below Sample 977A-57X-CC no more samples were recovered for planktonic foraminiferal analysis.

Benthic Foraminifers

Benthic foraminifers at Site 977 (present-day water depth 1984 m) are larger in size, more abundant and more diverse than at Sites 974 or 975, and are comparable in size, diversity, and distribution to those at Site 976. They are diagnostic of upper mesobathyal to lower mesobathyal (1000–4000 m) depths as defined by Wright (1978). They generally comprise $< 1\%$ – 2% of the total foraminiferal assemblage, except where there is occasional evidence for downslope contamination by shelf taxa that are often abraded and mixed with deeper water assemblages.

Biozonal Correlation

Correlation of the calcareous nannofossil and planktonic foraminiferal zonations for Hole 977A is shown in Figure 23. The placement

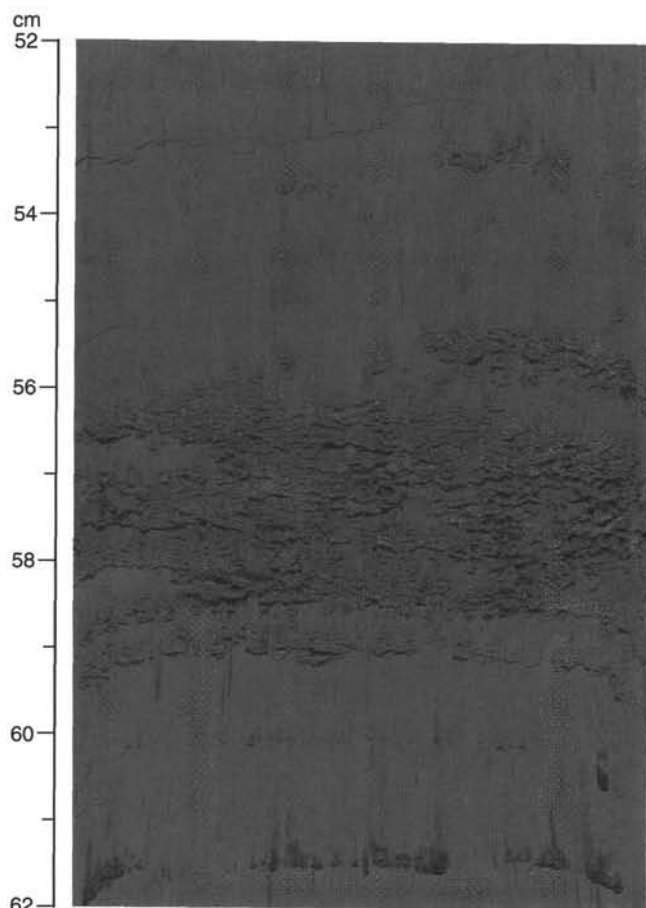


Figure 18. Base-cut-out turbidite, Section 977A-11H-3, 52–62 cm. Note multiple, thin silt partings ranging from discontinuous to continuous. Dark interval over silt may be muddy top to the turbidite. Texture somewhat obscured during core splitting.

of the Pliocene/Pleistocene boundary is based on calcareous nannofossils and planktonic foraminifers. A lower Pliocene hiatus spanning an estimated 0.5 m.y. occurs between Samples 977A-52X-6, 11–13 cm (490.51 mbsf) and 52X-6, 25–27 cm (490.65 mbsf). This estimated missing interval in the lower Pliocene is based on calcareous nannofossils. The lowest part of the sequence (Core 977A-57X), according to the planktonic foraminifers, is lowermost Pliocene, but contains reworked calcareous nannofossils from the uppermost Miocene (Rotaria Zone).

Paleoenvironment

Planktonic and benthic foraminifers are indicative of an open-marine environment with planktonic foraminifers dominant over benthic foraminifers. However, the regular presence of echinoid spines and a few inner neritic benthic foraminifers suggest weak, but continuous, sediment input from shallower waters. Foraminifers and calcareous nannofossils below Core 977A-45X generally indicate a more pelagic paleoenvironment, as indicated by a decrease of benthic foraminifers, and an increase in *Discoaster* species, and phosphatic remains.

Sedimentation Rates

Figure 24 shows the sedimentation rates for Hole 977A. Age data (Table 5) are based on first and last appearance events of selected

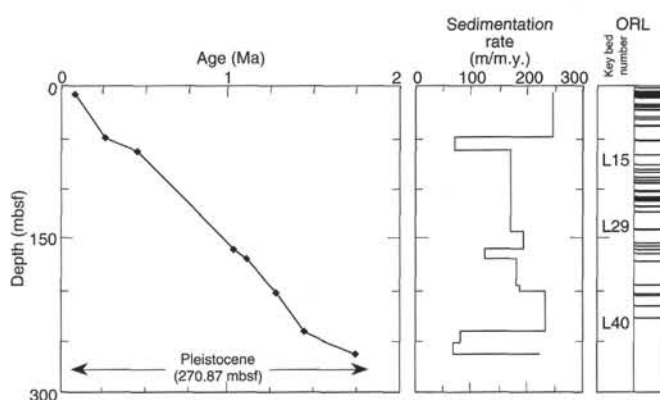


Figure 19. Sedimentation rate and occurrence of ORLs in Pleistocene section of Hole 977A. Individual ORLs are marked by horizontal lines. Key bed numbers L15, L29, and L40 (Table 3) are marked for reference.

nannofossils and planktonic foraminifers (see Table 2 in “Explanatory Notes” chapter, this volume). Average sedimentation rates in Hole 977A are 154 m/m.y. for the Pleistocene–Holocene, 96 m/m.y. for the Pliocene (to the unconformity). This interval, separated by the last occurrence of *D. tamalis* (point 17 on Table 5), shows a lower part (points 17 to 23 on Table 5) with an average sedimentation rate of 55 m/m.y. and an upper part (point 17 to 11 on Table 5) with a sedimentation rate of 148 m/m.y. Just below the unconformity, the sedimentation rate increases more than 400 m/m.y.

PALEOMAGNETISM

Fifty-six APC and XCB archive halves were measured with the cryogenic magnetometer. Blanket AF demagnetization was routinely applied at 15 mT. Some archive sections were progressively demagnetized up to 30 mT. Rock-magnetic studies were carried out for two intervals of the stratigraphic sequence: from 0 to 1.3 mbsf, to document initial diagenesis of magnetic minerals and from 150 to 540 mbsf, to determine the relationship between peaks in magnetic susceptibility and lithology. APC cores were oriented with the Tensor tool (Table 6).

Remanent Magnetization

Between 60 and 420 mbsf, NRM intensity and low-field magnetic susceptibility have weak values of the order of 10^{-4} A/m and 10^{-4} SI, respectively (Fig. 25). Above and below this interval, there is a sharp increase of about 10^{-2} A/m in the NRM intensity whereas susceptibility increases 2 to 3 times (3×10^{-4} SI).

The declinations of magnetization are relatively well grouped from core to core above 60 mbsf, are more scattered in the interval of low magnetization (60–420 mbsf), and cluster near 20° to the X-axis from 420 to 540 mbsf. Re-oriented declinations using Tensor tool data show scattered declinations implying insufficient demagnetization to thoroughly remove overprinting (Fig. 26).

Inclinations are largely positive after 15 mT AF demagnetization. Among the negative inclinations recorded, most show no change in declination with respect to the neighboring positive inclination. This suggests that these negative inclinations may be obscured by an overprint as seen in Site 976. Stepwise demagnetization of discrete samples were not successful due to the weakness of NRM intensity and instrument trouble with the spinner magnetometer.

Therefore, as at Sites 974, 975, and 976, magnetostratigraphy is not defined at Site 977. For example, there is no evidence of the Brunhes/Matuyama polarity transition that, based on biostratigraphic

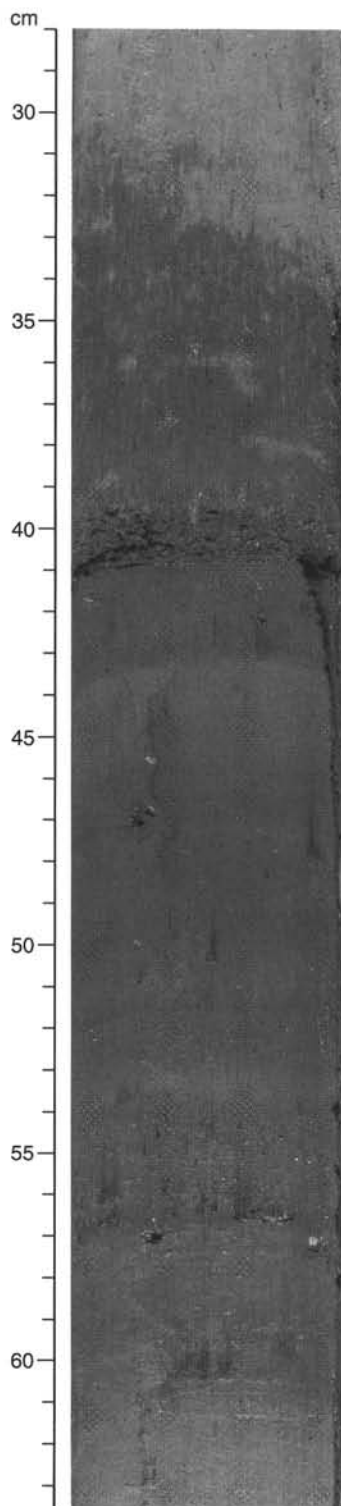


Figure 20. Organic-rich layer (key bed L7), Section 977A-4H-1, 28–63.5 cm. Note dispersed silt in interval from 56 to 57 cm and prominent silt layer from 40 to 41.5 cm. Top of the ORL is heavily bioturbated.

data, should be found at about 120 mbsf (Fig. 25). The apparent reversal at 10 mbsf has been encountered also at Sites 974 and 975.

Rock Magnetism of the Uppermost Sediment

Six discrete samples from the uppermost sediment (Section 977A-1H-1, 0 to 1.38 mbsf) were analyzed to document rock-magnetic properties just beneath the seafloor. We measured NRM direction, median destructive field (MDF) of NRM and ARM, SIRM, back-field IRM (-0.3 T), and low-field susceptibility (K). In addition, 6 samples from Section 976D-1H-1 were also analyzed. The uppermost part of the core generally exhibits less overprint throughout the sites. Characteristic directions were easily revealed by demagnetization above MDF for all samples analyzed.

The rock-magnetic data are shown in Figure 27 and Table 7. General trends observed in these two data sets can be simplified as follows:

1. K and SIRM decrease or remain constant downsection except for anomalous values from 0.1 to 0.2 mbsf, where sediment water content is very high; these data need to be calibrated with dry weight. This may suggest slight dissolution of magnetic minerals in this interval.
2. Mineral indexing parameter, $S_{-0.3T}$, does not change except for anomalously low values in the uppermost sample. Mostly high values (>0.96) suggest dominance of a magnetically soft mineral such as magnetite.
3. MDFs of NRM and ARM show a downcore increase. Two magnetic granulometric interparameters, K_{arm}/K and $K_{arm}/SIRM$, also increase, which suggests an increase in the fine-grained fraction of magnetic minerals.
4. NRM intensities, after 15 mT demagnetization in the samples examined, show different patterns in the uppermost part of Section 1H for both cores. However, both increase rather smoothly below 1 mbsf. This may suggest an increase in efficiency of detrital remanent magnetization (DRM) as the sediment becomes compacted (Otofuji and Sasajima, 1981).

Rather constant SIRM values indicate little change in the amount of ferrimagnetic material in the sediments. This is assumed because there is no significant change in magnetic mineralogy (constant $S_{-0.3T}$ value). The constant increase in the magnetically high-coercive portion, as expressed by an increase of K_{arm}/K and $K_{arm}/SIRM$, implies formation of stable single-domain magnetic minerals above an iron reduction zone. Grain growth from very fine crystals or even from amorphous materials is one possible interpretation (Karlin et al., 1987). Continuous dissolution of iron-bearing minerals may reduce mean grain size to give some increased magnetic coercivity. On the other hand, coarsening of the mean grain size of magnetic minerals is generally recognized in anoxic conditions. As iron dissolution continues or sulfide-reducing conditions are enhanced, fine minerals are readily exhausted with increasing depth (Canfield and Berner, 1987). As discussed in Site 976, rock-magnetic parameters suggest a rapid coarsening of magnetic minerals from 0 to 100 mbsf (see Fig. 42 in the "Site 976" chapter, this volume). This is also confirmed by Sample 977A-1H-3, 18–20 cm (Table 7). The magnetic mineral grain growth seems to continue to at least 1.5 mbsf and then dissolution may take over, depleting remanence-carrying minerals.

Sources of Magnetic Susceptibility from 150 to 540 mbsf

The second objective of rock-magnetic studies was to understand sources of magnetic susceptibility (K) by studying the anhysteretic remanence susceptibility K_{arm} and IRM (at 1 T, -0.3 T, and -0.1 T) of 34 discrete samples taken from 150 and 360 mbsf and from 420 to 540 mbsf (Table 8). The sharp change in susceptibility (Fig. 25) between these two intervals also corresponds to a change in sedimentation rate.

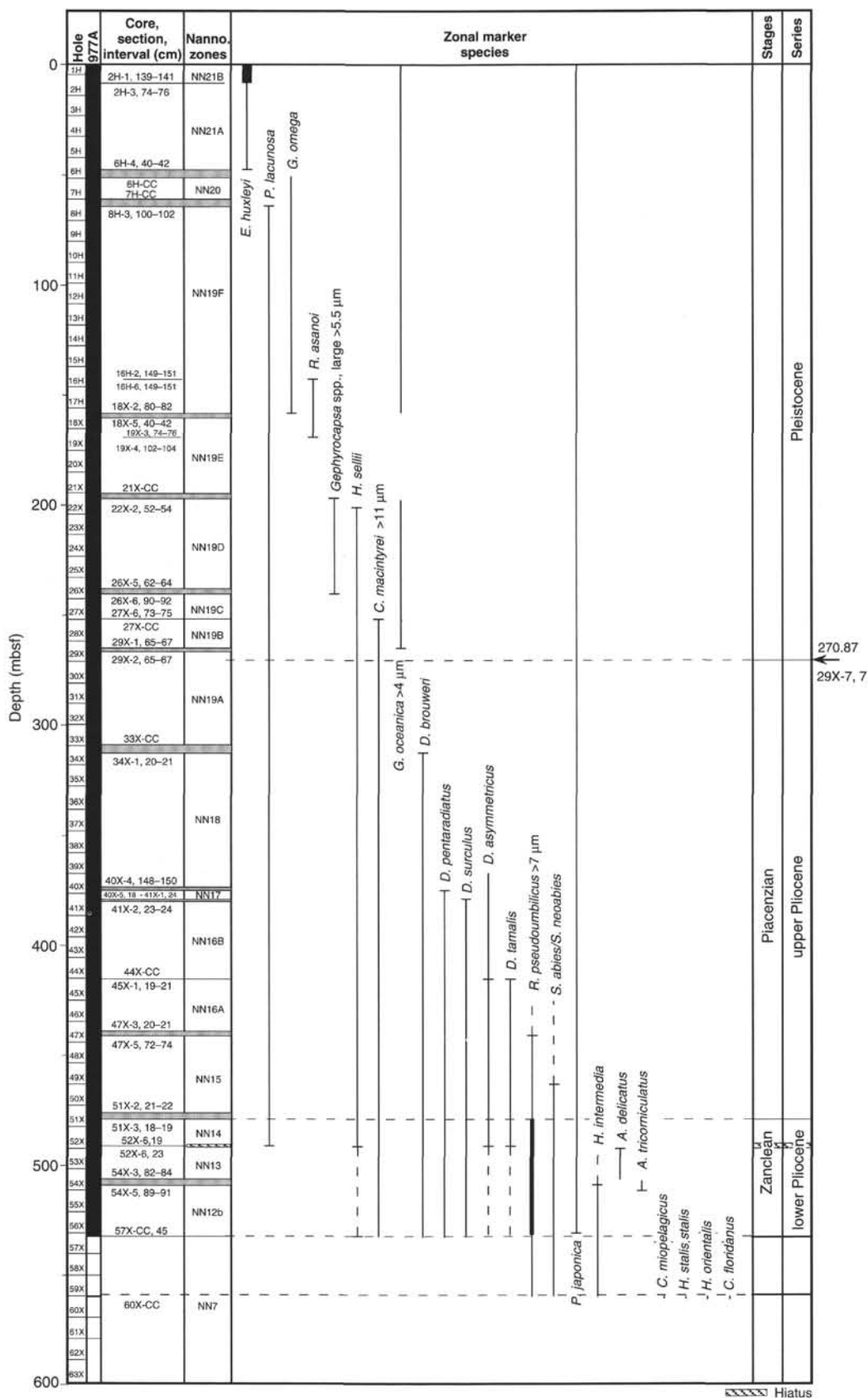


Figure 21. Calcareous nannofossil zonation of Hole 977A. Bold lines represent acme intervals. Lack of a short horizontal line at the end of a species' vertical range line indicates that the range of that species is incomplete. Dashed vertical lines below the Mediterranean bases of *H. sellii* indicates its irregular global occurrence. Dashed vertical lines above the LO indicates possible reworking. Shaded areas represent intervals not sampled.

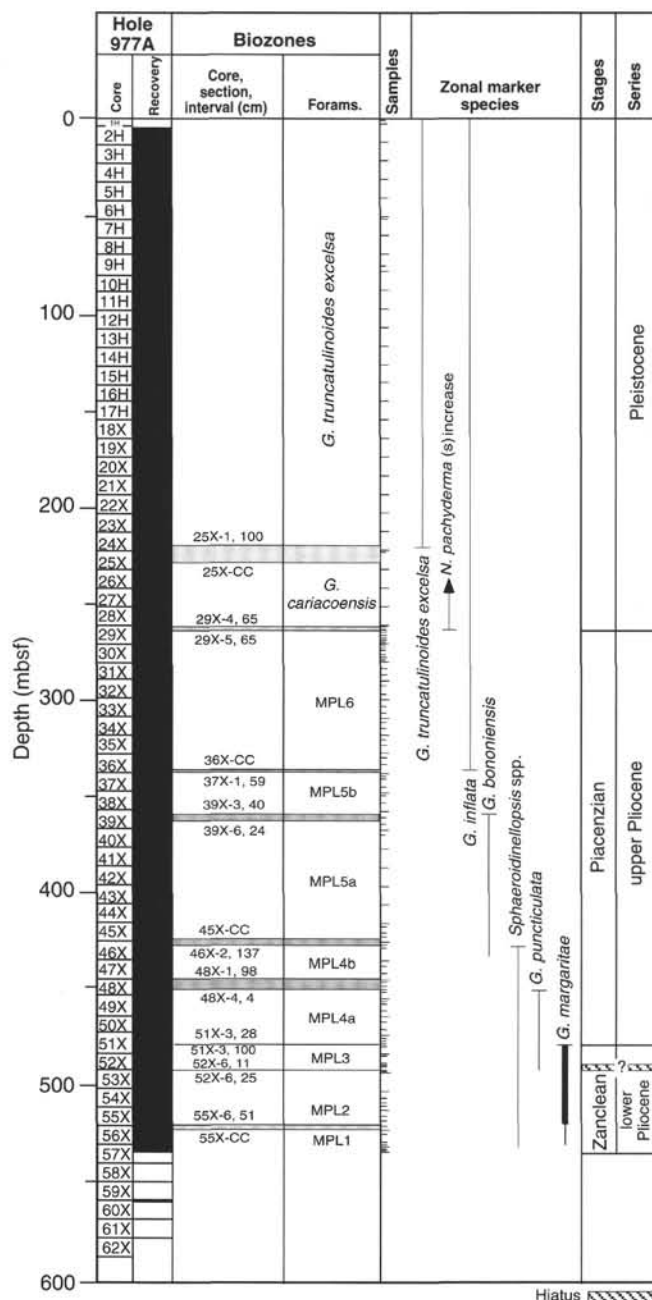


Figure 22. Planktonic foraminiferal zonation of Hole 977A. Bold lines represent acme intervals. Lack of a short horizontal line at the end of a species' vertical range line indicates that the range of that species is incomplete. Shaded areas represent intervals not sampled.

From 150 to 360 mbsf (Fig. 28A), K is low, relatively constant (10^{-4} SI), and displays a few discrete peaks that have values up to 4×10^{-4} SI that generally occur just above an organic-rich layer (see "Lithostratigraphy" section, this chapter). In contrast, K_{arm} is lower (about 25×10^{-6} SI) and apparently not dependent on K (Table 8). An exception is the very low values of K_{arm} within the organic-rich layer that gives a peak in susceptibility. K/K_{arm} show values of about 10, which is much higher than the background (Fig. 28B). An apparent relation exists between K/K_{arm} and the TOC recorded just below these peaks (Fig. 28B). $S_{-0.3T}$ values ($S_{-0.3T} = 0.94 \pm 0.03$) suggest low co-

ercivity magnetic carriers. However, since K_{arm} is imparted at 0.1 T (AF), we tried to determine the coercivity of the mineral at this magnetic field value. Therefore, we carried out measurement of IRM at 0.1 T for a few samples. A ratio of $-IRM_{0.1T}/SIRM$ was 0.40, indicating that less than half of SIRM is acquired at 0.1 T. This could partly explain the low values of K_{arm} .

In the second interval 420–540 mbsf, values of K are 2 times higher (2×10^{-4} SI), with peaks up to 10^{-3} SI. Contrary to the interval above, K_{arm} shows higher values of about 46×10^{-4} SI (Table 8; Fig. 28A) and ferrimagnetic grains have lower coercivities ($S_{-0.3T} = 0.97 \pm 0.01$), as indicated by higher $-IRM_{0.1T}/SIRM$ of 0.80.

Thus, there are two distinct magnetic assemblages in these two intervals. The dominant sources of magnetic susceptibility between 420 and 540 mbsf are low-coercivity ferrimagnetic grains such as magnetite and to a lesser extent, from paramagnetic and/or antiferromagnetic grains. In contrast, the magnetic susceptibility in the interval 150–360 mbsf is caused by paramagnetic and/or antiferromagnetic grains that give rise to low values of K_{arm} . Probably small amounts of ferrimagnetic minerals, together with stronger coercivities, may explain low NRM intensity recorded in this interval. Since it has been shown that paramagnetic susceptibility rarely exceeds 350×10^{-6} SI in sediments (Rochette, 1987), this may explain the origin of the high susceptibility peaks (400×10^{-6} SI) above organic-rich layers in the interval 160–360 mbsf. XRD analysis revealed the presence of iron carbonates with strong paramagnetic signals like siderite ($FeCO_3$) and ankerite ($Ca(Mg, Fe)(CO_3)_2$) above organic-rich layers (see "Lithostratigraphy" section, this chapter). We have measured K, K_{arm} , and $-IRM_{0.1T}/SIRM$ of siderite and ankerite from the shipboard mineral collection (Table 9). The last two parameters are related to small remanence carrier inclusions within the crystal. Ankerite has a mean susceptibility (1.5×10^{-4} SI), one order of magnitude below siderite (40×10^{-4} SI). Therefore, siderite could be a candidate for bearing strong paramagnetic susceptibility. Preliminary measurements of anisotropy of magnetic susceptibility, however, show that magnetic fabric of the samples having a susceptibility peak is normal (K_3 perpendicular to the bedding), and not inverse (interchange of K_1 and K_3) as would be expected if siderite is the dominant source of the magnetic susceptibility (Rochette et al., 1992).

STRUCTURAL GEOLOGY

The Pliocene to Pleistocene sequence cored at Site 977 is mainly poorly consolidated sediment, which therefore shows considerable drilling-induced deformation, including zones of downward drag ~1 cm wide on each side of the APC cores (up to Core 977A-17H). Extensive drilling-induced biscuit structures occur in the remaining XCB cores (977A-18X to 63X). From about 275 to 300 mbsf, sediments are more consolidated (see "Physical Properties" section, this chapter).

The dip of the bedding is close to horizontal throughout the entire hole, except for some meter-scale changes caused by slumping (Cores 977A-12H, 48X and 50X). In the Pleistocene sequence there are layers with a chaotic texture (e.g., Core 977A-11H), probably caused by slumping. A well-developed east-facing (in core coordinates) slump fold in the Pliocene sequence is shown in Figure 14 (interval 977A-48X-6, 27–48 cm). Structures associated with these slump folds include millimeter to centimeter scale reverse and normal faults, folded faults, and disharmonic folds with thickened hinge zones (Fig. 29, interval 977A-48X-7, 11–22 cm; Fig. 30). In the core of some slump folds, mud has been squeezed out along the hinge zone. Refolding and boudinage, probably syngenetic, are also observed along shear zones associated with the slumping.

The JOIDES Resolution seismic profile collected during the site approach (see "Background and Objectives" section, this chapter) suggests that there was little tectonic activity during the Pliocene and

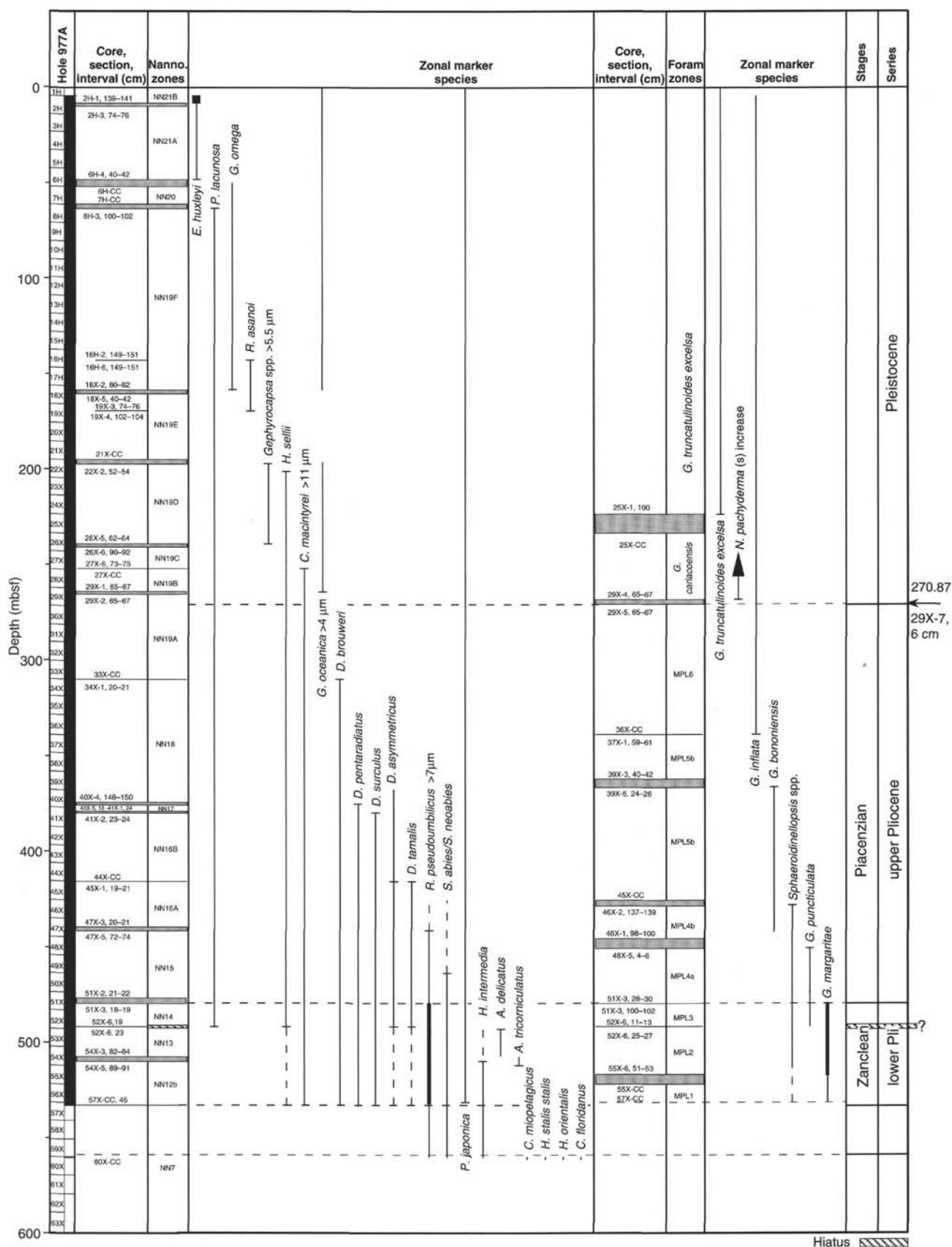


Figure 23. Summary of nannofossil and foraminiferal zonation of Hole 977A. Bold lines represent acme intervals. Lack of a short horizontal line at the end of a species' vertical range line indicates that the range of that species is incomplete. Shaded areas represent intervals not sampled.

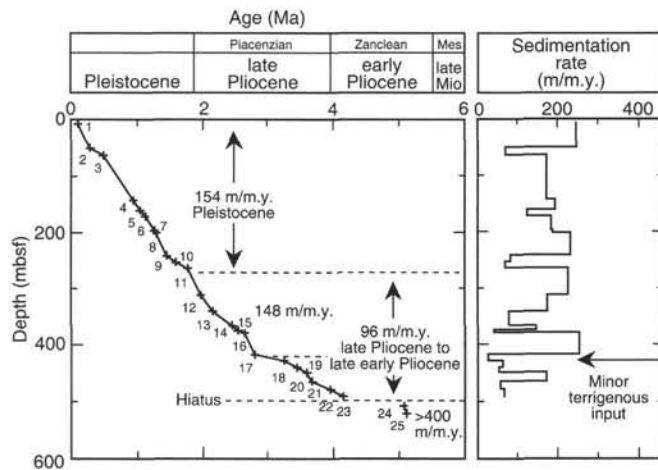


Figure 24. Sedimentation rates at Hole 977A.

Pleistocene in the basin between the Yusuf Ridge and Al-Mansour Seamount, in which Site 977 was located. The only sign of deformation near the site is a very low-amplitude fold that has propagated up to the seafloor above a fault in the underlying Miocene sequence, about 4 km east of the site. The Yusuf Ridge to the south was tilted during this period, however, and in the basin to the south of the Yusuf Ridge, deformation and thickness changes in the Pliocene and Pleistocene sediments suggest that there was activity on the faults bounding the basin.

ORGANIC GEOCHEMISTRY

Calcium carbonate and organic carbon concentrations were measured on samples obtained regularly from Hole 977A. Organic matter atomic C/N ratios and Rock-Eval analyses were employed to determine the type of organic matter contained within the sediments. Analyses of extractable methyl alkenones were attempted to obtain estimates of sea-surface paleotemperatures. Elevated amounts of headspace gases were encountered, and routine monitoring of these gases was done for drilling safety.

Inorganic and Organic Carbon Concentrations

Concentrations of carbonate carbon vary between 2.5% and 7.5% in sediments from Site 977 (Table 10; Fig. 31). These carbonate carbon concentrations are equivalent to 21% to 62% sedimentary CaCO_3 , assuming that all of the carbonate is present as pure calcite. The range in carbonate contents reflects varying combinations of fluctuating biological productivity, dilution by non-carbonate sedimentary components, and post-depositional carbonate dissolution driven by oxidation of organic carbon during Pliocene–Pleistocene times.

Sediments at Site 977 average 0.55% TOC, which is nearly twice the ocean-drilling average of 0.3% compiled by McIver (1975) from DSDP Legs 1 through 33. TOC concentrations fluctuate between 0% and 2.5% (Table 10; Fig. 31). The sediments in which TOC concentrations are elevated resemble those referred to as sapropels at Sites 974 and 975. As such, their appearance at Site 977 is an important westward extension of sapropel deposition in the Mediterranean.

Organic Matter Source Characterization

Organic C/N ratios were calculated for Site 977 samples using TOC and total nitrogen concentrations to help identify the origin of

their organic matter. Site 977 C/N ratios vary from <5 to 21 (Table 10). The low C/N ratios occur in samples especially low in organic carbon and are not accurate indicators of organic matter source. These values are probably an artifact of the low carbon content combined with the tendency of clay minerals to absorb ammonium ions generated during the degradation of organic matter (Müller, 1977).

The C/N ratios of 28 samples containing a minimum of 1% TOC average 10.1, which is a value that is intermediate between unaltered algal organic matter and fresh land-plant material (e.g., Emerson and Hedges, 1988; Meyers, 1994). It is likely that these organic-carbon-rich sediments contain partially degraded algal material with some admixed continental organic matter. Preferential loss of nitrogen-rich, proteinaceous matter can elevate the C/N ratios of algal organic matter during settling to the seafloor.

Sediment samples having relatively elevated TOC concentrations were selected for Rock-Eval characterization of the type and thermal maturity of their organic matter contents (Table 11). A van Krevelen-type plot of the HI and OI values suggests that the sediments contain mostly Type III (land-derived) organic matter (Fig. 32). This source assignment for the organic matter conflicts, however, with the relatively low C/N ratios for these samples, which indicate that the organic matter is predominantly marine material. The contradiction between the Rock-Eval source characterization and the elemental source characterization is evidence that the marine organic matter has been heavily oxidized, probably by microbial reworking. Well-preserved Type II organic matter has high hydrogen index values (Espitalié et al., 1977).

Rock-Eval T_{max} values are relatively low in the upper 200 m of Hole 977A, but they become elevated below this depth (Fig. 33). These values indicate that organic matter in the upper section is thermally immature with respect to petroleum generation, whereas it is overmature in the deeper sediments. The temperatures needed to achieve the degree of maturity evident in the deeper section would range between 125°C and 150°C, which is substantially greater than present bottom-hole temperatures (see "In Situ Temperature Measurements" section, this chapter). The thermal maturity of the organic matter in sediments below 200 mbsf consequently suggests that heat flows may have been higher in the past at Site 977.

Alkenone Paleotemperature Estimates

Samples containing at least 1% TOC were selected from Hole 977A for extraction and analysis of their C_{37} alkenone biomarkers and calculation of sea-surface paleotemperatures. Organic matter in these samples contained too little extractable material to provide useful alkenone data. The absence of measurable alkenones contrasts with sapropel layers present elsewhere in the Mediterranean and indicates that the organic matter present at Site 977 is not as well preserved.

Headspace Gases

Concentrations of headspace methane are high in sediments from Hole 977A (Fig. 34). Two sources of the gas are possible. First, gas from some deeper origin may have migrated into the unit. Evidence for migration of methane into porous sediments from deeper sources has been found at Sites 762 and 763 on the Exmouth Plateau (off northwest Australia) where a known thermogenic source exists in underlying Jurassic rocks (Meyers and Snowdon, 1993). No comparable source of gas is known on the southern margin of Iberia. A second possibility is in situ formation by methanogenic bacteria. High C_1/C_2 ratios (Table 12) indicate that the methane is biogenic, as opposed to thermogenic, in origin. The source of the methane is probably from in situ microbial fermentation of the marine organic matter present in the sediments at Site 977. Similar microbial production of methane from marine organic matter has been inferred from high biogenic gas

Table 5. Age of calcareous nannofossil and planktonic foraminiferal biostratigraphic events and depth of their occurrence in Hole 977A.

		Biostratigraphic event	Age (Ma)	Depth (mbsf)		
				Top	Bottom	Mean
1	Base	<i>E. huxleyi</i> acme	0.085	5.41	7.67	6.54
2	FO	<i>E. huxleyi</i>	0.26	46.92	52.08	49.50
3	LO	<i>P. lacunosa</i>	0.46	61.48	65.00	63.24
4	LO	<i>R. asanoi</i>	0.93	140.01	145.99	143.00
5	FO	<i>G. omega</i> >4.0 μ m	1.02	158.32	162.40	160.36
6	FO	<i>R. asanoi</i>	1.10	169.36	171.12	170.24
7	LO	<i>Gephyrocapsa</i> spp. >5.5 μ m	1.24	194.79	196.42	195.61
8	LO	<i>H. sellii</i>	1.27	199.75	202.62	201.19
9	FO	<i>Gephyrocapsa</i> spp. >5.5 μ m	1.44	239.52	241.30	240.41
10	LO	<i>C. macintyreii</i> >11 μ m	1.58	250.83	252.53	251.68
11	FO	<i>G. caribbeanica</i> >4.0 μ m	1.75	262.45	263.95	263.20
		Pliocene/Pleistocene boundary	1.83			270.87
12	LO	<i>D. brouweri</i>	1.96	309.75	309.90	309.83
13	FO	<i>G. inflata</i>	2.13	338.78	339.09	338.94
14	LO	<i>G. bononiensis</i>	2.45	361.32	365.66	363.49
15	LO	<i>D. pentaradiatus</i>	2.52	373.48	373.68	373.58
16	LO	<i>D. surculus</i>	2.63	373.68	378.83	376.25
17	LO	<i>D. tamalis</i>	2.78	415.83	415.79	415.81
18	LO	<i>Sphaeroidinellopsis</i> spp.	3.22	425.43	428.19	426.81
19	LO	<i>R. pseudoumbilicus</i> >7 μ m	3.43	438.10	441.62	439.86
20	LO	<i>G. puncticulata</i>	3.57	445.98	449.04	447.51
21	LO	<i>S. abies</i>	3.66	460.98	464.03	462.51
22	LCO	<i>G. margaritae</i> /LCO <i>R. pseudoumbilicus</i> >7.0 μ m	3.94	475.01	476.48	475.74
23	FCO	<i>D. asymmetricus</i>	4.13	490.59	490.63	490.61
24	LcO	<i>H. intermedia</i>	5.07	505.92	508.99	507.45
25	FCO	<i>G. margaritae</i>	5.10	531.27	531.27	531.27

Notes: FO = first occurrence, LO = last occurrence, LCO = last common occurrence, FCO = first common occurrence, LcO = last consistent occurrence; also indicated are the main chronostratigraphic boundaries. This table is also on the CD-ROM, back pocket, this volume.

Table 6. Azimuthal orientation of APC cores from Hole 977A using Tensor tool data.

Core	Magnetic toolface (MTF) ($^{\circ}$)
161-977A-	
3H	78
4H	280
5H	105
6H	—
7H	67
8H	9
9H	117
10H	129
11H	331
12H	—
13H	—
14H	—
15H	189
16H	313
17H	290

Notes: The orientation parameter (MFT) is an angle between true north and x-axis of the core-coordinate. Cores 977A-6H, 12H, 13H, and 14H failed to recover stable readings.

concentrations in Pliocene–Pleistocene sediments from Site 532 on the Walvis Ridge (Meyers and Brassell, 1985), Sites 897 and 898 on the Iberian Abyssal Plain (Meyers and Shaw, in press), Site 976 nearby in the Alboran Sea (this volume), and also in middle Miocene sediments from Site 767 in the Celebes Sea (Shipboard Scientific Party, 1990). A biogenic origin of the methane is supported by the disappearance of interstitial sulfate at approximately the same sub-bottom depth where methane concentrations begin to rise (see “Inorganic Geochemistry” section, this chapter). As noted by Claypool and Kvenvolden (1983), the presence of interstitial sulfate inhibits methanogenesis in marine sediments.

Higher molecular weight thermogenic headspace gases are also present at Site 977. Concentrations of propane, *iso*-butane, and *iso*-pentane exceed those of ethane in sediments from about 200 mbsf to 450 mbsf (Table 12). A general correspondence between elevated

Rock-Eval T_{max} values and appearance of these heavier gases (Figs. 33, 34) suggests that the C_3 , C_4 , and C_5 gases were produced by thermal degradation of sedimentary organic matter during some former period of elevated heat flow in this sub-basin of the Alboran Sea.

INORGANIC GEOCHEMISTRY

Nineteen interstitial water samples were recovered from Site 977A between 1.45 and 506.50 mbsf, one sample per core in the uppermost 50 m mbsf and one every third core below. The resulting interstitial water profiles are dominated by two main processes: carbonate diagenesis and organic matter degradation.

Carbonate Diagenesis

Calcium concentrations decrease from approximate seawater values of 10–11 mM at 1.45 mbsf to about 4 mM between 17.95 and 46.45 mbsf, remain below seawater concentrations until 247 mbsf, then increase to nearly eight times seawater concentrations at 506.50 mbsf (Table 13; Fig. 35C). Magnesium decreases from seawater concentrations at the surface to 35 mM below 74.95 mbsf (Fig. 35D). The calcium and magnesium decrease in the zone of increased alkalinity indicates dolomite or high magnesium calcite precipitation. This inferred precipitation is supported by the presence of authigenic calcite rhombs in Cores 977A-2H, 3H, and 4H (see “Lithostratigraphy” section, this chapter). Carbonate recrystallization at depth is suggested by the increase in strontium concentrations from around 100 μ M in the top 37 m to 1437 μ M at 477.70 mbsf (Fig. 36C). Biogenic calcium carbonate is rich in strontium; however, this strontium is forced from the crystal lattice upon recrystallization (Deer et al., 1966). The slight decrease in strontium at 506.50 mbsf may reflect strontium uptake in a strontium-bearing phase. The consistent magnesium concentrations below 74.95 mbsf indicate that magnesium is not being consumed in any reactions. The increase in calcium concentrations toward the base of the hole suggests supply of calcium from depth.

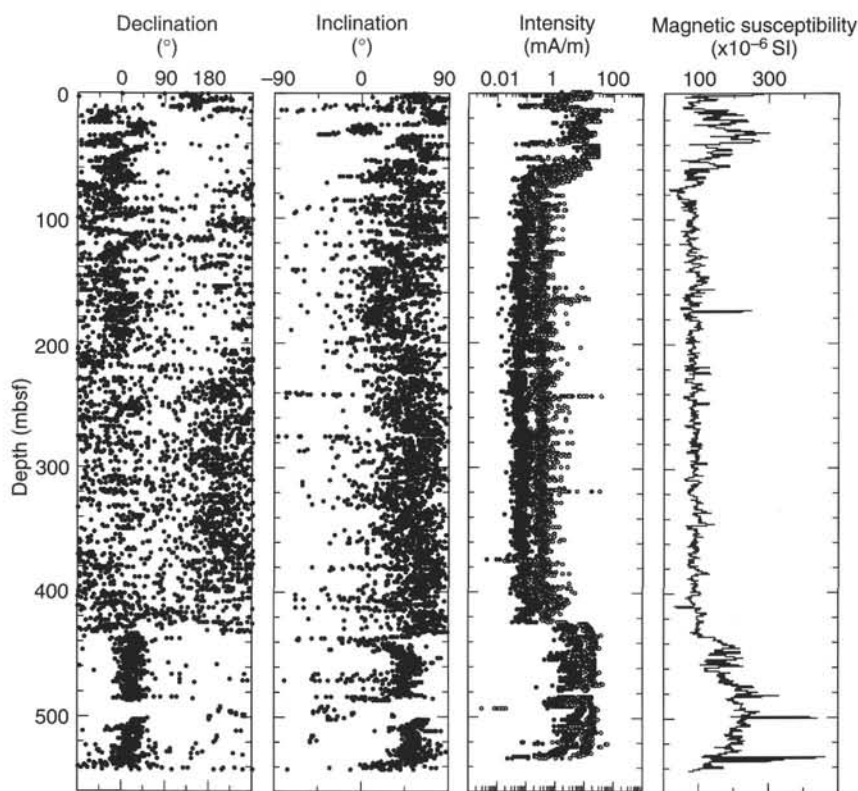


Figure 25. Declination (core-coordinate), inclination, and intensity after 15 mT AF demagnetization for Hole 977A. Open circles on the intensity diagrams indicate intensity before demagnetization. Low-field susceptibility measured on MST is shown after smoothing with window of 20 points.

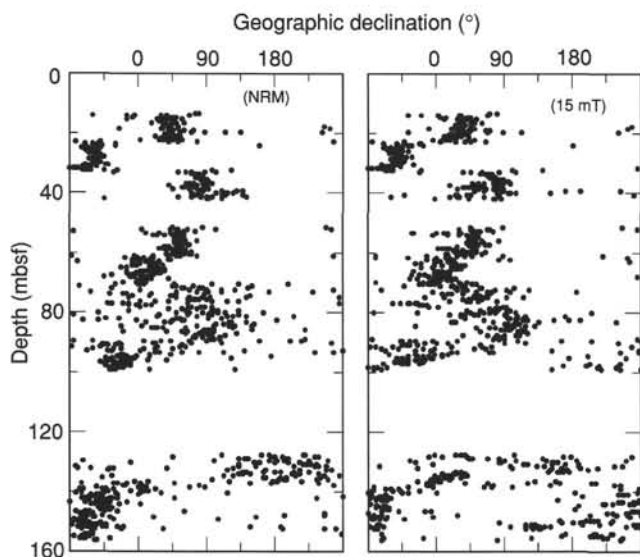


Figure 26. Reoriented declination by using Tensor tool data (Table 6) for APC cores in Hole 977A before and after AF demagnetization.

Organic Matter Degradation

The rapid sediment accumulation rates at this site (approximately 135 m/m.y.; see "Biostratigraphy" section, this chapter) ensure that organic matter is buried more rapidly than dissolved oxygen can penetrate from the overlying seawater. Therefore, only the uppermost few tens of centimeters of the cored interval are oxic (as evidenced by a thin brown veneer in the top of Core 977A-1H). Below this layer, bacterial degradation of organic matter proceeds through utiliza-

tion of nitrate, manganese and iron oxyhydroxides, sulfate, and finally carbon dioxide.

This sequence is reflected in the manganese and sulfate profiles. The Mn^{2+} profile (Fig. 37C) peaks at $24 \mu M$ at 1.45 mbsf and then decreases rapidly to a background of about $6 \mu M$ by 27.45 mbsf. Below 275.80 mbsf Mn^{2+} concentrations are below the lower limit of detection ($<5 \mu M$). This profile indicates that the manganese reduction zone is located in the upper meter of the sediment. Sulfate decreases rapidly from seawater concentrations at 2.95 mbsf to reach zero at 46.45 mbsf, but increases in the deepest samples (Fig. 37A). The constant SO_4^{2-} concentration in the top two samples (Table 13) indicates that SO_4^{2-} reduction is not occurring in the uppermost three meters: this is the zone of manganese and iron reduction. The depletion of SO_4^{2-} is accompanied by an increase in headspace methane concentrations from <300 ppm in the upper 36 m to 35,695 ppm at 122.45 mbsf (see "Organic Geochemistry" section, this chapter). This indicates the development of methanogenesis, which, because of the greater amount of free energy yielded by SO_4^{2-} reduction, only commences after SO_4^{2-} is depleted (Claypool and Kvenvolden, 1983).

The rapid rate of organic matter degradation is reflected in the profiles of three other species. Alkalinity concentrations increase from slightly higher than seawater concentrations at 1.45 mbsf, to 15 mM at 27.45 mbsf, before decreasing toward the base of the hole (Fig. 35B). Phosphate concentrations show a distinct peak of $56 \mu M$ between 6.88 and 9.88 mbsf before decreasing rapidly to about $9 \mu M$ at 46.45 mbsf (Fig. 38B). In contrast to alkalinity and phosphate, ammonium increases rapidly in the top 10 m, peaks at $3937 \mu M$ at 218 mbsf, and then decreases to the base of the hole (Fig. 38A). The phosphate and alkalinity profiles track the rapid degradation of organic matter in the upper 50 m of the cored interval, whereas the ammonium concentration is also influenced by degradation of organic matter by methanogenic bacteria. The ammonium maximum is surprisingly deep, considering methanogenesis commences at about 45 mbsf. However, the it is coincident with a CH_4 peak (see "Organic Geochemistry" section, this chapter). The core in which the ammoni-

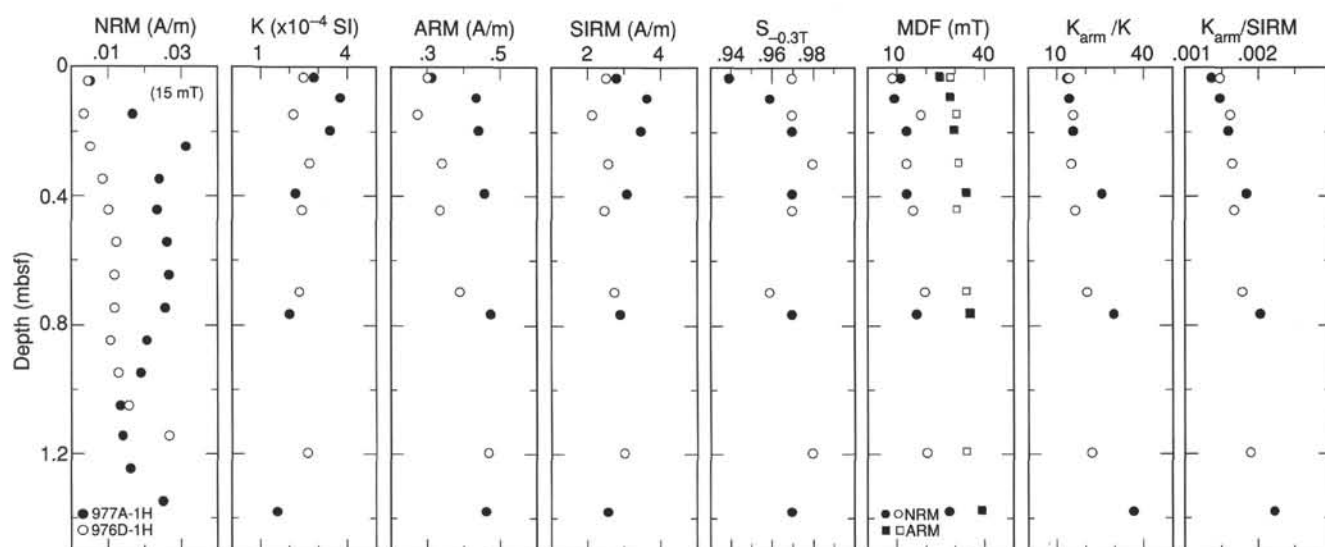


Figure 27. Rock-magnetic parameters from Core 977A-1H are plotted with closed symbols. Open symbols are for Core 976D-1H as a reference. Data are listed in Table 7.

Table 7. Rock-magnetic parameters from Cores 977A-1H and 976D-1H.

Core, section, interval (cm)	Depth	MDF _{NRM}	ARM	MDF _{ARM}	SIRM	S _{-0.3T}	K _{arm}	K	K _{arm} /K	K _{arm} /SIRM
161-977A-										
IH-1, 4	0.04	11.9	0.3167	25.8	2.842	0.94	3.980E-3	2.857E-4	13.9	1.40E-3
IH-1, 10	0.10	9.6	0.4408	29.0	3.691	0.96	5.539E-3	3.771E-4	14.7	1.50E-3
IH-1, 20	0.20	13.6	0.4463	30.6	3.485	0.97	5.609E-3	3.443E-4	16.3	1.61E-3
IH-1, 40	0.40	13.9	0.4630	34.4	3.130	0.97	5.818E-3	2.243E-4	25.9	1.86E-3
IH-1, 77	0.77	17.5	0.4800	36.0	2.939	0.97	6.031E-3	2.014E-4	29.9	2.05E-3
IH-1, 138	1.38	28.5	0.4672	40.0	2.624	0.97	5.871E-3	1.586E-4	37.0	2.24E-3
IH-3, 18	3.18	32.0	0.2872	34.3	1.960	0.96	3.609E-3	1.400E-4	25.8	1.84E-3
161-976D-										
IH-1, 4	0.04	9.1	0.3041	28.9	2.537	0.97	3.821E-3	2.529E-4	15.1	1.506E-3
IH-1, 15	0.15	18.6	0.2796	31.0	2.151	0.97	3.513E-3	2.157E-4	16.3	1.633E-3
IH-1, 30	0.30	13.6	0.3420	31.7	2.599	0.98	4.297E-3	2.757E-4	15.6	1.653E-3
IH-1, 45	0.45	16.0	0.3364	31.0	2.510	0.97	4.227E-3	2.486E-4	17.0	1.684E-3
IH-1, 70	0.70	20.0	0.3949	34.9	2.757	0.96	4.962E-3	2.371E-4	20.9	1.800E-3
IH-1, 120	1.20	20.6	0.4705	34.8	3.080	0.98	5.912E-3	2.657E-4	22.3	1.919E-3

Notes: NRM intensities are from archive halves. Units are as follows: MDF_{NRM} and MDF_{ARM} in mT; ARM and SIRM in A/m; K_{arm} and K in SI. See "Explanatory Notes" chapter, this volume, for details.

um maximum occurs (Core 977A-24X) contains four dark-colored layers, some of which overlie a series of opaque-rich sandy silts (see "Lithostratigraphy" section, this chapter). Such layers may be the result of redeposited sediments rich in organic matter. The rapid burial of these sediments would have resulted in only minor oxic and sub-oxic degradation of the organic matter; hence, fairly reactive organic matter would be preserved in these intervals. This would be degraded by methanogenic bacteria, which is evidenced by both the CH₄ and ammonium profiles.

The downcore decrease in ammonium concentrations can be ascribed to ion-exchange reactions with clay minerals with a concomitant lithium release. Part of the increase in lithium from near seawater concentrations at 1.45 mbsf to 202 μM at 477.70 mbsf may reflect such a release (Fig. 36D). However, an additional source is required to fully account for the strong enrichment in lithium relative to seawater concentrations.

Evidence for Evaporite-Related Fluids

Salinity decreases slightly in the upper section of the hole because of sulfate reduction, remains below seawater concentrations until 362.30 mbsf, and then increases to 46‰ at 506.50 mbsf (Fig. 36A). Chlorinity remains <620 mM to 218 mbsf, increasing to 778 mM at

506.50 mbsf (Fig. 36B). Sodium decreases to a minimum at 103.45 mbsf, and then increases to 578 mM at 506.50 mbsf (Fig. 37D). Lithium increases from surface concentrations to 202 μM at 477.70 mbsf. These concentrations are considerably lower than those reported from the sites underlain by evaporite sequences (see Site 975 "Inorganic Geochemistry" section, this volume); however, such increases do indicate the influence of brine fluids. They may reflect the presence of a paleo-fluid that has been trapped under the rapidly accumulating Pliocene–Pleistocene sequence, but such a source is unlikely to account for the enhanced lithium concentrations. An alternative, more credible scenario would be migration of evaporitic brines from another section of the basin. The increase in calcium and the enhanced sulfate concentration toward the base of the cored interval suggest that this brine may originate from dissolution of gypsum. The concave nature of some of the profiles (Cl⁻, Na⁺, salinity) suggests this brine has not been present for a sufficient period for steady-state diffusion to develop.

Silica and Potassium

The silica profile exhibits a steep increase in the upper few meters, then gradually decreases with depth except for a peak at 103.45 mbsf (Fig. 38C). Dissolution of the diatomaceous ooze at 117.50 mbsf (see

Table 8. Rock-magnetic parameters.

Core, section	Top (cm)	Depth (mbsf)	K	K _{arm}	SIRM	S _{-0.3T}	IRM _{0.1T} /SIRM
161-977A-							
17H-3	130	150.80	75.8	42.3	30.9	0.96	0.32
17H-6	101	155.01	80.8	35.5	30.4	0.90	
19X-4	70	170.80	482.9	20.5	21.6	0.94	
19X-4	73	170.83	507.9	15.9	14.1	0.91	
19X-4	127	171.37	61.4	23.4	33.6	0.92	
23X-6	134	212.84	75.0	26.9	30.3	0.92	0.33
24X-1	144	215.04	465.0	8.5	28.3	0.92	
28X-3	14	255.31	73.6	8.5	29.6	0.88	
28X-3	20	255.37	150.8	31.0	28.1	0.97	0.47
28X-3	20	255.37	157.9	9.8	26.6	0.95	
28X-3	24	255.41	137.1	21.4	32.4	0.95	
29X-6	93	270.23	83.3	29.4	31.2	0.93	0.40
30X-4	136	277.26	89.2	36.1	35.7	0.94	0.54
31X-4	127	286.77	85.8	25.1	25.1	0.93	0.37
34X-4	138	315.58	103.3	36.7	47.8	0.94	0.44
35X-4	135	325.25	51.7	25.7	24.6	0.94	
37X-3	98	342.40	100.0	23.9	41.1	1.00	
38X-6	26	355.96	129.3	27.6	52.0	0.96	
39X-4	70	363.10	68.6	22.1	44.0	0.93	
46X-5	96	432.26	165.7	4099.0	1310.0	0.96	
47X-3	103	438.93	387.1	5919.0	3830.0	0.97	
48X-4	25	449.25	475.7	4286.0	2780.0	0.98	
51X-1	29	473.59	165.7	3530.0	1570.0	0.97	
51X-1	120	474.50	925.7	16254.0	33500.0	0.94	
51X-2	19	474.99	199.3	4384.0	1870.0	0.98	
52X-5	72	489.62	151.4	3490.0	1600.0	0.98	
52X-5	88	489.78	215.7	3021.0	1650.0	0.98	
52X-5	95	489.85	655.0	6085.0	7280.0	0.98	
54X-6	101	510.61	228.3	4000.0	2032.0	0.96	0.78
54X-6	101	510.61	260.0	3460.0	2150.0	0.95	
55X-3	50	515.30	140.8	2470.0	1375.0	0.96	0.76
55X-3	56	515.36	108.3	3600.0	1116.0	0.97	0.80
55X-3	75	515.55	215.0	2800.0	1160.0	0.97	0.83
56X-4	81	526.71	1265.0	2302.0	11906.0	0.99	0.86

Notes: K and K_{arm} are 10⁻⁶ SI. SIRM (m/Am).

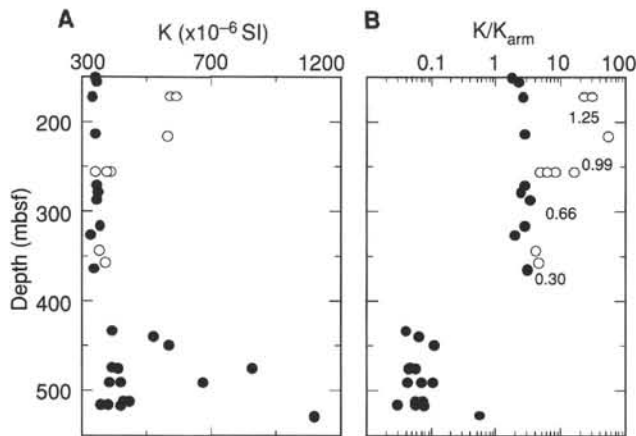


Figure 28. **A.** Magnetic susceptibility (K) vs. depth (mbsf). **B.** K/K_{arm} vs. depth (K_{arm} = anhysteretic remanence susceptibility). Open circles correspond to peaks related to organic-rich layers. Numbers beside symbols give TOC recorded just below the susceptibility peak.

“Lithostratigraphy” section, this chapter) likely provides the source for the lower silica peak. Furthermore, it is possible that dissolution of this diatomaceous layer is the cause of the steepening in the lithium gradient. The origin of the upper silica peak is not so apparent. Silica concentrations generally increase rapidly in the upper few meters of the sediment column, reflecting the corrosive nature of seawater toward biogenic silica. However, an increase to concentrations of almost 1 mM is unlikely in this area, given the generally low abundance of siliceous plankton in the Mediterranean. Potassium concentrations decrease from slightly higher than seawater concentrations at

Table 9. Rock-magnetic properties of natural siderite (Mont Saint Hilaire, Quebec, Canada) and ankerite (Eagle Mine, Gilman, CO).

Mineral	K	K _{arm}	SIRM	IRM _{0.1T} /SIRM
Siderite powder	1000	25	240	0.10
Siderite crystal	4193	65	162	0.60
Siderite crystal	4420	10	51	0.57
Ankerite powder	150	20	33	0.58

Note: Same convention as in Table 8.

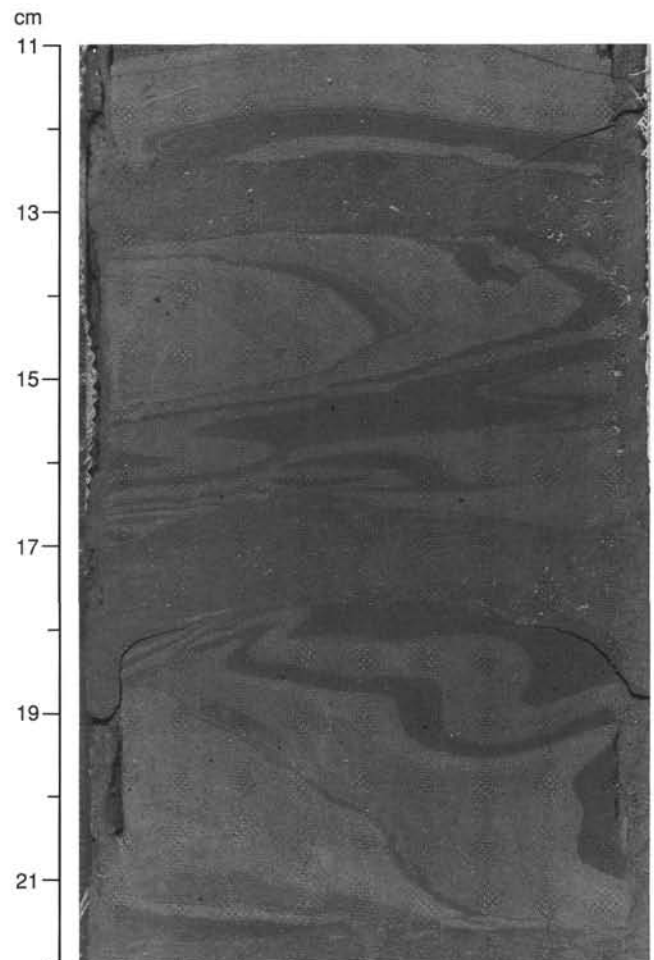


Figure 29. Isoclinal to asymmetric folds associated with slumping in Pliocene clay (interval 977A-48X-7, 11–22 cm). Note thickening of the hinge zone and millimeter-scale normal faults.

the top of the cored interval to 4 mM at 506.50 mbsf (Fig. 37C). Such a profile is typical for potassium in marine sediments and reflects potassium uptake by clay minerals.

Conclusions

The interstitial water profiles track the degradation of organic carbon in the upper sediments at Site 977 and suggest the presence of a brine toward the base of the hole. Organic carbon degradation occurs through oxygen, nitrate, and manganese reduction in the upper two meters, then by sulfate reduction to 46.45 mbsf. Below 46.45 mbsf organic matter degradation proceeds through the action of methanogenic bacteria. Increases in calcium and sulfate toward the base of the

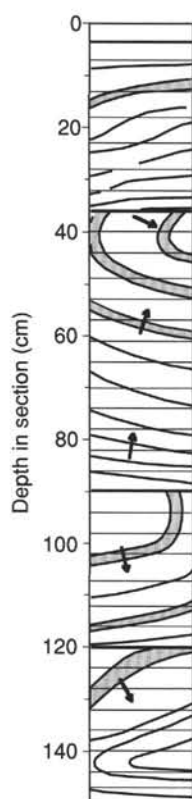


Figure 30. Reconstruction of the slump in Section 977A-48X-6, shown in Figure 14. Arrows point toward younging direction. Thick horizontal lines show inferred position of fault surfaces associated with slumping. Thin lines give boundaries between biscuits, which are illustrated rotated back to their original positions.

hole interval suggest the brine may originate from gypsum dissolution.

PHYSICAL PROPERTIES

Introduction

Physical property measurements were made on whole-core sections (for MST and thermal conductivity measurements), split cores (for sonic velocity measurements), and discrete samples (for index properties) for Site 977. Natural gamma ray was measured at 10-cm intervals on cores as part of the MST. MST and thermal conductivity measurements were made on every section. Index properties were measured once per section until Core 977A-27X and every other section from Core 977A-28X onwards. The MST velocity was measured for only the APC cores. Velocity measurements using DSV and Hamilton frame transducers were made on every section. The general quality of the data for Site 977 was good because we did not find gas in the cores as was the case for Site 976.

Multisensor Track (MST)

The slight offset of susceptibility, density, and natural gamma data (Fig. 39) at around 150 mbsf is because of the change in coring from APC to XCB. The relatively large susceptibility values in the shallow part of the hole (0–60 mbsf) is possibly due to the increased terrigenous input to the sediments (see “Lithostratigraphy” section, this chapter). There is an increase in susceptibility at around 410–520 mbsf that coincides with a decrease in sedimentation rate from 146

m/m.y. in the late Pliocene to 58 m/m.y. in the late early Pliocene (Fig. 24). The zone of higher susceptibility overlaps with an interval of increased terrigenous sediment input from 420–485 mbsf but continues below it (485–540 mbsf).

Thermal Conductivity

Thermal conductivity results for Hole 977A are shown in Figure 40 and listed in Table 14 (on CD-ROM). The data are scattered between 1.0 and 1.5 W/(m·K). There is a slight increase in the first 50 mbsf, with a slow increase below this depth.

Index Properties

Index properties: bulk density, porosity, and void ratio, show a minimum in their values centered around 150 mbsf (Fig. 41; Table 15 on CD-ROM), corresponding to the change in the coring technique mentioned above.

The grain densities are almost constant with depth (Fig. 41), perhaps because the biogenic silica components in the sediments are not present in large amounts.

Bulk density increases rapidly with depth in the uppermost 50 mbsf, and increases at a slower rate below that. This is caused by compaction and water expulsion in the shallow part of the sediments. The porosity and void ratio values show similar trends.

The porosity is about 70% at the seafloor, and it rapidly decreases to 60% by 50 mbsf, reaching 30% at the bottom of the hole (Fig. 41).

P-wave Velocity

DSV and Hamilton frame P-wave velocity data is presented in Figure 42 and in Table 16 on CD-ROM. The velocity at the surface is about 1.5 km/s, which increases gradually to 2.2 km/s at around 540 mbsf. There are four gradients observed in the velocity data: the first reaching from the surface to ~50 mbsf, the second extending from 50 mbsf to ~400 mbsf, the third extending from 400 mbsf to ~500 mbsf, and the fourth from 500 mbsf to the bottom of the hole.

DOWNHOLE LOGGING

Operations

Log data were acquired at Hole 977A using the Quad combination (quad combo) and Formation MicroScanner (FMS) tools. Table 17 shows the intervals logged with each tool string and the data are shown in Figure 43. We encountered several bridges (borehole narrowing or obstructions), at 273, 304, and 335 mbsf while the quad combo was lowered to the bottom of the hole.

We ran the quad combo over a 500-m interval of the borehole. It showed that the borehole diameter exceeded 18 in (the caliper maximum) over most of the interval from 140.0 to 323.0 mbsf, because of washout (see “Operations” chapter, this volume). Several constrictions reduced the borehole diameter at 190, 210, 240, 295–303, 314–324, 335–340, and 472–478 mbsf.

The poor borehole conditions in the upper part of the hole made it impossible to run the FMS tool in that interval. We decided to set the end of the drill pipe at 405 mbsf to avoid most of the borehole constrictions and maximize the chance of success in FMS logging. The FMS obtained excellent images in the lower part of the hole including the transition zone between clays and sandy conglomerates. However, the hole conditions continued to deteriorate and we had considerable difficulty pulling the FMS tool back into the pipe. There was a possibility that the Lockable Flapper Valve at the end of the pipe was damaged or obstructed from properly functioning. Therefore, we decided not to run the geochemical logging string because of the danger of tools with nuclear sources becoming stuck in the hole.

Table 10. Results of inorganic and total carbon (TC) analyses of Pliocene–Pleistocene sediment samples from lithostratigraphic Unit I at Site 977.

Core, section, interval (cm)	Depth (mbsf)	Inorg. C (wt%)	CaCO ₃ (wt%)	TC (wt%)	TOC (wt%)	TN (wt%)	TS (wt%)	C/N
161-977A-								
1H-1, 6–7	0.06	3.61	30.1	4.12	0.51	0.13		4.58
1H-1, 89–90	0.89	4.79	39.9	5.18	0.39	0.12		3.79
1H-2, 64–65	2.14	4.24	35.3	5.11	0.87	0.17		5.97
1H-2, 96–97	2.46	4.39	36.6	5.09	0.70	0.16		5.10
1H-3, 48–49	3.48	4.45	37.1	4.73	0.28	0.11		2.97
2H-1, 59–60	4.59	3.49	29.1	3.73	0.24	0.11		2.55
2H-1, 103–104	5.03	3.06	25.5	3.55	0.49	0.12		4.76
2H-2, 38–39	5.81	3.93	32.7	4.80	0.87	0.16		6.34
2H-2, 76–77	6.19	3.62	30.2	4.43	0.81	0.21		4.50
2H-2, 113–114	6.56	4.10	34.2	4.89	0.79	0.22		4.19
2H-3, 25–26	7.18	3.87	32.2	4.89	1.02	0.18		6.61
2H-3, 136–137	8.29	3.81	31.7	4.49	0.68	0.14		5.67
2H-4, 36–37	8.79	4.09	34.1	4.83	0.74	0.14		6.17
2H-4, 84–85	9.27	4.02	33.5	4.89	0.87	0.16		6.34
2H-5, 7–8	10.00	4.55	37.9	5.61	1.06	0.24		5.15
2H-6, 60–61	12.03	4.71	39.2	5.78	1.07	0.17		7.34
2H-7, 50–51	13.43	4.36	36.3	4.25	0.00	0.12	0.00	0.00
3H-1, 37–38	13.87	5.14	42.8	5.79	0.65	0.10		7.58
3H-1, 95–96	14.45	5.19	43.2	5.86	0.67	0.09		8.69
3H-2, 45–46	15.45	4.98	41.5	5.74	0.76	0.13		6.82
3H-3, 24–25	16.74	5.15	42.9	5.75	0.60	0.12		5.83
3H-3, 45–46	16.95	5.47	45.6	6.00	0.53	0.13		4.76
3H-3, 85–86	17.35	5.35	44.6	5.89	0.54	0.12		5.25
3H-4, 38–39	18.38	4.50	37.5	5.43	0.93	0.16		6.78
3H-4, 73–74	18.73	4.15	34.6	4.58	0.43	0.11		4.56
3H-5, 27–28	19.77	4.57	38.1	5.70	1.13	0.17		7.75
3H-5, 44–45	19.94	4.21	35.1	4.80	0.59	0.14		4.92
3H-5, 145–146	20.95	3.88	32.3	4.76	0.88	0.20		5.13
3H-6, 21–22	21.21	4.87	40.6	5.47	0.60	0.13		5.38
3H-6, 74–75	21.74	4.48	37.3	4.94	0.46	0.11		4.88
3H-6, 94–95	21.94	5.28	44.0	5.75	0.47	0.11		4.98
4H-1, 37–38	23.37	4.73	39.4	5.86	1.13	0.22		5.99
4H-1, 128–129	24.28	4.91	40.9	5.70	0.79	0.15		6.14
4H-4, 106–107	28.56	4.38	36.5	4.62	0.24	0.10		2.80
4H-5, 106–107	30.06	3.44	28.7	3.82	0.38	0.16		2.77
4H-6, 3–4	30.53	4.02	33.5	5.00	0.98	0.15		7.62
4H-6, 10–11	30.60	3.95	32.9	5.08	1.13	0.21		6.28
5H-1, 42–43	32.92	4.27	35.6	5.53	1.26	0.19		7.74
5H-1, 56–57	33.06	4.19	34.9	5.19	1.00	0.17		6.86
5H-2, 69–70	34.69	5.13	42.7	5.58	0.45	0.11		4.77
5H-3, 74–75	36.24	3.07	25.6	3.48	0.41	0.13		3.68
5H-5, 45–46	38.95	4.90	40.8	5.97	1.07	0.22		5.67
5H-5, 64–65	39.14	4.24	35.3	4.78	0.54	0.12		5.25
5H-5, 103–104	39.53	4.45	37.1	5.36	0.91	0.13		8.17
5H-6, 80–81	40.80	4.01	33.4	4.30	0.29	0.06		5.64
6H-1, 16–17	42.16	4.64	38.7	5.19	0.55	0.09		7.13
6H-1, 65–66	42.65	3.71	30.9	3.98	0.27	0.07		4.50
6H-3, 130–131	46.30	7.37	61.4	7.51	0.14	0.05		3.27
6H-6, 41–42	49.91	6.05	50.4	6.43	0.38	0.06		7.39
7H-1, 66–67	52.16	6.37	53.1	7.24	0.87	0.10		10.15
7H-1, 76–77	52.26	6.30	52.5	7.14	0.84	0.10		9.80
7H-2, 2–3	53.02	3.96	33.0	4.82	0.86	0.12		8.36
7H-2, 83–84	53.83	4.04	33.7	4.45	0.41	0.06		7.97
7H-4, 36–37	56.36	4.09	34.1	4.29	0.20	0.05		4.67
7H-6, 93–94	59.93	6.93	57.7	7.20	0.27	0.05		6.30
8H-1, 49–50	61.49	5.40	45.0	5.82	0.42	0.07		7.00
8H-2, 114–115	63.64	6.48	54.0	6.70	0.22	0.05		5.13
8H-3, 19–20	64.19	6.66	55.5	6.83	0.17	0.05		3.97
8H-3, 64–65	64.64	5.81	48.4	6.06	0.25	0.05		5.83
8H-4, 67–68	66.17	5.76	48.0	6.33	0.57	0.13		5.12
8H-4, 82–83	66.32	5.20	43.3	5.75	0.55	0.09		7.13
8H-5, 17–18	67.17	5.19	43.2	5.99	0.80	0.11		8.48
8H-5, 36–37	67.36	5.45	45.4	5.63	0.18	0.12		1.75
8H-6, 83–84	69.33	5.20	43.3	5.56	0.36	0.12		3.50
9H-1, 56–57	71.06	5.24	43.6	5.63	0.39	0.13		3.50
9H-3, 76–77	74.26	6.58	54.8	6.79	0.21	0.05		4.90
9H-5, 78–79	77.28	5.45	45.4	7.16	1.71	0.23		8.67
9H-7, 27–28	79.80	6.31	52.6	7.01	0.70	0.09		9.07
10H-1, 35–36	80.35	6.38	53.1	6.95	0.57	0.14		4.75
10H-1, 143–144	81.43	5.58	46.5	6.76	1.18	0.13		10.59
10H-3, 26–27	83.26	3.38	28.2	3.83	0.45	0.09		5.83
10H-4, 31–32	84.81	4.32	36.0	5.33	1.01	0.12		9.82
10H-4, 121–122	85.71	6.68	55.6	7.00	0.32	0.06		6.22
10H-6, 55–56	88.05	3.67	30.6	4.16	0.49	0.13		4.40
11H-1, 141–142	90.91	5.40	45.0	6.18	0.78	0.15		6.07
11H-2, 133–134	92.33	3.45	28.7	4.84	1.39	0.14		11.58
11H-4, 82–83	94.82	3.16	26.3	5.24	2.08	0.19		12.77
11H-5, 104–105	96.54	3.91	32.6	4.31	0.40	0.08		5.83
12H-4, 4–5	103.54	5.19	43.2	5.77	0.58	0.15		4.51
12H-4, 43–44	103.93	4.71	39.2	5.38	0.67	0.09	0.55	8.69
12H-4, 63–64	104.13	4.36	36.3	5.23	0.87	0.12	0.63	8.46
12H-4, 99–100	104.49	4.24	35.3	4.81	0.57	0.09	0.61	7.39
12H-5, 112–113	106.12	4.24	35.3	4.41	0.17	0.06	0.05	3.31
12H-7, 5–6	108.05	5.24	43.6	5.63	0.39	0.08	0.10	5.69
13H-1, 42–43	108.92	5.02	41.8	5.25	0.23	0.07	0.18	3.83
13H-1, 50–51	109.00	4.60	38.3	5.73	1.13	0.12	0.72	10.99
13H-1, 80–81	109.30	4.49	37.4	5.31	0.82	0.11	0.66	8.70
13H-3, 17–18	111.67	4.30	35.8	5.07	0.77	0.10	1.05	8.98

Table 10 (continued).

Core, section, interval (cm)	Depth (mbsf)	Inorg. C (wt%)	CaCO ₃ (wt%)	TC (wt%)	TOC (wt%)	TN (wt%)	TS (wt%)	C/N
13H-4, 84-85	113.84	4.32	36.0	4.48	0.16	0.07	0.45	2.67
13H-5, 149-150	115.99	3.63	30.2	4.23	0.60	0.10	0.00	7.00
13H-7, 63-64	118.13	2.54	21.2	3.11	0.57	0.08	1.10	8.31
13H-CC, 16-17	118.30	3.13	26.1	3.76	0.63	0.08	0.13	9.19
13H-CC, 18-19	118.32	3.63	30.2	4.07	0.44	0.08	0.00	6.42
14H-1, 7-8	118.07	3.98	33.2	5.48	1.50	0.16	1.22	10.94
14H-1, 49-50	118.49	4.17	34.7	5.05	0.88	0.12	2.09	8.56
14H-1, 146-147	119.46	4.64	38.7	5.06	0.42	0.09	0.04	5.44
14H-2, 49-50	119.99	3.81	31.7	4.29	0.48	0.09	0.00	6.22
14H-3, 46-47	121.46	4.74	39.5	5.29	0.55	0.08	0.40	8.02
14H-4, 124-125	123.74	3.81	31.7	5.28	1.47	0.10	0.00	17.15
14H-5, 21-22	124.21	3.84	32.0	4.29	0.45	0.09	1.13	5.83
14H-6, 92-93	126.48	6.04	50.3	6.36	0.32	0.07	0.00	5.33
14H-6, 128-129	126.84	5.07	42.2	5.69	0.62	0.10	0.67	7.23
14H-7, 31-32	127.40	4.08	34.0	4.74	0.66	0.10	0.78	7.70
14H-7, 58-59	127.67	4.05	33.7	4.57	0.52	0.09	0.74	6.74
15H-1, 73-74	128.23	3.52	29.3	4.06	0.54	0.08	0.06	7.87
15H-3, 30-31	130.80	4.59	38.2	4.87	0.28	0.07	0.94	4.67
15H-4, 41-42	132.41	6.19	51.6	6.50	0.31	0.07	0.00	5.17
15H-5, 1-2	133.51	4.05	33.7	4.48	0.43	0.08	2.83	6.27
15H-5, 140-141	134.90	3.70	30.8	4.14	0.44	0.08	0.10	6.42
15H-6, 26-27	135.26	5.06	42.1	5.37	0.31	0.07	0.84	5.17
16H-1, 80-81	137.80	4.28	35.7	4.61	0.33	0.07	0.02	5.50
16H-2, 53-54	139.03	3.68	30.7	4.16	0.48	0.09	0.12	6.22
16H-3, 59-60	140.59	5.93	49.4	6.47	0.54	0.07	0.06	9.00
16H-3, 60-61	140.60	3.80	31.7	4.68	0.88	0.10	4.44	10.27
16H-3, 105-106	141.05	3.67	30.6	5.14	1.47	0.17	1.87	10.09
16H-4, 80-81	142.30	3.43	28.6	3.80	0.37	0.07	0.17	6.17
17H-2, 60-61	148.60	3.86	32.2	4.27	0.41	0.14	0.73	3.42
17H-4, 114-115	152.14	5.72	47.6	6.13	0.41	0.07	0.54	6.83
17H-5, 64-65	153.14	3.70	30.8	4.89	1.19	0.10	1.38	13.88
17H-5, 98-99	153.48	3.75	31.2	4.34	0.59	0.08	0.83	8.60
17H-5, 105-106	153.55	4.52	37.7	5.02	0.50	0.07	0.75	8.33
17H-5, 129-130	153.79	6.80	56.6	7.66	0.86	0.08	1.80	12.54
17H-5, 138-139	153.88	3.51	29.2	4.25	0.74	0.17	2.08	5.08
17H-5, 148-149	153.98	4.24	35.3	5.66	1.42	0.19	2.29	8.72
17H-6, 35-36	154.35	3.48	29.0	4.29	0.81	0.13	2.63	7.27
18X-1, 27-28	156.27	3.96	33.0	4.84	0.88	0.12	1.82	8.56
18X-1, 70-71	156.70	3.16	26.3	3.46	0.30	0.14	0.81	2.50
18X-1, 80-81	156.80	3.02	25.2	3.31	0.29	0.06	0.00	5.64
18X-3, 18-19	159.18	4.50	37.5	5.70	1.20	0.20	3.53	7.00
18X-3, 56-57	159.56	4.01	33.4	4.35	0.34	0.12	0.76	3.31
18X-4, 90-91	161.40	5.91	49.2	6.22	0.31	0.06	0.65	6.03
18X-4, 107-108	161.57	5.83	48.6	6.22	0.39	0.08	0.87	5.69
18X-6, 18-19	163.68	4.23	35.2	5.79	1.56	0.24	3.81	7.58
18X-6, 73-74	164.23	4.60	38.3	5.00	0.40	0.15	0.18	3.11
19X-1, 23-24	165.83	3.37	28.1	3.76	0.39	0.15	0.12	3.03
19X-3, 62-63	169.22	3.56	29.7	3.79	0.23	0.06	0.45	4.47
19X-4, 70-72	170.80	5.98	49.8	6.49	0.51	0.15	1.58	3.97
19X-4, 91-92	171.01	4.02	33.5	5.27	1.25	0.14	2.55	10.42
19X-6, 87-88	173.97	5.04	42.0	5.86	0.82	0.09	0.00	10.63
20X-1, 56-57	175.76	5.02	41.8	5.77	0.75	0.12	0.60	7.29
20X-2, 97-98	177.67	2.94	24.5	5.41	2.47	0.14	0.16	20.58
20X-3, 116-117	179.36	4.30	35.8	4.72	0.42	0.13	0.71	3.77
21X-1, 10-11	185.00	3.84	32.0	4.29	0.45	0.15	0.18	3.50
21X-1, 87-88	185.77	3.06	25.5	3.81	0.75	0.17	1.10	5.15
21X-1, 108-109	185.98	2.94	24.5	3.65	0.71	0.16	0.00	5.18
21X-1, 127-128	186.17	3.06	25.5	3.70	0.64	0.16	1.70	4.67
21X-3, 94-95	188.84	2.94	24.5	3.60	0.66	0.16	2.95	4.81
21X-4, 106-107	190.46	4.28	35.7	4.45	0.17	0.07	0.33	2.83
21X-4, 128-129	190.68	4.07	33.9	4.38	0.31	0.08	0.04	4.52
21X-7, 23-24	194.63	5.03	41.9	6.37	1.34	0.14	2.71	11.17
22X-1, 106-107	195.46	4.34	36.2	4.46	0.12	0.06	0.00	2.33
22X-2, 48-49	196.38	4.67	38.9	5.03	0.36	0.08	0.03	5.25
22X-3, 64-65	198.04	3.20	26.7	3.63	0.43	0.10	1.95	5.02
22X-5, 97-98	201.37	5.22	43.5	5.65	0.43	0.08	0.65	6.27
22X-6, 57-58	202.47	4.74	39.5	5.62	0.88	0.11	1.33	9.33
22X-7, 22-23	203.62	3.39	28.2	3.93	0.54	0.10	1.29	6.30
22X-CC, 34-35	204.16	4.41	36.7	4.72	0.31	0.07	0.08	5.17
23X-1, 63-64	204.63	4.80	40.0	6.30	1.50	0.17	1.70	10.29
23X-2, 59-60	206.09	4.51	37.6	4.98	0.47	0.09	1.86	6.09
23X-2, 83-84	206.33	5.44	45.3	4.65	0.00	0.17	0.91	0.00
23X-2, 99-100	206.49	4.91	40.9	5.62	0.71	0.10	0.90	8.28
23X-3, 11-12	207.11	3.95	32.9	4.34	0.39	0.08	0.57	5.69
23X-3, 69-70	207.69	4.57	38.1	4.92	0.35	0.08	0.61	5.10
23X-4, 49-50	208.99	3.47	28.9	3.96	0.49	0.09	0.81	6.35
23X-4, 118-119	209.68	4.32	36.0	4.74	0.42	0.08	0.71	6.13
23X-5, 59-60	210.59	3.52	29.3	4.30	0.78	0.09	1.32	10.11
23X-5, 95-96	210.95	4.36	36.3	4.81	0.45	0.07	0.07	7.50
23X-6, 34-35	211.84	4.09	34.1	4.84	0.75	0.10	0.29	8.75
23X-6, 74-75	212.24	3.02	25.2	3.30	0.28	0.07	0.81	4.67
23X-6, 103-104	212.53	4.32	36.0	4.78	0.46	0.09	0.27	5.96
23X-7, 11-12	213.11	5.13	42.7	5.46	0.33	0.09	0.10	4.28
23X-CC, 17-18	213.66	4.97	41.4	5.30	0.33	0.13	1.36	2.96
24X-1, 66-67	214.26	3.34	27.8	3.62	0.28	0.14	0.08	2.33
24X-2, 7-8	215.17	4.26	35.5	5.25	0.99	0.20	2.57	5.78
24X-2, 73-74	215.83	5.05	42.1	5.42	0.37	0.08	1.00	5.40
24X-4, 6-7	218.16	5.50	45.8	5.90	0.40	0.08	0.34	5.83
24X-4, 58-59	218.68	3.63	30.2	4.17	0.54	0.10	1.44	6.30
24X-4, 81-82	218.91	3.92	32.7	4.25	0.33	0.09	0.82	4.28
24X-4, 125-126	219.35	3.78	31.5	4.09	0.31	0.08	0.55	4.52

Table 10 (continued).

Core, section, interval (cm)	Depth (mbsf)	Inorg. C (wt%)	CaCO ₃ (wt%)	TC (wt%)	TOC (wt%)	TN (wt%)	TS (wt%)	C/N
24X-4, 139-140	219.49	3.37	28.1	3.64	0.27	0.08	0.09	3.94
24X-5, 15-16	219.75	5.30	44.1	5.49	0.19	0.07	0.60	3.17
24X-5, 49-50	220.09	3.80	31.7	4.25	0.45	0.14	0.47	3.75
25X-1, 107-108	224.27	4.88	40.7	5.14	0.26	0.14	0.65	2.17
25X-2, 14-15	224.87	4.92	41.0	5.48	0.56	0.10	1.14	6.53
25X-2, 48-49	225.21	4.94	41.2	5.41	0.47	0.05	0.00	10.97
25X-3, 45-46	226.68	4.81	40.1	5.35	0.54	0.09	0.05	7.00
25X-3, 95-96	227.18	3.60	30.0	4.56	0.96	0.08	1.69	14.00
25X-3, 132-133	227.55	2.93	24.4	3.58	0.65	0.10	0.93	7.58
25X-4, 18-19	227.91	2.67	22.2	3.24	0.57	0.10	0.53	6.65
25X-5, 107-108	230.30	4.93	41.1	5.56	0.63	0.05	0.71	14.70
26X-1, 21-22	233.11	3.92	32.7	4.53	0.61	0.11	0.55	6.47
26X-1, 90-91	233.80	3.92	32.7	4.95	1.03	0.11	0.08	10.92
26X-1, 115-116	234.05	4.35	36.2	4.97	0.62	0.11	0.28	6.58
26X-2, 20-21	234.60	3.25	27.1	3.63	0.38	0.05	0.80	8.87
26X-2, 49-50	234.89	4.26	35.5	4.88	0.62	0.09	1.68	8.04
26X-3, 26-27	236.16	5.19	43.2	5.66	0.47	0.05	0.10	10.97
26X-3, 113-114	237.03	5.40	45.0	5.89	0.49	0.10	0.06	5.72
26X-6, 20-21	240.60	4.35	36.2	4.98	0.63	0.09	0.66	8.17
26X-6, 36-37	240.76	4.34	36.2	4.84	0.50	0.09	0.16	6.48
26X-6, 55-56	240.95	4.35	36.2	4.83	0.48	0.09	0.50	6.22
27X-1, 84-85	243.44	4.22	35.2	4.62	0.40	0.05	0.03	9.33
27X-6, 44-45	250.54	5.09	42.4	5.61	0.52	0.05	0.50	12.13
28X-3, 58-59	255.75	4.44	37.0	5.10	0.66	0.10	0.67	7.70
28X-6, 35-36	260.02	4.32	36.0	4.94	0.62	0.11	0.45	6.58
28X-6, 75-76	260.42	9.07	75.6	9.51	0.44	0.02	0.68	25.67
29X-1, 61-62	262.41	4.64	38.7	5.13	0.49	0.10	0.15	5.72
29X-5, 129-130	269.09	3.14	26.2	3.83	0.69	0.12	1.49	6.71
29X-7, 14-15	270.94	4.56	38.0	5.16	0.60	0.05	0.83	14.00
30X-4, 78-79	276.68	4.51	37.6	5.03	0.52	0.05	0.18	12.13
30X-5, 67-68	278.07	3.43	28.6	4.01	0.58	0.12	0.17	5.64
30X-CC, 25-26	281.16	4.07	33.9	4.68	0.61	0.10	0.85	7.12
31X-2, 123-124	283.73	4.76	39.7	5.25	0.49	0.10	0.14	5.72
31X-6, 49-50	288.99	4.99	41.6	5.58	0.59	0.10	0.11	6.88
32X-1, 37-38	290.87	4.74	39.5	5.37	0.63	0.05	0.02	14.70
32X-4, 94-95	295.94	4.38	36.5	5.15	0.77	0.09	0.10	9.98
32X-6, 104-105	299.04	3.62	30.2	5.50	1.88	0.06	0.10	36.56
33X-2, 20-21	301.80	4.54	37.8	5.71	1.17	0.09	0.70	15.17
33X-4, 55-56	305.15	4.79	39.9	5.32	0.53	0.05	0.11	12.37
33X-5, 122-123	307.32	4.29	35.7	4.76	0.47	0.09	0.21	6.09
33X-6, 91-92	308.51	5.03	41.9	5.44	0.41	0.04	0.10	11.96
33X-6, 136-137	308.96	4.22	35.2	4.82	0.60	0.10	0.42	7.00
33X-CC, 15-16	309.25	4.59	38.2	5.06	0.47	0.09	0.16	6.09
34X-6, 44-46	317.64	5.04	42.0	5.53	0.49	0.12	0.13	4.76
34X-CC, 11-12	319.35	4.93	41.1	5.49	0.56	0.14	0.62	4.67
35X-2, 88-89	321.78	4.16	34.7	4.62	0.46	0.08	0.43	6.71
35X-3, 129-130	323.69	3.98	33.2	4.51	0.53	0.08	0.80	7.73
35X-4, 90-91	324.80	4.09	34.1	4.62	0.53	0.13	1.11	4.76
35X-6, 10-11	327.00	3.27	27.2	4.08	0.81	0.15	0.13	6.30
35X-CC, 19-20	329.09	3.70	30.8	4.10	0.40	0.08	0.46	5.83
36X-1, 35-36	329.25	4.30	35.8	4.67	0.37	0.13	0.12	3.32
36X-2, 44-45	330.84	3.98	33.2	4.45	0.47	0.08	0.78	6.85
36X-3, 39-40	332.29	3.92	32.7	4.42	0.50	0.08	0.57	7.29
36X-4, 26-27	333.66	4.09	34.1	4.67	0.58	0.08	0.28	8.46
36X-4, 126-127	334.66	4.62	38.5	5.13	0.51	0.13	0.07	4.58
36X-CC, 16-17	338.55	3.45	28.7	3.89	0.44	0.08	0.04	6.42
37X-1, 18-19	338.68	3.74	31.2	4.19	0.45	0.08	0.69	6.56
37X-3, 79-80	342.21	4.74	39.5	5.04	0.30	0.14	0.07	2.50
37X-4, 59-60	343.51	4.82	40.2	5.19	0.37	0.06	0.15	7.19
37X-CC, 24-25	348.21	4.39	36.6	5.15	0.76	0.10	0.22	8.87
38X-1, 27-28	348.47	4.83	40.2	5.31	0.48	0.08	0.53	7.00
38X-2, 86-87	350.56	4.63	38.6	4.98	0.35	0.07	0.73	5.83
38X-3, 80-81	352.00	3.95	32.9	4.31	0.36	0.07	0.80	6.00
38X-3, 113-114	352.33	5.22	43.5	5.49	0.27	0.13	0.07	2.42
38X-4, 43-44	353.13	4.82	40.2	5.30	0.48	0.13	0.53	4.31
38X-4, 140-141	354.10	5.45	45.4	5.73	0.28	0.12	1.11	2.72
38X-5, 77-78	354.97	5.47	45.6	5.90	0.43	0.07	0.03	7.17
38X-CC, 18-19	357.86	4.85	40.4	5.17	0.32	0.06	0.12	6.22
39X-3, 67-68	361.57	5.66	47.1	6.08	0.42	0.13	0.42	3.77
39X-5, 69-70	364.59	5.07	42.2	5.43	0.36	0.07	0.14	6.00
40X-2, 46-47	369.46	5.57	46.4	5.98	0.41	0.07	0.22	6.83
40X-3, 78-79	371.28	4.03	33.6	4.49	0.46	0.07	0.22	7.67
40X-4, 12-13	372.12	5.17	43.1	5.65	0.48	0.08	0.49	7.00
40X-5, 88-89	374.38	4.04	33.7	4.37	0.33	0.13	0.05	2.96
41X-1, 18-19	377.28	4.91	40.9	5.32	0.41	0.14	0.50	3.42
41X-2, 8-9	378.68	3.63	30.2	4.09	0.46	0.09	0.70	5.96
41X-7, 30-31	386.35	4.44	37.0	5.16	0.72	0.10	0.43	8.40
41X-7, 40-41	386.45	4.45	37.1	4.86	0.41	0.08	0.48	5.98
42X-1, 12-14	386.82	3.98	33.2	4.92	0.94	0.12	0.00	9.14
42X-1, 63-64	387.33	4.11	34.2	4.78	0.67	0.08	0.10	9.77
42X-1, 79-80	387.49	4.91	40.9	5.16	0.25	0.06	0.46	4.86
42X-3, 118-119	390.88	3.44	28.7	4.30	0.86	0.12	0.86	8.36
42X-4, 16-18	391.36	3.59	29.9	4.53	0.94	0.10	0.10	10.97
42X-4, 27-28	391.47	4.20	35.0	4.93	0.73	0.09	0.96	9.46
42X-4, 50-51	391.70	4.05	33.7	4.56	0.51	0.08	0.48	7.44
42X-6, 81-82	395.01	5.09	42.4	5.44	0.35	0.07	0.53	5.83
42X-6, 94-95	395.14	4.92	41.0	5.30	0.38	0.13	0.31	3.41
43X-4, 123-124	402.13	5.73	47.7	6.03	0.30	0.06	0.53	5.83
43X-6, 25-26	404.15	4.01	33.4	4.52	0.51	0.09	0.61	6.61
44X-3, 45-46	409.45	3.49	29.1	3.93	0.44	0.09	0.57	5.70
44X-4, 95-96	411.45	5.96	49.6	6.33	0.37	0.05	0.83	8.63

Table 10 (continued).

Core, section, interval (cm)	Depth (mbsf)	Inorg. C (wt%)	CaCO ₃ (wt%)	TC (wt%)	TOC (wt%)	TN (wt%)	TS (wt%)	C/N
44X-6, 106-107	414.56	4.76	39.7	5.33	0.57	0.13		5.12
44X-CC, 21-22	415.66	4.86	40.5	5.32	0.46	0.20		2.68
45X-1, 92-93	416.52	3.21	26.7	3.60	0.39	0.09		5.06
45X-3, 20-21	418.80	5.29	44.1	5.72	0.43	0.07		7.17
45X-4, 57-58	420.67	4.03	33.6	4.62	0.59	0.08		8.60
45X-5, 104-105	422.58	4.81	40.1	4.98	0.17	0.12		1.65
45X-5, 149-150	423.03	4.25	35.4	4.58	0.33	0.14		2.75
45X-6, 33-34	423.37	4.68	39.0	5.32	0.64	0.09		8.30
45X-7, 2-3	424.56	5.24	43.6	5.59	0.35	0.08		5.10
46X-2, 67-68	427.47	6.01	50.1	6.36	0.35	0.05		8.17
46X-3, 42-43	428.72	4.44	37.0	4.90	0.46	0.13		4.13
46X-3, 84-85	429.14	4.64	38.7	5.11	0.47	0.07		7.83
46X-4, 4-5	429.84	6.12	51.0	6.57	0.45	0.06		8.75
46X-4, 37-38	430.17	4.67	38.9	5.14	0.47	0.09		6.09
46X-5, 53-54	431.83	4.24	35.3	4.83	0.59	0.09		7.65
46X-6, 27-28	433.07	4.28	35.7	4.30	0.02	0.15		0.16
46X-6, 102-103	433.82	5.80	48.3	4.63	0.00	0.15		0.00
46X-6, 137-138	434.17	5.80	48.3	5.94	0.14	0.06		2.72
47X-1, 56-57	435.46	5.55	46.2	5.84	0.29	0.06		5.64
47X-2, 10-11	436.50	4.43	36.9	5.06	0.63	0.15		4.90
47X-3, 37-38	438.27	5.53	46.1	6.02	0.49	0.13		4.40
47X-3, 128-129	439.18	4.40	36.7	4.92	0.52	0.14		4.33
47X-6, 14-15	442.54	4.93	41.1	5.44	0.51	0.06		9.92
47X-7, 35-36	444.25	4.78	39.8	5.24	0.46	0.07		7.67
48X-1, 80-81	445.30	6.59	54.9	6.93	0.34	0.03	0.21	13.22
48X-2, 19-20	446.19	4.48	37.3	5.06	0.58	0.08	0.14	8.46
48X-2, 40-41	446.40	4.68	39.0	5.20	0.52	0.08	0.72	7.58
48X-3, 82-83	448.32	4.58	38.2	5.20	0.62	0.07	0.19	10.33
48X-4, 17-18	449.17	5.12	42.6	5.67	0.55	0.07	0.14	9.17
48X-6, 66-68	452.66	4.61	38.4	4.95	0.34	0.08	0.90	4.96
48X-6, 112-113	453.12	4.48	37.3	4.91	0.43	0.06	0.63	8.36
48X-6, 114-115	453.14	5.36	44.6	5.81	0.45	0.06	0.30	8.75
49X-1, 31-32	454.41	5.40	45.0	5.85	0.45	0.06	0.00	8.75
49X-2, 86-87	456.46	5.52	46.0	5.98	0.46	0.06	0.93	8.94
49X-3, 46-47	457.56	5.77	48.1	6.36	0.59	0.05	0.46	13.77
49X-3, 126-127	458.36	6.35	52.9	6.60	0.25	0.04	0.06	7.29
49X-5, 27-28	460.37	4.69	39.1	5.18	0.49	0.08	0.13	7.15
49X-6, 32-33	461.92	5.20	43.3	5.51	0.31	0.07	0.00	5.17
49X-CC, 26-27	463.79	4.15	34.6	4.52	0.37	0.07	0.00	6.17
50X-1, 18-19	463.88	5.07	42.2	5.51	0.44	0.07	0.08	7.33
50X-2, 100-101	466.20	6.73	56.1	6.97	0.24	0.03	0.11	9.33
50X-3, 22-23	466.92	4.38	36.5	4.74	0.36	0.07	0.14	6.00
50X-4, 112-113	469.32	4.70	39.2	4.99	0.29	0.06	0.06	5.64
50X-5, 103-104	470.73	5.58	46.5	5.72	0.14	0.06	0.00	2.72
50X-6, 117-118	472.37	6.59	54.9	6.79	0.20	0.03	0.10	7.78
50X-7, 3-4	472.73	6.41	53.4	6.53	0.12	0.03	0.43	4.67
51X-1, 8-9	473.38	4.90	40.8	5.07	0.17	0.06	0.00	3.31
51X-1, 55-56	473.85	5.65	47.1	5.73	0.08	0.04	0.00	2.33
51X-4, 82-83	478.62	4.82	40.2	5.08	0.26	0.06	0.05	5.06
51X-4, 109-110	478.89	6.39	53.2	6.41	0.02	0.05	0.09	0.47
52X-2, 106-108	485.46	5.59	46.6	5.82	0.23	0.05	0.07	5.37
52X-4, 44-46	487.84	5.39	44.9	5.68	0.29	0.06	0.00	5.64
52X-5, 79-80	489.69	7.48	62.3	7.79	0.31	0.01	0.25	36.17
52X-6, 3-4	490.43	5.99	49.9	6.34	0.35	0.04	0.09	10.21
52X-6, 105-106	491.45	7.43	61.9	7.64	0.21	0.02	0.00	12.25
53X-2, 112-113	495.12	6.26	52.1	6.49	0.23	0.04	0.00	6.71
53X-5, 66-67	499.16	4.37	36.4	4.93	0.56	0.07	0.11	9.33
53X-5, 122-123	499.72	4.11	34.2	4.55	0.44	0.07	0.00	7.33
53X-6, 61-62	500.61	6.86	57.1	7.01	0.15	0.04	0.10	4.37
53X-6, 136-137	501.36	4.91	40.9	5.32	0.41	0.07	0.04	6.83
54X-2, 18-19	503.78	4.63	38.6	5.24	0.61	0.07	0.10	10.17
54X-4, 18-19	506.78	5.17	43.1	5.66	0.49	0.07	0.17	8.17
54X-5, 25-26	508.35	6.98	58.1	7.16	0.18	0.03	0.00	7.00
54X-5, 127-128	509.37	4.46	37.2	4.94	0.48	0.07	0.06	8.02
54X-6, 3-4	509.63	4.44	37.0	4.82	0.38	0.07	0.57	6.33
55X-1, 11-12	511.91	6.33	52.7	6.73	0.40	0.05	1.08	9.33
55X-2, 53-54	513.83	4.78	39.8	5.19	0.41	0.07	0.56	6.83
55X-3, 50-51	515.30	4.66	38.8	5.09	0.43	0.06	0.07	8.36
55X-3, 77-78	515.57	5.93	49.4	6.70	0.77	0.06	0.70	14.97
55X-4, 78-79	515.08	6.77	56.4	7.14	0.37	0.04	0.18	10.79
55X-4, 92-93	517.22	6.16	51.3	6.56	0.40	0.06	0.19	7.78
55X-4, 139-140	517.69	4.41	36.7	4.83	0.42	0.07	0.05	7.00
55X-4, 145-146	517.75	4.27	35.6	4.66	0.39	0.07	0.00	6.50
55X-5, 43-44	518.23	3.85	32.1	4.37	0.52	0.07	0.09	8.67
55X-6, 97-98	520.27	4.36	36.3	4.92	0.56	0.08	0.90	8.17
55X-7, 38-39	521.18	4.36	36.3	4.78	0.42	0.07	0.73	7.00
56X-2, 103-104	523.93	6.99	58.2	7.20	0.21	0.04	0.16	6.13
56X-3, 43-44	524.83	4.44	37.0	4.77	0.33	0.11	0.62	3.50
56X-7, 26-27	530.66	7.00	58.3	7.28	0.28	0.04	0.17	8.17
57X-1, 23-24	531.23	4.29	35.7	4.67	0.38	0.08	1.04	5.54
57X-1, 114-115	532.14	6.85	57.1	7.18	0.33	0.05	0.40	7.70

Notes: Total organic carbon (TOC) concentrations are calculated from the difference between inorganic carbon and TC concentrations. C/N ratios are calculated from TOC and total nitrogen (TN) concentrations and are given as atom/atom ratios. TS = total sulfur concentrations. This table is also on the CD-ROM, back pocket, this volume.

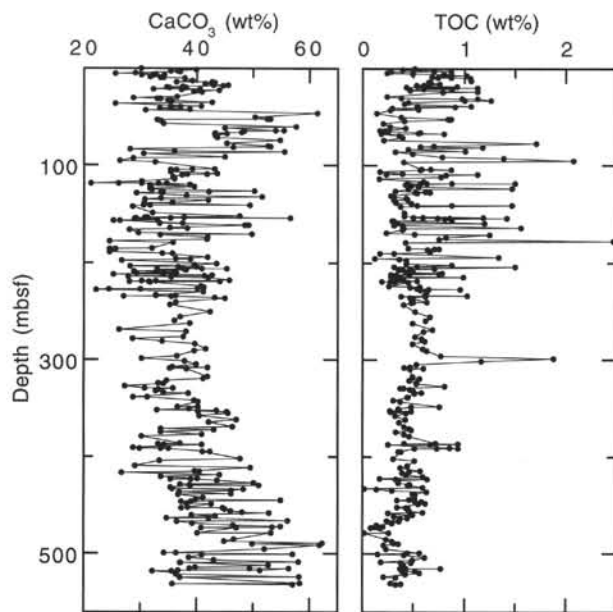


Figure 31. Organic carbon and CaCO_3 concentrations in sediment samples from Hole 977A.

Results

The main objective of logging in Hole 977A was to provide high-resolution images of the contact between the clays that constitute most of the sedimentologic units (and where the recovery was near 100%) and the low-recovery conglomeratic interval that occurs at the bottom of the hole. There is a smooth transition from the clay sediments to the conglomerates in terms of electrical response (534.0–536.0 mbsf). The change is more abrupt on other logs, placing the contact at 535.0 mbsf. The logs help provide information about the extremely low recovery interval below 531 mbsf.

In the logged section of Hole 977A, preliminary analysis of the logging data allows us to differentiate two main log units that correspond to the difference in the sediments recovered:

1. Log unit I (77.0–535.0 mbsf). This log unit shows a gradual downhole increase of formation resistivity from $0.7 \Omega\text{m}$ to $\sim 1 \Omega\text{m}$. Neutron-derived porosity remains in the 40%–45% range throughout this interval. The density is rather low in the upper part of the interval ($< 2 \text{ g/cm}^3$), and increases to 2 g/cm^3 between 440 and 470 mbsf, and to 2.2 g/cm^3 between 480 and 530 mbsf.
2. Log unit II (535.0–570.0 mbsf). This unit is characterized both by resistivity increase (1.5 to $2.0 \Omega\text{m}$), a decrease in the neutron porosity to 20%, and a density increase to 2.3 g/cm^3 .

Shipboard FMS images indicate that the data is of high quality. We observed an apparent depth shift between features observed with both the quad combo and FMS tools. This is caused by different far stretching of the logging cable caused by different weights of the tool strings. This was normally corrected post-cruise using the natural radioactivity log recorded with both tool strings. The subdued character of the natural radioactivity variations in the sediments of Hole 977A and the differing responses of the NGT tool between the two strings (mainly a result of being off-centered on the quad combo and centered on the FMS) complicated the correction. On the ship we compared both gamma-ray curves and caliper measurements and identified a depth shift of about 1.6 m between the two runs. This preliminary correction has been taken into account in our analysis and

presentation of the FMS data ($\text{depth}_{\text{FMS}} = \text{depth}_{\text{quad combo}} + 1.6 \text{ m}$). The two log units defined above using “standard” logs have also been recognized on FMS images, as they are electrically distinct one from another.

We present in Figure 44 a synoptic view of the downhole log data from the quad combo and FMS tools along with the MST measurements made in the shipboard lab for Core 977A-48X. This core was selected because it has a large peak in the susceptibility data and there was also an interval of slumped sediments in the lower part of the core. The downhole log data are recorded at different spacings (15 cm for quad combo data, 5 mm for FMS pad data) than the MST data (2 cm for susceptibility, 3 cm for GRAPE, 10 cm for natural gamma). The only standard downhole log data that correlate with the susceptibility peak is the drop in bulk density and increase in neutron porosity at 449.5 mbsf. The neutron porosity shows other peaks without density decreases of similar magnitude and is therefore suspect. There is nothing in the FMS data that obviously correlates with the susceptibility peak. Similarly, there is no clear indication in the unprocessed images of the slump found in the bottom of the core.

Figure 45 shows an expanded view of quad combo data and unprocessed FMS images from the transition zone. The low-recovery interval (531.0 mbsf to 598.0 mbsf, bottom hole) appears to begin at 532.0 mbsf, where a dark-colored 0.5-m-thick more conductive interval is identified both with “standard” logs and FMS. Note in the FMS data that there is internal layering within this interval. Below this layer is a 2.5-m-thick interval that has similar characteristics to the sediments above the dark-colored zone. The transition between clays and conglomerates at 535.0 mbsf is abrupt, and it is marked by a 1.0-m-thick layer, largely without internal zonation. This layer has a larger hole diameter, lower bulk density, higher porosity, a lower photoelectric effect value, and is darker (lower resistivity) in the FMS images. All of this is consistent with this layer having a distinctly higher water content than the surrounding layers. FMS images recorded in the 5-m interval below 535.0 mbsf are of excellent quality and provide information about the physical characteristics of the low-recovery conglomeratic interval.

IN SITU TEMPERATURE MEASUREMENTS

Downhole temperature measurements were made with the ADARA temperature tool four times in Hole 977A. The WSTP temperature tool was tried at two depths but failed due to battery problems.

The ADARA temperature data were reduced to in situ values (Table 18). The individual temperature measurement runs are shown in Figure 46. Temperature and thermal conductivity measurement data were combined to determine the heat flow (see “Physical Properties” section, this chapter). The thermal conductivity shows a gradual trend to higher conductivity over the depth interval where temperatures were measured. The temperature data were plotted vs. the integrated thermal resistivity in Figure 47. The uppermost three temperature points fall precisely on a line, while the deepest point falls well below that line. The fit from the three uppermost points gives an extrapolated surface temperature ($12.41 \pm 0.02^\circ\text{C}$) in close agreement with the observed seafloor temperature (12.4°C). The fit using all four points has a lower correlation and produces an extrapolated surface temperature ($12.86 \pm 0.44^\circ\text{C}$) well above that observed.

We interpret the heat flow from the uppermost three points, 101 mW/m^2 , to be the correct value for this site. The heat flow, if all four points were used, would be 89 mW/m^2 .

There are no other heat-flow values in the immediate vicinity of Site 977. Figure 48 shows other measurements in the region (Polyak et al., in press). The value for Site 977 is comparable to those in the middle of the basin to the north of the seamount just north of the site. The range of those values, 97 – 112 mW/m^2 , probably reflects the

Table 11. Results of Rock-Eval pyrolysis analyses of sapropels selected from Hole 977A.

Core, section, interval (cm)	Depth (mbsf)	TOC (%)	T _{max} (°C)	S ₁	S ₂	S ₃	PI	S ₂ /S ₃	PC	HI	OI
161-977A-											
2H-5, 7-8	10.0	0.71	416	0.14	1.69	2.68	0.08	0.62	0.15	236	377
4H-1, 37-38	23.4	0.81	422	0.20	1.48	2.86	0.12	0.51	0.14	182	353
4H-6, 10-11	30.6	0.87	416	0.22	2.15	2.86	0.09	0.75	0.19	247	328
5H-1, 42-43	32.9	1.00	415	0.16	2.05	2.79	0.07	0.73	0.18	205	279
9H-5, 78-79	77.3	1.23	408	0.31	2.98	2.41	0.09	1.23	0.27	242	195
11H-4, 82-83	94.8	1.71	416	0.26	5.06	2.54	0.05	1.99	0.44	295	148
14H-1, 7-8	118.1	1.21	420	0.17	3.34	2.43	0.05	1.37	0.29	276	200
16H-3, 105-106	141.0	0.99	417	0.23	2.39	2.24	0.09	1.06	0.21	241	226
17H-5, 148-149	154.0	1.30	417	0.94	2.73	2.21	0.26	1.23	0.30	210	170
18X-3, 18-19	159.2	1.22	418	0.74	2.08	2.08	0.26	1.00	0.23	170	170
18X-6, 18-19	163.7	1.56	418	0.13	3.56	2.42	0.04	1.47	0.30	228	155
19X-4, 91-92	171.0	1.22	420	0.08	1.83	2.36	0.04	0.77	0.15	150	193
20X-2, 97-98	177.7	0.29	408	0.04	0.36	1.96	0.10	0.18	0.03	124	675
20X-3, 116-117	179.4	0.35		0.04	0.42	1.79	0.09	0.23	0.03	120	511
23X-1, 63-64	204.6	1.31	418	0.25	3.62	2.29	0.06	1.58	0.32	276	174
26X-1, 90-91	233.8	0.35		0.04	0.56	1.53	0.07	0.36	0.05	160	437
32X-6, 104-105	299.0	0.40		0.05	0.58	1.57	0.08	0.36	0.05	145	392
33X-2, 20-21	301.8	0.31		0.04	0.42	1.39	0.09	0.30	0.03	135	448
35X-6, 10-11	327.0	0.38		0.08	0.80	1.51	0.09	0.52	0.07	210	397
37X-CC, 24-25	348.2	0.47	475	0.03	0.78	1.37	0.04	0.56	0.06	165	291
41X-7, 30-31	386.3	0.53	482	0.02	0.69	1.47	0.03	0.46	0.05	130	277
42X-4, 16-18	391.4	0.63	493	0.07	1.20	1.63	0.06	0.73	0.10	190	258
45X-6, 33-34	423.4	0.43	496	0.13	0.79	1.37	0.14	0.57	0.07	183	318
46X-5, 53-54	431.8	0.48	494	0.03	0.76	1.61	0.04	0.47	0.06	158	335

Notes: Total organic carbon (TOC) concentrations are derived from the Rock-Eval parameters and therefore differ somewhat from the TOC values of the same samples in Table 10. T_{max} values could not be measured accurately for samples with low (<0.5%) TOC contents. Units of the various Rock-Eval parameters are given in the "Explanatory Notes" chapter, this volume.

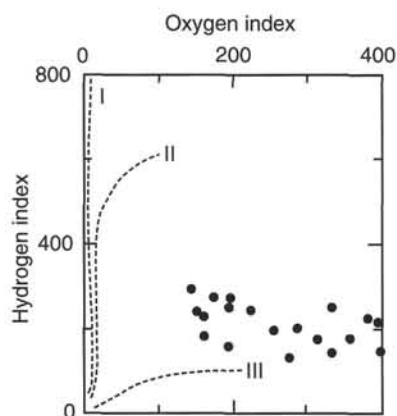


Figure 32. Rock-Eval van Krevelen-type diagram of Pleistocene sapropels from Hole 977A. Organic matter appears to be a mixture of Type II algal material that has been variably oxidized and Type III continental or detrital organic matter. Hydrogen index = mg hydrocarbons/g organic carbon; oxygen index = mg CO₂/g organic carbon.

variation in sediment thickness in that basin. If basement temperatures were near constant in the basin, perhaps as a result of hydrothermal circulation within the basement, the heat flow would be lowest in those areas with thickest sediment. High sedimentation rates will also serve to depress the surface heat flow, but the rates are unlikely to vary enough in the short distances involved to account for the observed variation.

REFERENCES

- Abrantes, F., 1988. Diatom productivity peak and increased circulation during the latest Quaternary: Alboran Basin (western Mediterranean). *Mar. Micropaleontol.*, 13:79-96.
- Alonso, B., and Maldonado, A., 1992. Plio-Quaternary margin growth patterns in a complex tectonic setting: northeastern Alboran Sea. *Geo-Mar. Lett.*, 12:137-143.

- Bellon, H., Bordet, P., and Montenat, C., 1983. Le magmatisme néogène des Cordillères bétiques (Espagne): chronologie et principaux caractères géochimiques. *Bull. Soc. Geol. Fr.*, Ser. 7, 25:205-218.
- Canfield, D.E., and Berner, R.A., 1987. Dissolution and pyritization of magnetite in anoxic marine sediments. *Geochim. Cosmochim. Acta*, 51:645-659.
- Claypool, G.E., and Kvenvolden, K.A., 1983. Methane and other hydrocarbon gases in marine sediment. *Annu. Rev. Earth Planet. Sci.*, 11:299-327.
- Cloetingh, S., van der Beek, P.A., van Rees, D., Roep, Th.B., Biermann, C., and Stephenson, R.A., 1992. Flexural interaction and the dynamics of Neogene extensional basin formation in the Alboran-Betic region. *Geo-Mar. Lett.*, 12:66-67.
- Comas, M.C., García-Dueñas, V., and Jurado, M.J., 1992. Neogene tectonic evolution of the Alboran Basin from MCS data. *Geo-Mar. Lett.*, 12:157-164.
- Comas, M.C., García-Dueñas, V., Soto, J.I., and Campos, J., 1993. An extensional basin developed on a collisional orogen: the Alboran Sea. In Seranne, M., and Malavielle, J. (Eds.), *Late Orogenic Extension in Mountain Belts*. Doc. B.R.G.M. Fr., 219:44-46.
- Comas, M.C., and Maldonado, A., 1988. Late Cenozoic sedimentary facies and processes in the Iberian Abyssal Plain, Site 637, ODP Leg 103. In Boillot, G., Winterer, E.L., et al., *Proc. ODP, Sci. Results*, 103: College Station, TX (Ocean Drilling Program), 635-655.
- Comas, M.C., Bourgeois, J., Boulègue, J., Fernandez-Soler, J.M., de la Linde, J., and Soto, J.I., in press. Preliminary results of the Cyanalboran cruise: dives of the submersible CYANA in the Alboran Sea. *Terra Nova*.
- Deer, W.A., Howie, R.A., and Zussman, J., 1966. *An Introduction to the Rock-Forming Minerals*: London (Longman Group).
- de Larouzière, F.D., Bolze, J., Bordet, P., Hernandez, J., Montenat, C., and Ott d'Estevou, P., 1988. The Betic segment of the lithospheric trans-Alboran shear zone during the Late Miocene. *Tectonophysics*, 152:41-52.
- Docherty, J.I.C., and Banda, E., 1992. A note on the subsidence history of the northern margin of the Alboran Sea. *Geo-Mar. Lett.*, 12:82-87.
- Emerson, S., and Hedges, J.I., 1988. Processes controlling the organic carbon content of open ocean sediments. *Paleoceanography*, 3:621-634.
- Espitalié, J., Laporte, J.L., Leplat, P., Madec, M., Marquis, F., Paulet, J., and Boutefeu, A., 1977. Méthode rapide de caractérisation des roches mères, de leur potentiel pétrolier et de leur degré d'évolution. *Rev. Inst. Fr. Pet.*, 32:23-42.
- Hernandez-Pacheco, A., and Ibarrola, E., 1970. Nuevos datos sobre la petrología y geoquímica de las rocas volcánicas de la isla de Alborán (Mediterráneo occidental, Almería). *Estud. Geol. (Madrid)*, 26:93-103.

- Karlin, R., Lyle, M., and Heath, G.R., 1987. Authigenic magnetite formation in suboxic marine sediments. *Nature*, 326:490–493.
- Mauffret, A., El-Robrini, M., and Genesseeux, M., 1987. Indice de la compression récente en mer Méditerranée: un bassin losangique sur la marge nor-algérienne. *Bull. Soc. Geol. Fr.*, 8:1195–1206.
- Mauffret, A., Maldonado, A., and Campillo, A.C., 1992. Tectonic framework of the Eastern Alboran and Western Argelian Basins, Western Mediterranean. *Geo-Mar. Lett.*, 12:104–110.
- McIver, R.D., 1975. Hydrocarbon occurrences from JOIDES Deep Sea Drilling Project. *Proc. Ninth Petrol. Congr.*, 269–280.
- Meyers, P.A., 1994. Preservation of elemental and isotopic source identification of sedimentary organic matter. *Chem. Geol.*, 144:289–302.
- Meyers, P.A., and Brassell, S.C., 1985. Biogenic gases in sediments deposited since Miocene times on the Walvis Ridge, South Atlantic Ocean. In Caldwell, D.E., Brierley, J.A., and Brierley, C.L. (Eds.), *Planetary Ecology*: New York (Van Nostrand Reinhold), 69–80.
- Meyers, P.A., and Shaw, T.J., in press. Organic matter accumulation, sulfate reduction, and methanogenesis in Pliocene–Pleistocene turbidites on the Iberia Abyssal Plain. In Whitmarsh, R.B., Sawyer, D.S., Klaus, A., and Masson, D.G. (Eds.), *Proc. ODP, Sci. Results*, 149: College Station, TX (Ocean Drilling Program).
- Meyers, P.A., and Snowdon, L.R., 1993. Sources and migration of methane-rich gas in sedimentary rocks on the Exmouth Plateau: northwest Australian continental margin. In Oremland, R.S. (Ed.), *Biogeochemistry of Global Change*: New York (Chapman and Hall), 434–446.
- Minas, H.J., Coste, B., Le Corre, P., Minas, M., and Raimbault, P., 1991. Biological and geochemical signatures associated with the water circulation through the Strait of Gibraltar and the Western Alboran Sea. *J. Geophys. Res.*, 96:8755–8771.
- Müller, P.J., 1977. C/N ratios in Pacific deep sea sediments: effect of inorganic ammonium and organic nitrogen compounds sorbed by clays. *Geochim. Cosmochim. Acta*, 41:765–776.
- Otofujii, Y., and Sasajima, S., 1981. A magnetization process of sediment: laboratory experiment on post-depositional remanent magnetization. *Geophys. J. R. Astron. Soc.*, 66:241–260.
- Pickering, K.T., Hiscott, R., and Hein, F.J., 1989. *Deep-Marine Environments: Clastic Sedimentation and Tectonics*: London (Unwin Hyman).
- Platt, J.P., and Vissers, R.L.M., 1989. Extensional collapse of thickened continental lithosphere: a working hypothesis for the Alboran Sea and Gibraltar Arc. *Geology*, 17:540–543.
- Polyak, B.G., Fernandez, M., Khutoskoy, M.D., Soto, J.I., Basov, I.A., Comas, M.C., Khain, V.Ye., Alonso, B., Agapova, G.V., Mazurova, I.S., Negrodo, A., Tochitsky, V.O., de la Linde, J., Bogdanov, N.A., and Banda, E., in press. Heat flow in the Alboran Sea (the Western Mediterranean). *Tectonophysics*.
- Rochette, P., 1987. Magnetic susceptibility of the rock matrix related to magnetic fabric studies. *J. Struct. Geol.*, 9:1015–1020.
- Rochette, P., Jackson, M., and Aubourg, C., 1992. Rock magnetism and the interpretation of anisotropy of magnetic susceptibility. *Rev. Geophys.*, 30:209–226.
- Rullkötter, J., Cornford, C., and Welte, D.H., 1982. Geochemistry and petrography of organic matter in Northwest African continental margin sediments: quantity, provenance, depositional environment and temperature history. In von Rad, U., Hinz, K., Sarnthein, M., and Seibold, E. (Eds.), *Geology of the Northwest African Continental Margin*: Berlin (Springer-Verlag), 686–703.
- Scholle, P.A., and Ekdale, A.A., 1983. Pelagic environments. In Scholle, P.A., Bebout, D.G., and Moore, C.H. (Eds.), *Carbonate Depositional Environments*. AAPG Mem., 33:620–691.
- Shipboard Scientific Party, 1990. Site 767. In Rangin, C., Silver, E.A., von Breyman, M.T., et al., *Proc. ODP, Init. Repts.*, 124: College Station, TX (Ocean Drilling Program), 121–193.
- Stanley, D.J., 1983. Parallel-laminated deep-sea muds and coupled gravity-flow hemipelagic settling in the Mediterranean. *Smithson. Contrib. Marine Sci.*, 19.
- Stow, D.A.V., and Piper, D.J.W., 1984. *Fine-Grained Sediments: Deep-Water Processes and Facies*. Geol. Soc. Spec. Publ. London, 15.
- Tintoré, J., Viúdez, A., Gomis, D., Alonso, S., and Werner, F.E., 1995. Mesoscale variability and Q vector vertical motion in the Alboran Sea. In La Violette, P.E. (Ed.), *Seasonal and Interannual Variability of the Western Mediterranean Sea*: Washington (Am. Geophys. Union), Coastal and Estuarine Studies, 46:47–71.
- Vergnaud-Grazzini, C., and Pierre, C., 1991. High fertility in the Alboran Sea since the Last Glacial Maximum. *Paleoceanography*, 6:519–536.
- Watts, A.B., Platt, J.P., and Bulh, P., 1993. Tectonic evolution of the Alboran Sea Basin. *Basin Res.*, 5:153–177.
- Woodside, J.M., and Maldonado, A., 1992. Styles of compressional neotectonics in the Eastern Alboran Sea. *Geo-Mar. Lett.*, 12:111–116.
- Wright, R., 1978. Neogene paleobathymetry of the Mediterranean based on benthic foraminifers from DSDP Leg 42. In Hsü, K.J., Montadert, L., et al., *Init. Repts. DSDP*, 42 (Pt. 1): Washington (U.S. Govt. Printing Office), 837–846.

Ms 1611R-107

NOTE: For all sites drilled, core-description forms (“barrel sheets”) and core photographs can be found in Section 3, beginning on page 429. Smear-slide data can be found in Section 4, beginning on page 949. Thin-section data can be found in Section 5, beginning on page 991. See Table of Contents for material contained on CD-ROM.

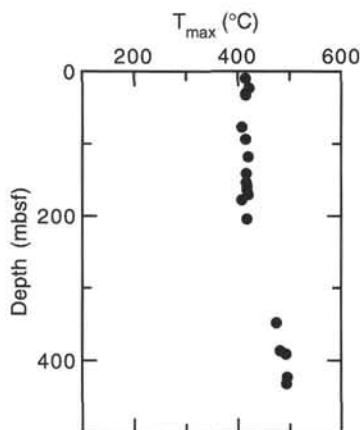


Figure 33. Increase of Rock-Eval T_{max} values with depth in sediments of Hole 977A. Sediments above 200 mbsf are thermally immature with respect to petroleum generation, whereas those below 250 mbsf are overmature.

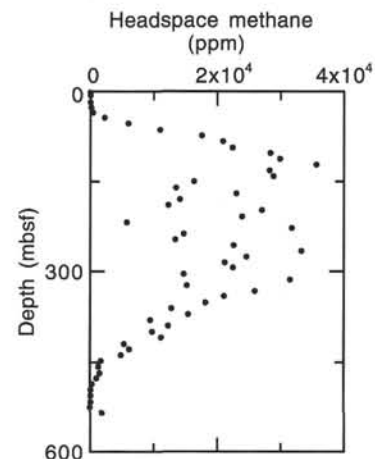


Figure 34. Headspace methane concentrations in sediments from Hole 977A. The decrease in concentrations below 300 mbsf is probably a result of migration of thermogenic methane out of the sediments during the Pliocene.

Table 12. Results of headspace gas analyses of sediments from Hole 977A.

Core, section, interval (cm)	Depth (mbsf)	C ₁	C ₂₌	C ₂	C ₃₌	C ₃	IC ₄	IC ₅	IC ₆	NC ₆	C ₁ /C ₂
161-977A-											
1H-2, 0-5	2	3									
2H-3, 0-5	7	3									
3H-4, 0-5	18	7									
4H-4, 0-5	27	56									
5H-4, 0-5	36	339									
6H-4, 0-5	44	2171									
7H-4, 0-5	54	5899									
8H-4, 0-5	64	10992									
9H-4, 0-5	74	17543									
10H-4, 0-5	84	20956									
11H-4, 0-5	94	22401									
12H-4, 0-5	103	28414									11201
13H-4, 0-5	112	29912									14207
14H-4, 0-5	122	35695									9971
15H-4, 0-5	131	28307									11898
16H-4, 0-5	141	28865									9436
17H-4, 0-5	150	16411									9622
18X-4, 0-5	160	13582									8206
19X-4, 0-5	170	23020									6791
20X-4, 0-5	179	14125									7673
21X-4, 0-5	189	12290									7063
22X-4, 0-5	198	27084									6145
23X-4, 0-5	208	23936									5417
24X-4, 0-5	218	5759									5984
25X-4, 0-5	227	31857	8	3	30	5					2880
26X-4, 0-5	237	14755		4		13					10619
27X-4, 0-5	247	13430		3		15					3689
28X-4, 0-5	256	22627	13	39	18	73					4477
29X-4, 0-5	266	33330		8		40	9	12	7	8	580
30X-4, 0-5	275	24633		5		29					4166
31X-4, 0-5	285	21169		5		28	5	6			4927
32X-4, 0-5	294	22546		5		30	5	6			4234
33X-4, 0-5	304	14735		4		24	5	7			4509
34X-4, 0-5	314	31564		8		58	9	13			3684
35X-4, 0-5	323	15229		4		27	5	6			3946
36X-4, 0-5	333	25980		7		56	9	13			3807
37X-4, 0-5	342	21144		6		48	9	12			3711
38X-4, 0-5	352	18139		5		40	8	9			3524
39X-4, 0-5	362	12853		4		43	11	14			3628
40X-4, 0-5	371	15438		5		45	9	10			3213
41X-4, 0-5	381	9449		3		32	8	9			3088
42X-4, 0-5	391	12314		5		70	16	20			3150
43X-4, 0-5	400	9779		3		33	5	5			2463
44X-4, 0-5	410	11226		4		38	7	7			3260
45X-4, 0-5	420	5340		2		26	5	6			2807
46X-4, 0-5	429	6167		2		14					2670
47X-4, 0-5	439	4868				10					3084
48X-4, 0-5	448	1763				5					
49X-4, 0-5	458	1275				2					
50X-4, 0-5	468	1485				3					
51X-3, 0-5	477	972	2	3							324
52X-1, 0-5	487	256									
53X-4, 0-5	496	107									
54X-4, 0-5	506	32									
55X-4, 0-5	516	44									
56X-4, 0-5	525	24									
57X-4, 0-5	535	1803				5					

Notes: Dominance of methane indicates that the most of the gases originate from in situ fermentation of organic matter. The presence of significant amounts of thermogenic C₃, C₄, and C₅ gases below 200 mbsf suggests that heat flows were once higher at Site 977. C₂₌ = ethene, C₃₌ = propene.

Table 13. Interstitial water data from Hole 977A.

Core, section, interval (cm)	Depth (mbsf)	pH	Alkalinity (mM)	Salinity (‰)	Cl (mM)	Ca (mM)	Mg (mM)	Mn (μM)	Sr (μM)	SO ₄ (mM)	NH ₄ (mM)	H ₄ SiO ₄ (μM)	Li (μM)	Na (mM)	K (mM)	PO ₄ (μM)
161-977A-																
1H-1, 145-150	1.45	7.4	5.62	38	619	11.09	59.66	23.7	102	28.86	0.25	470	32	553.92	12.41	17.87
1H-2, 145-150	2.95	7.5	7.10	39	625	10.16	58.27	18.6	105	28.57	0.55	583	34	521.38	12.30	24.26
2H-2, 145-150	6.88	7.2	12.49	37	625	7.42	56.32	15.2	95	20.09	1.13	977	35	538.23	11.96	56.21
2H-4, 145-150	9.88	7.5	14.44	38	619	5.91	54.92	10.6	91	16.82	1.40	977	36	516.59	12.19	55.44
3H-3, 145-150	17.95	7.5	15.09	37	607	4.38	50.39	8.9	80	10.66	1.41	441	42	505.30	11.26	18.89
4H-3, 145-150	27.45	7.6	13.50	36	612	4.10	47.59	7.0	90	6.48	1.44	433	49	523.11	10.93	10.20
5H-3, 145-150	36.95	7.6	13.17	34	606	4.44	44.14	7.5	106	2.68	1.51	417	55	530.37	10.23	14.03
6H-3, 145-150	46.45	7.6	n.d.	34	605	4.06	40.66	6.2	141	0.33	1.60	371	61	526.92	9.85	9.43
9H-3, 145-150	74.95	7.5	10.37	34	595	7.68	35.88	5.2	207	0.00	2.17	711	82	521.78	8.59	7.39
12H-3, 145-150	103.45	7.1	10.91	34	608	7.59	35.19	7.0	233	0.00	2.74	933	110	479.19	7.96	7.13
15H-3, 145-150	131.95	7.3	8.65	34	612	9.00	34.15	4.6	241	0.00	2.80	461	128	489.30	7.63	8.66
18X-3, 145-150	160.45	7.1	7.12	34	612	9.98	34.15	8.1	250	0.27	2.86	435	130	487.24	6.50	5.34
21X-3, 145-150	189.35	7.2	5.57	36	617	10.22	34.05	5.8	261	0.00	3.07	366	120	491.60	5.82	<2.5
24X-3, 140-150	218.00	7.4	4.72	36	624	9.59	33.99	6.0	290	0.00	3.94	313	121	497.10	5.51	4.99
27X-3, 140-150	247.00	7.4	4.07	34.5	626	10.53	33.76	5.2	320	0.20	3.41	280	122	505.03	6.03	3.47
30X-3, 140-150	275.80	7.4	3.67	35	638	12.78	33.96	5.7	379	0.00	3.24	337	133	509.77	5.30	2.46
33X-3, 140-150	304.50	7.2	4.54	36	631	14.98	34.32	1.0	480	0.00	2.37	329	142	531.71	5.35	<2.5
36X-3, 140-150	333.30	7.3	2.84	36	656	17.24	35.58	1.1	596	0.00	1.93	309	156	547.25	4.08	<2.5
39X-3, 140-150	362.30	7.2	2.46	36	678	22.02	35.01	1.1	725	0.00	2.01	289	173	552.57	5.42	<2.5
42X-3, 140-150	391.10	7.0	1.93	40	676	27.64	35.52	0.9	899	0.00	1.94	300	177	545.41	3.35	<2.5
45X-3, 140-150	420.00	7.3	1.55	40	700	33.66	35.72	1.0	1042	0.00	2.01	220	184	570.17	4.00	<2.5
48X-3, 140-150	448.90	7.0	1.33	41	728	41.66	37.15	1.2	1229	0.00	1.92	282	191	566.50	4.22	<2.5
51X-3, 140-150	477.70	7.3	1.44	43.5	749	54.47	37.96	1.5	1437	0.38	1.29	191	202	566.30	4.22	<2.5
54X-3, 140-150	506.50	n.d.	n.d.	46	778	76.40	35.40	1.5	1350	6.47	1.10	121	190	578.80	4.08	<2.5

Note: n.d. = not determined. This table is also on the CD-ROM, back pocket, this volume.

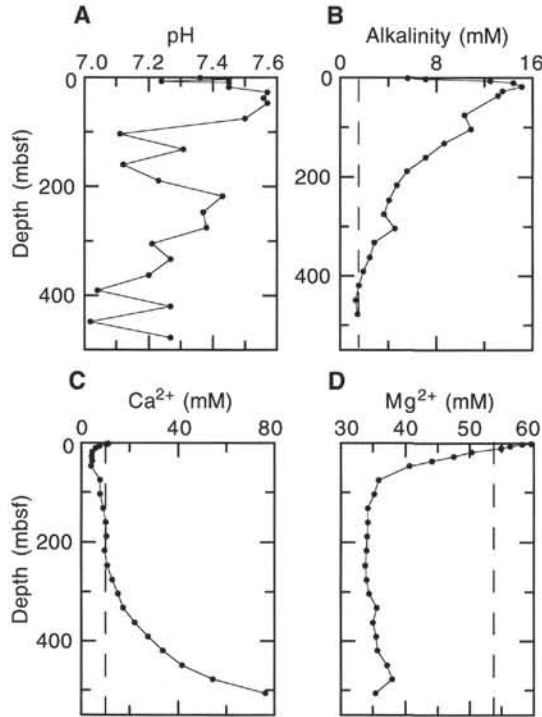


Figure 35. Concentration profiles of (A) pH, (B) alkalinity, (C) calcium, and (D) magnesium in Hole 977A. The dashed lines indicate standard seawater (International Association for the Physical Sciences of the Ocean [IAPSO]) composition.

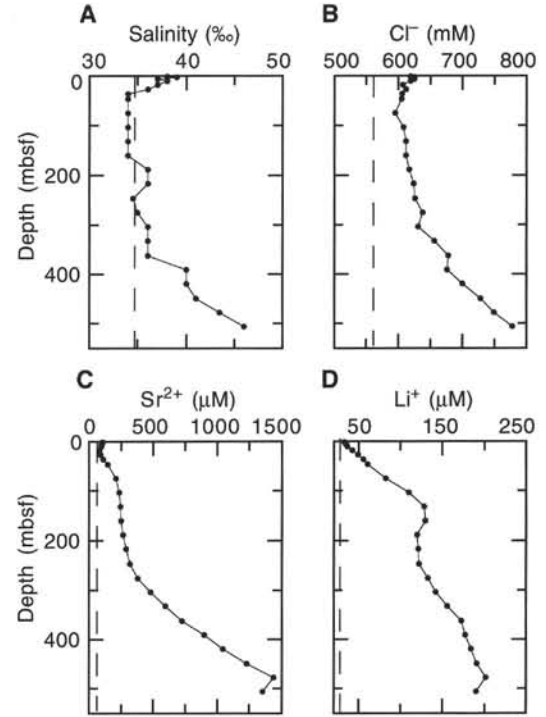


Figure 36. Concentration profiles of (A) salinity, (B) chloride, (C) strontium, and (D) lithium in Hole 977A. The dashed lines indicate standard seawater (IAPSO) composition.

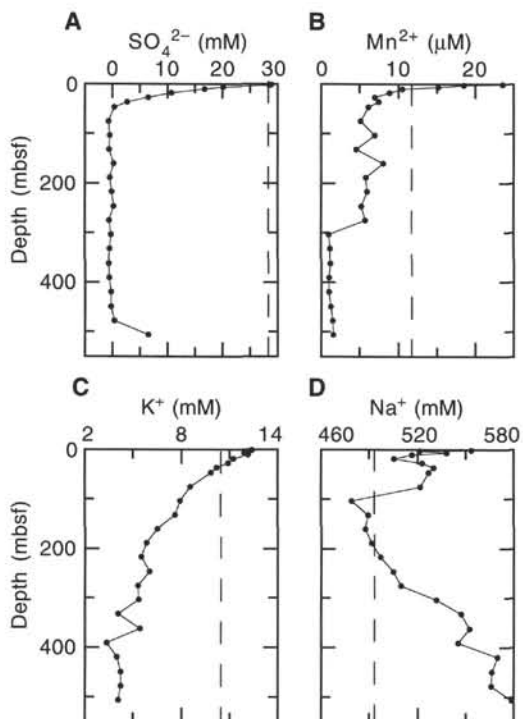


Figure 37. Concentration profiles of (A) sulfate, (B) manganese, (C) potassium, and (D) sodium in Hole 977A. The dashed lines indicate standard seawater (IAPSO) composition.

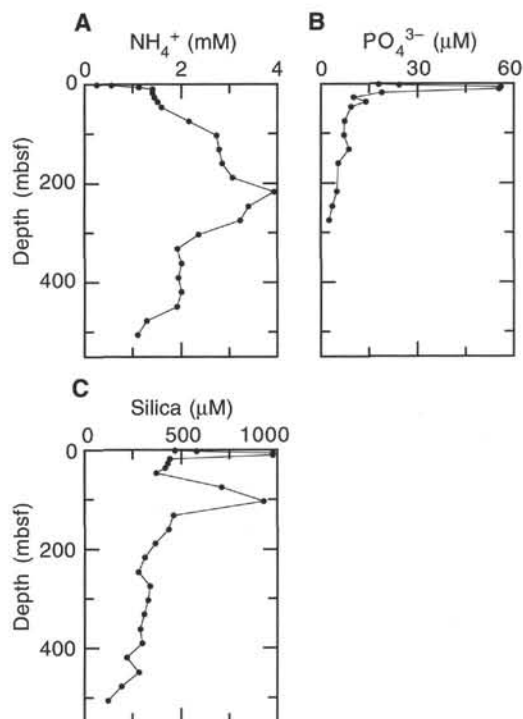


Figure 38. Concentration profiles of (A) ammonium, (B) phosphate, and (C) silica in Hole 977A.

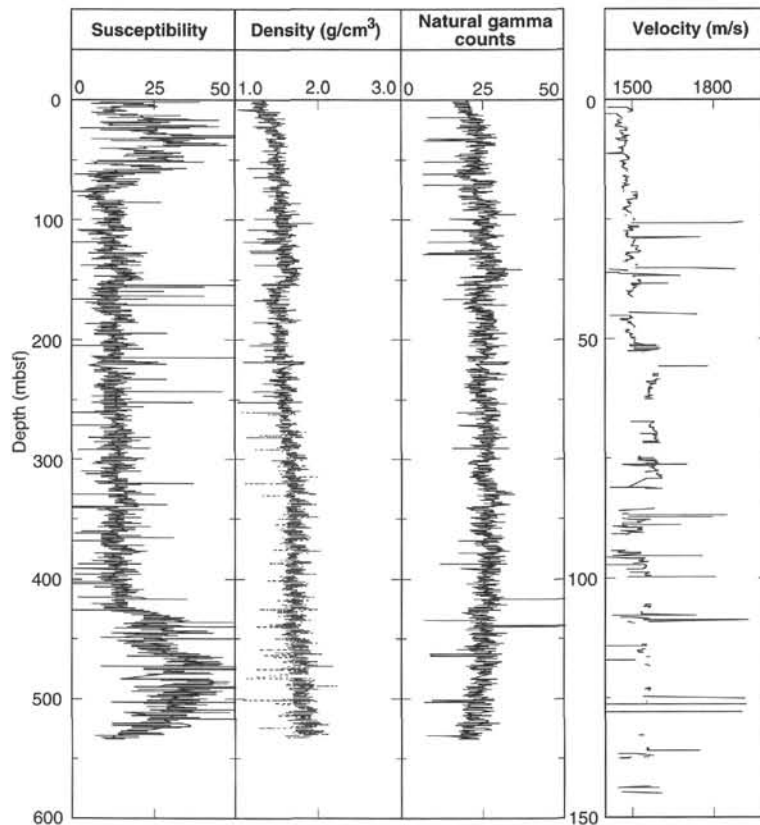


Figure 39. MST data (susceptibility, density, natural gamma, and velocity) for Hole 977A. Note the different depth scale for the velocity data.

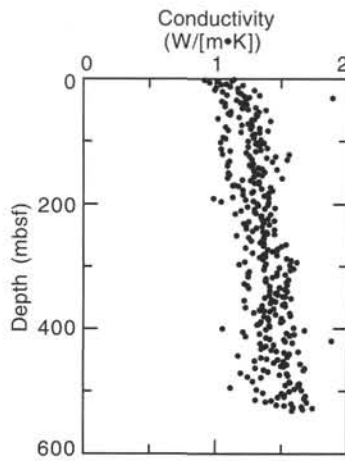


Figure 40. Thermal conductivity data for Hole 977A.

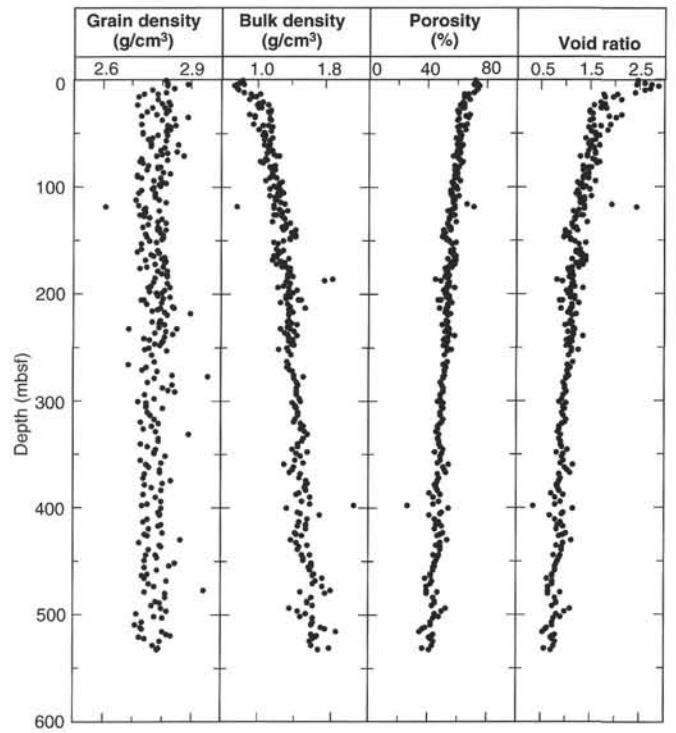


Figure 41. Index property data for Hole 977A.

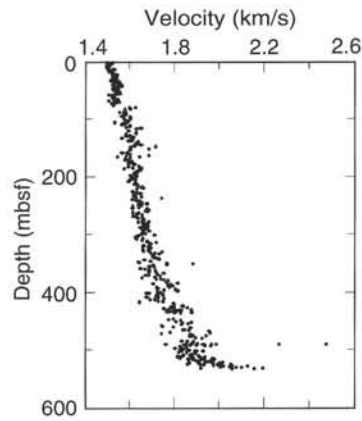


Figure 42. Seismic velocity data for Hole 977A.

Table 17. Logged depth intervals in Hole 977A for quad combo and FMS.

String	Run	Depth		Tools
		(mbsf)	(mbrf)	
Quad combo	Up 1	570.0–77.0	2565.0–2073.0	NGT/SDT/CNT-G/HLDT/DIT-E/TLT
	Up 2*	190.0–61.0	2185.0–2056.0	NGT/SDT/CNT-G/HLDT/DIT-E/TLT
FMS	Up 1	561.0–420.0	2556.0–2415.0	NGT/FMS/GPIT
	Up 2*	560.0–522.0	2555.0–2517.0	NGT/FMS/GPIT

Notes: * = repeat section; mbsf = meters below seafloor; mbrf = meters below rig floor.

Table 18. Depths and equilibrium temperatures for the ADARA and WSTP temperature tool runs at Hole 977A.

Depth (mbsf)	Temperature (°C)
23.0	14.564
51.5	16.954
80.0	19.300
108.5	20.683

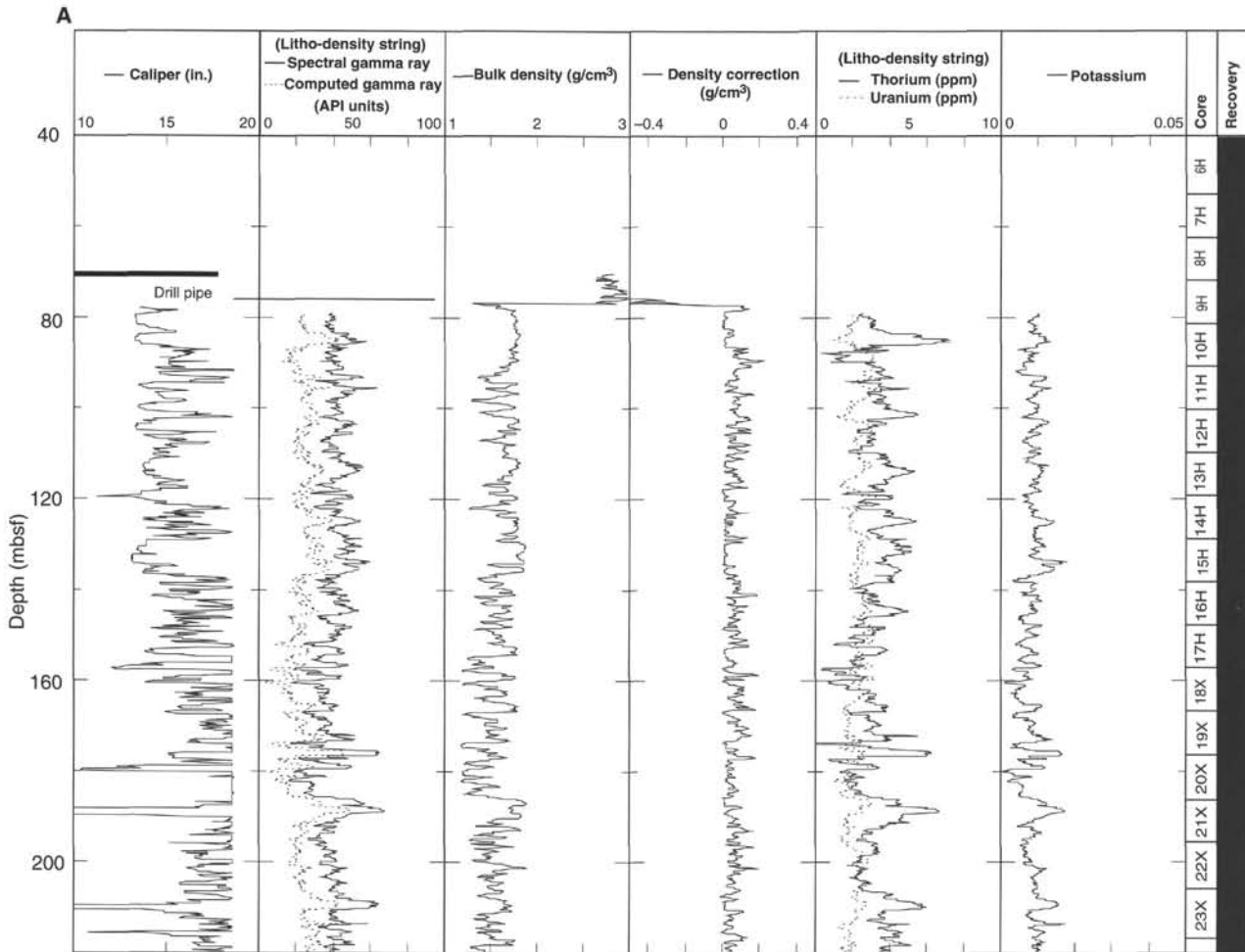


Figure 43. Quad combo (A–C) and FMS tool (D–F) results for Hole 977A. FMS data has been shifted 1.6 m using caliper data as a reference (see text).

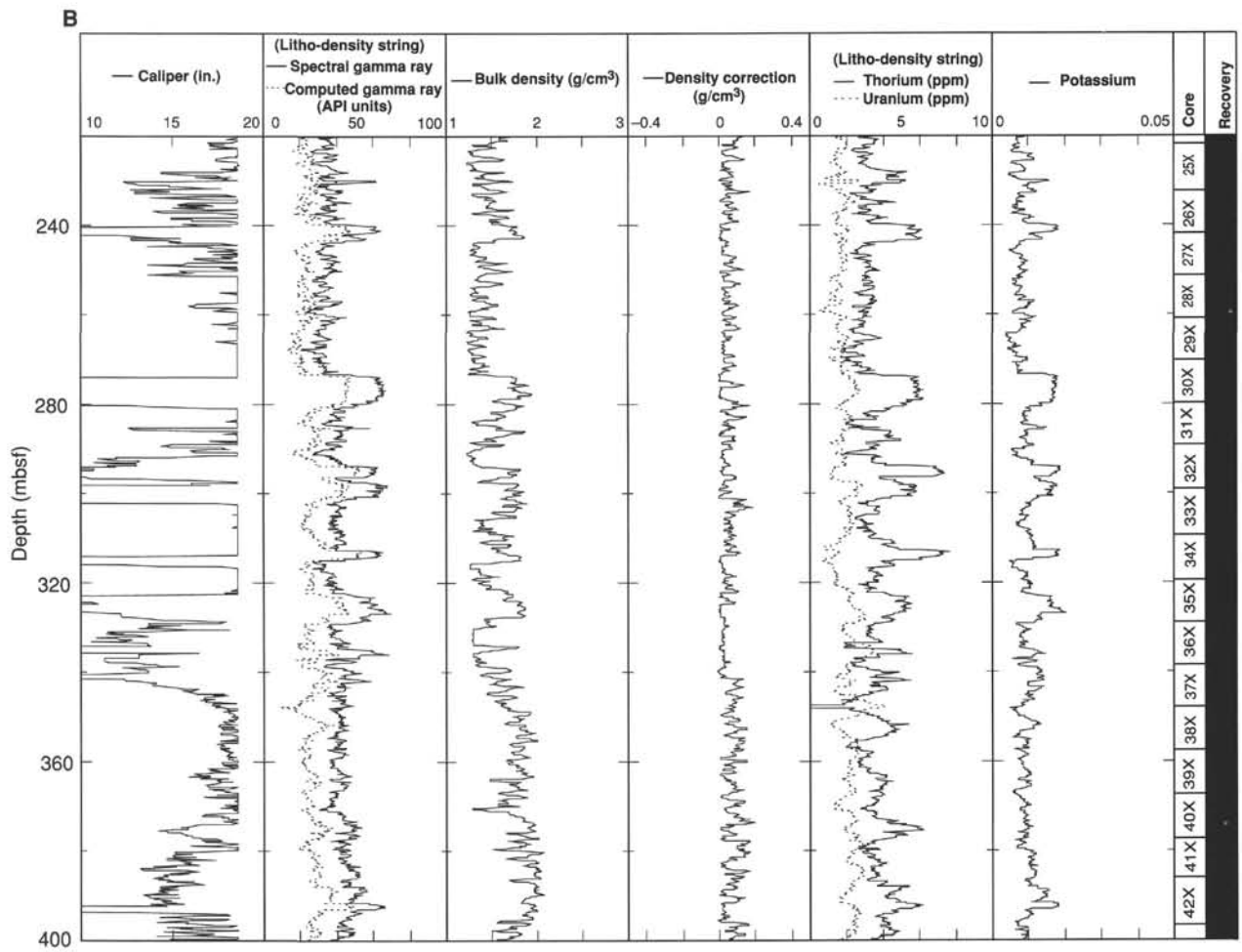


Figure 43 (continued).

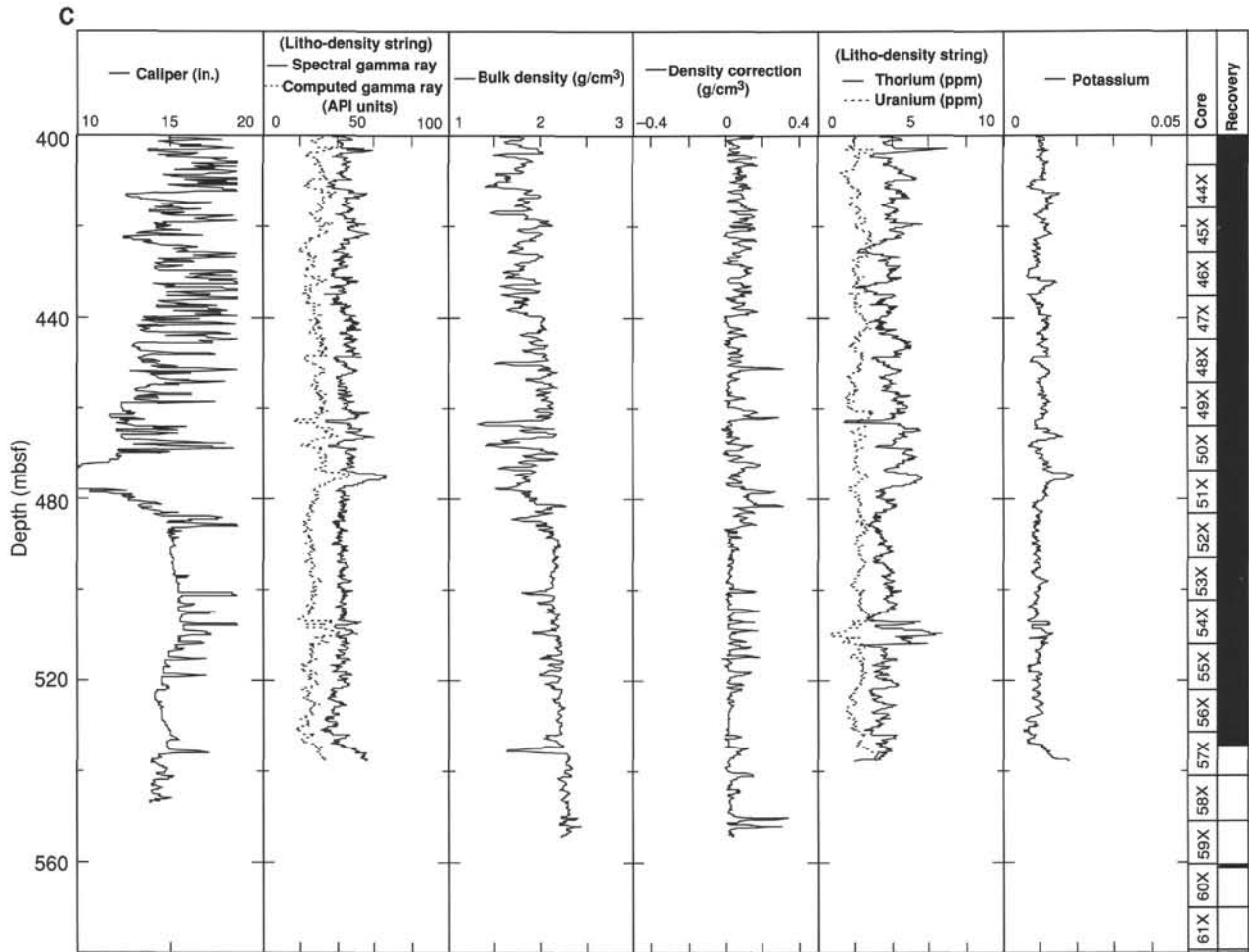


Figure 43 (continued).

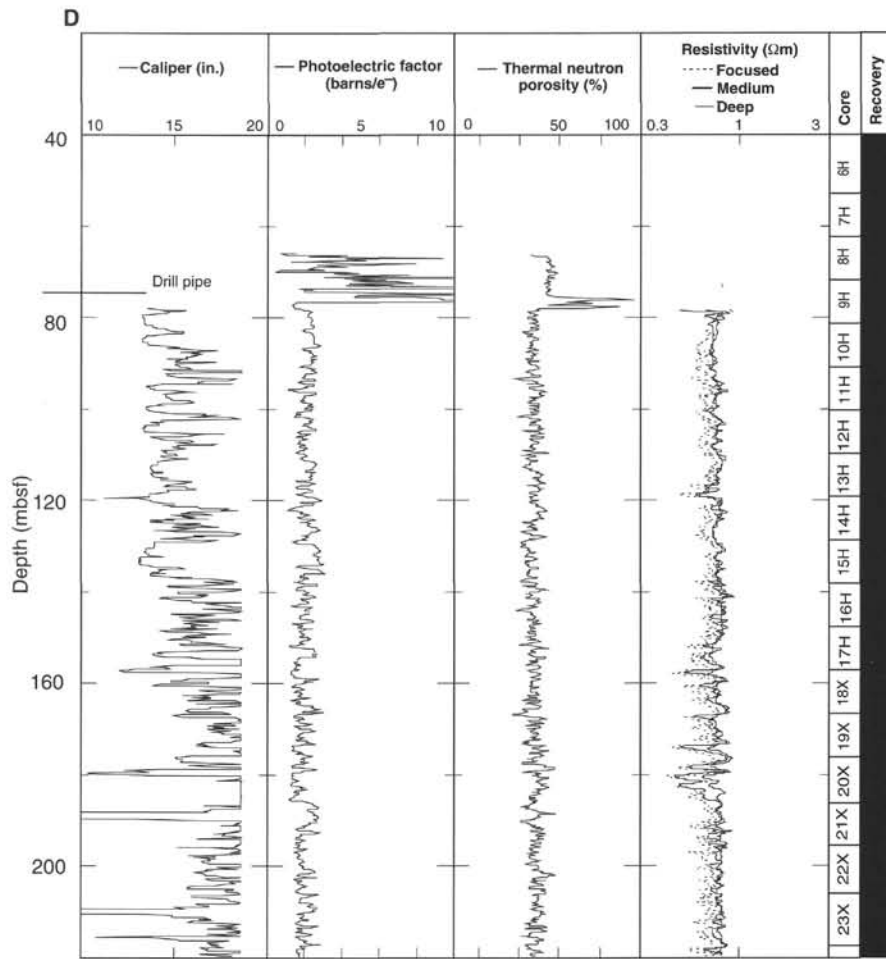


Figure 43 (continued).

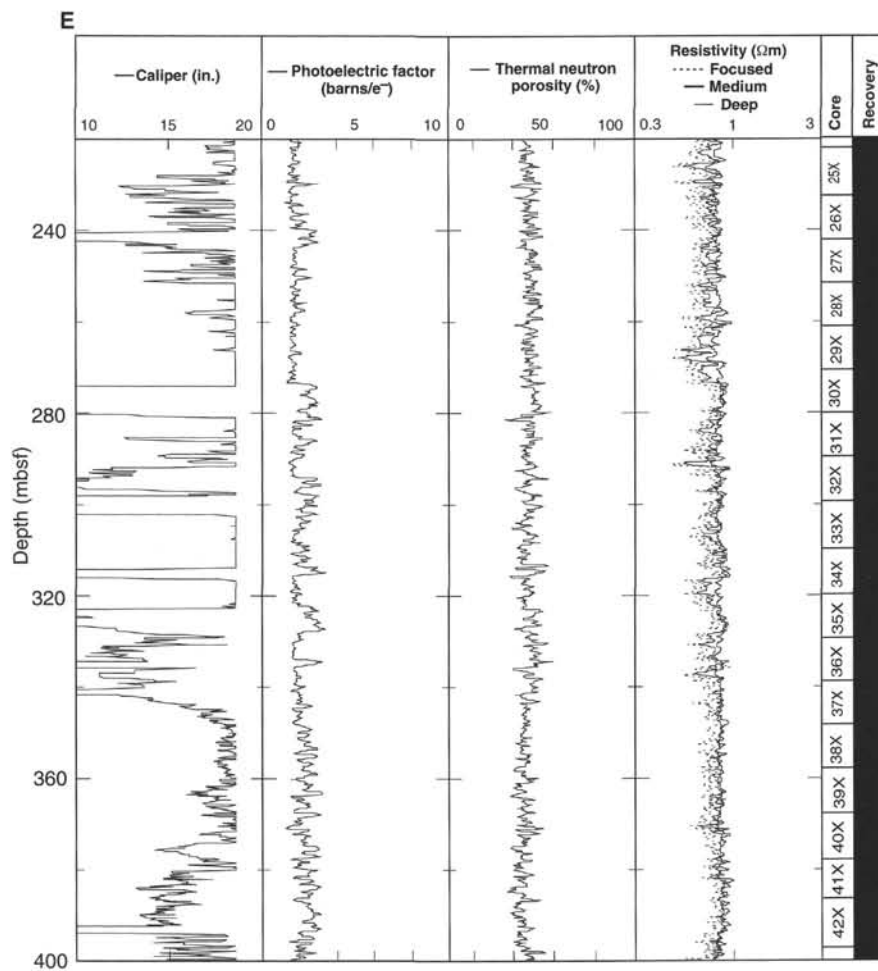


Figure 43 (continued).

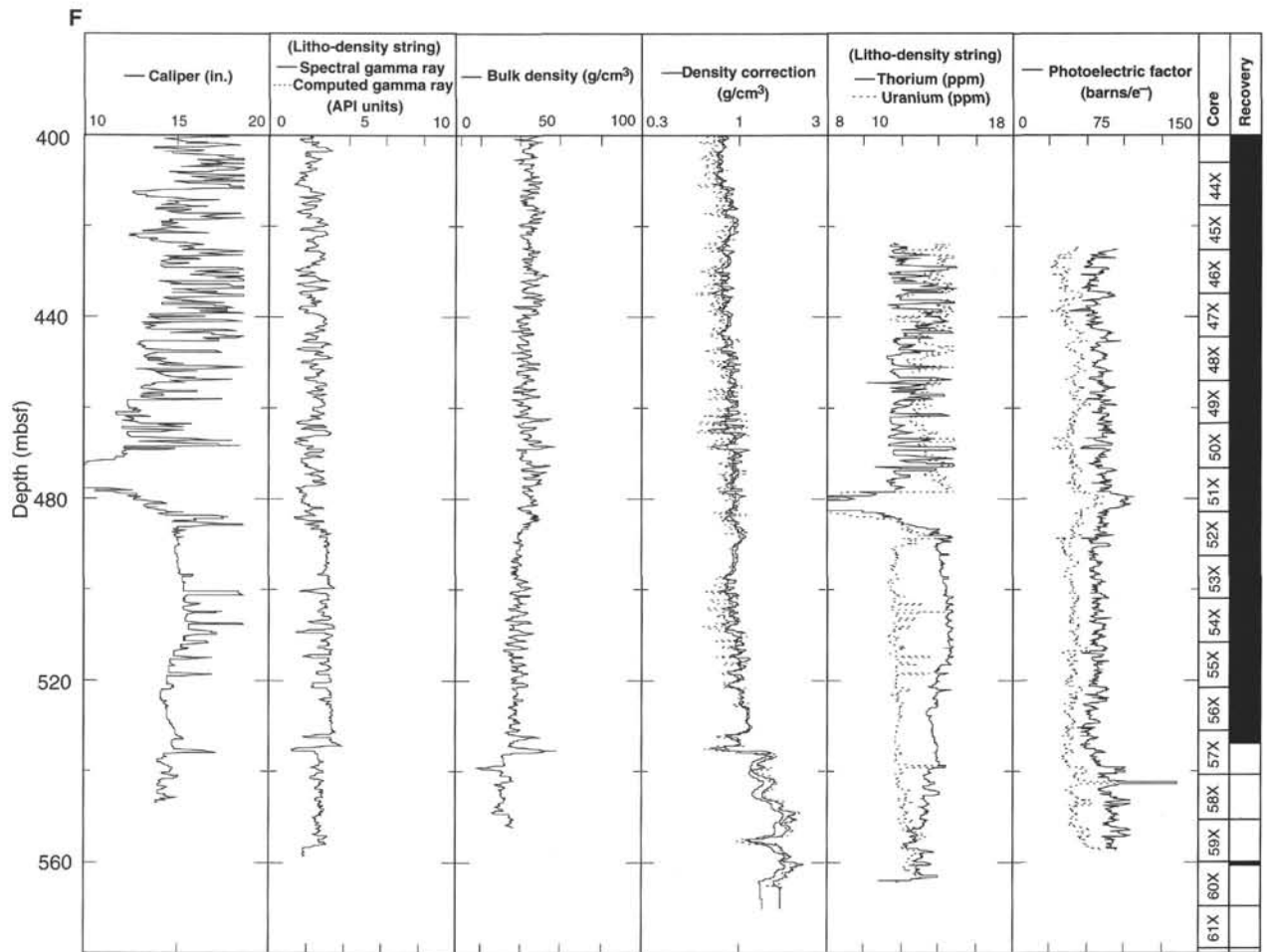


Figure 43 (continued).

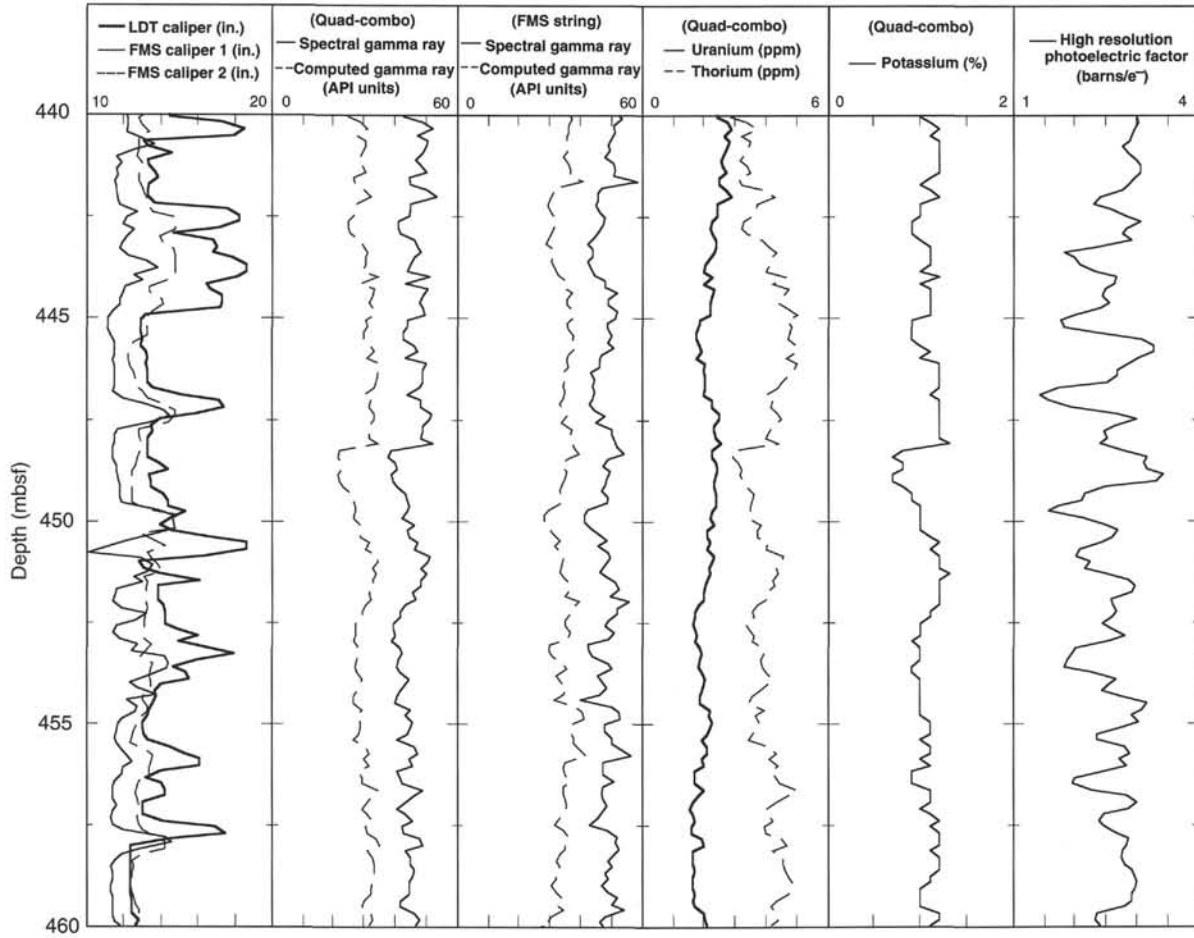


Figure 44. Quad combo, FMS, and MST data plotted at a common scale for Core 977A-48X. This core was selected for presentation because it shows a prominent peak in magnetic susceptibility. The only standard logs that correlate well with the magnetic susceptibility peak are high-resolution bulk density and epithermal neutron porosity. Note that in situ densities are 0.2–0.3 g/cm³ higher than the apparent bulk densities reported by the MST GRAPE instrument.

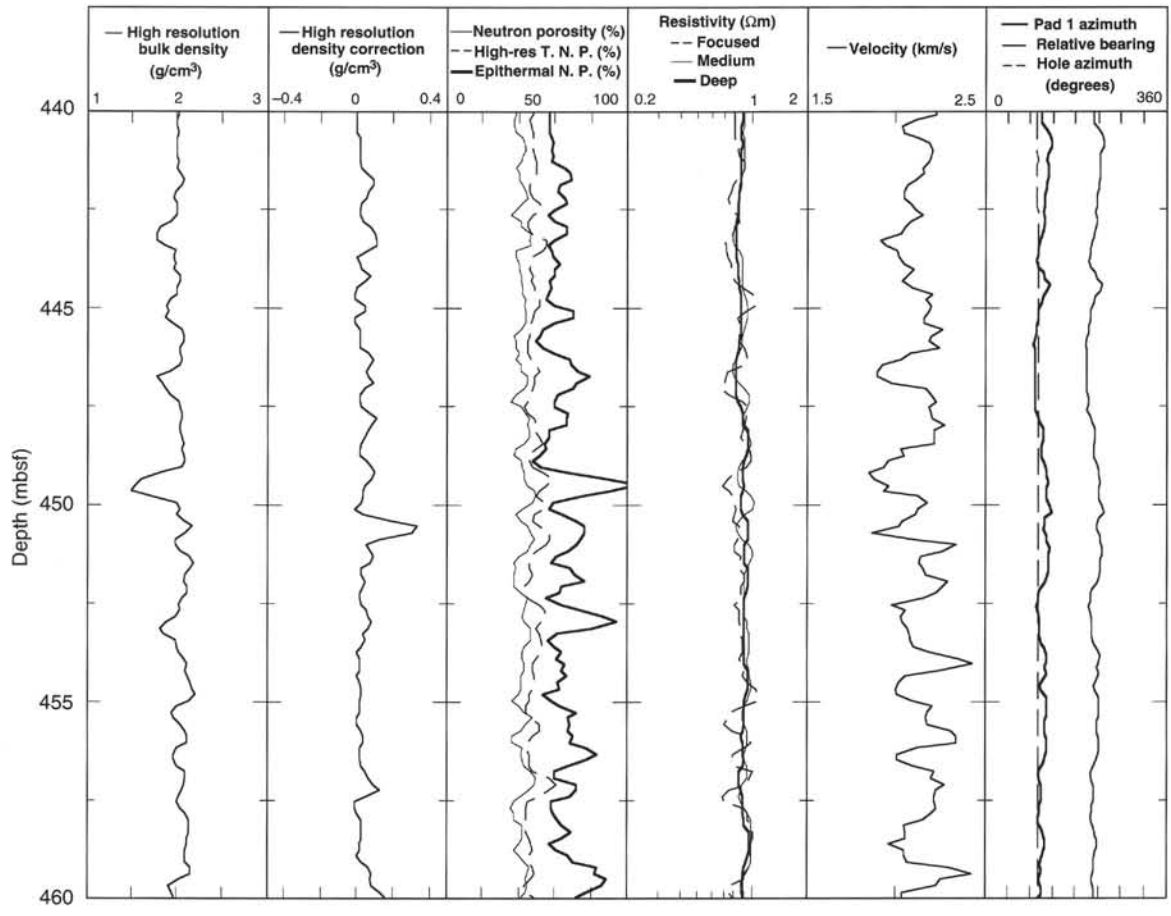


Figure 44 (continued).

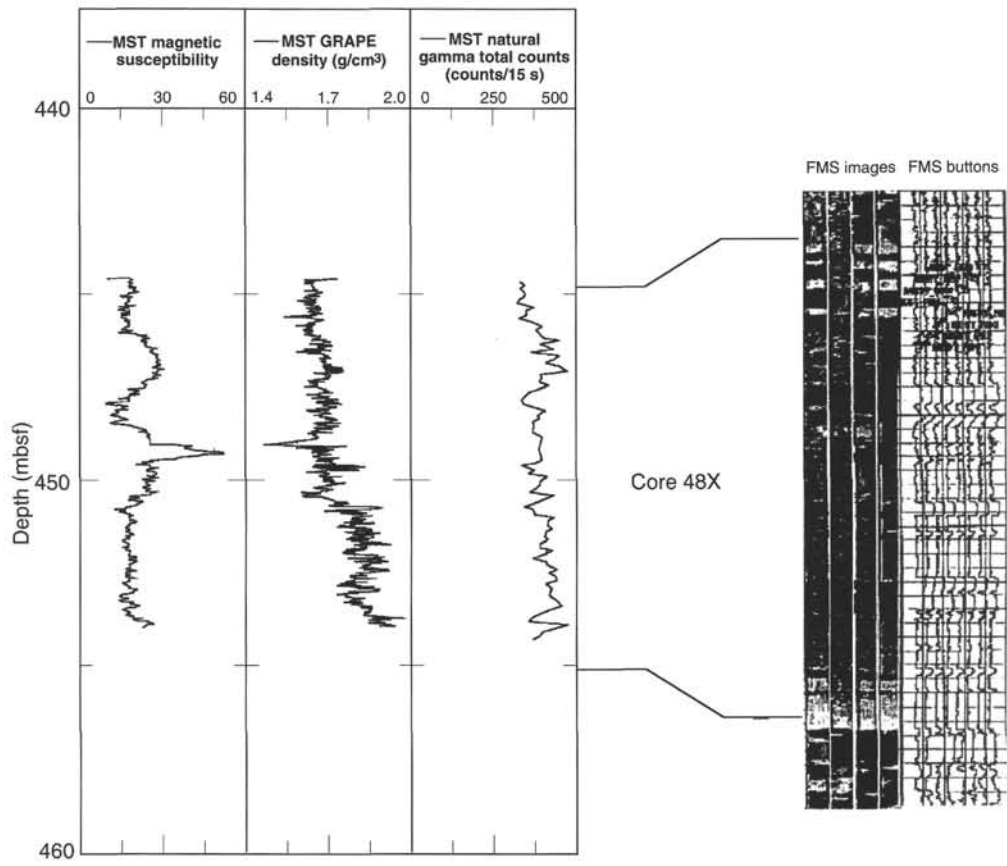


Figure 44 (continued).

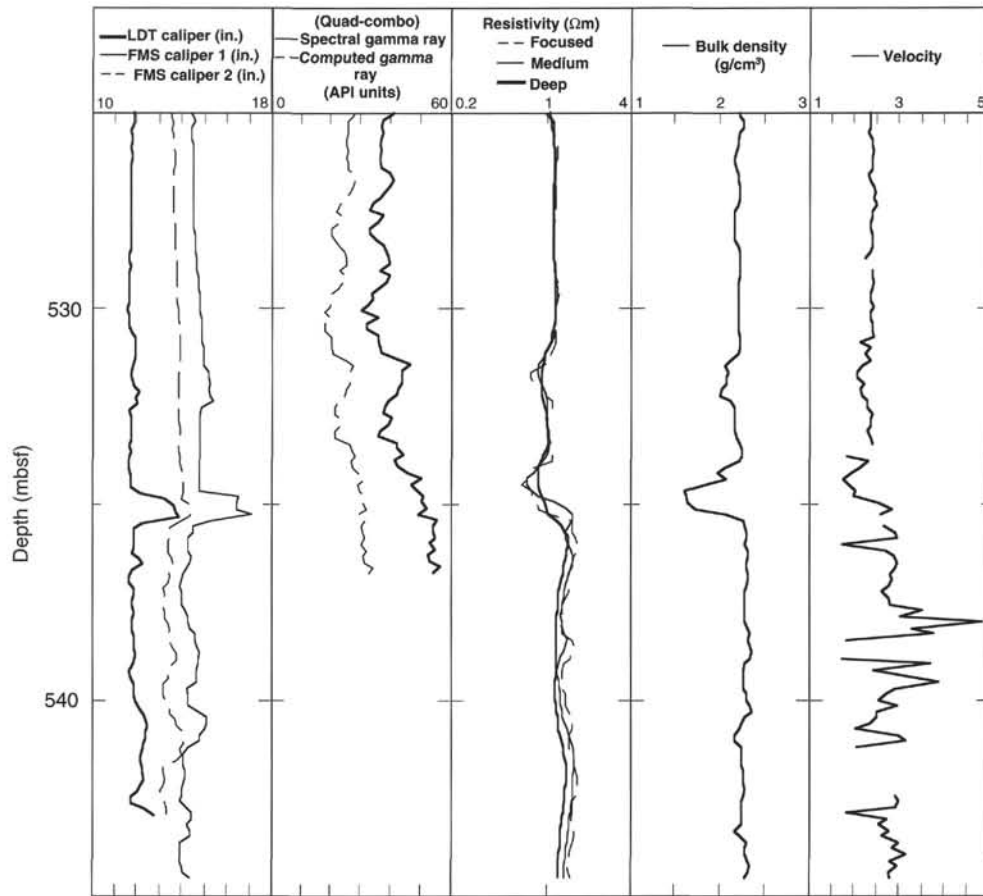


Figure 45. Details of the transition zone between clays and conglomeratic rocks at 535 mbsf. The smooth transition observed in resistivity records is caused by the vertical resolution of the tool. Higher resolution logs, such as the FMS, show that the contact is very sharp. Note the smooth nature of the FMS pad images at the top of the figure in the sediments and the irregular nature of the images at the bottom in the conglomerates.

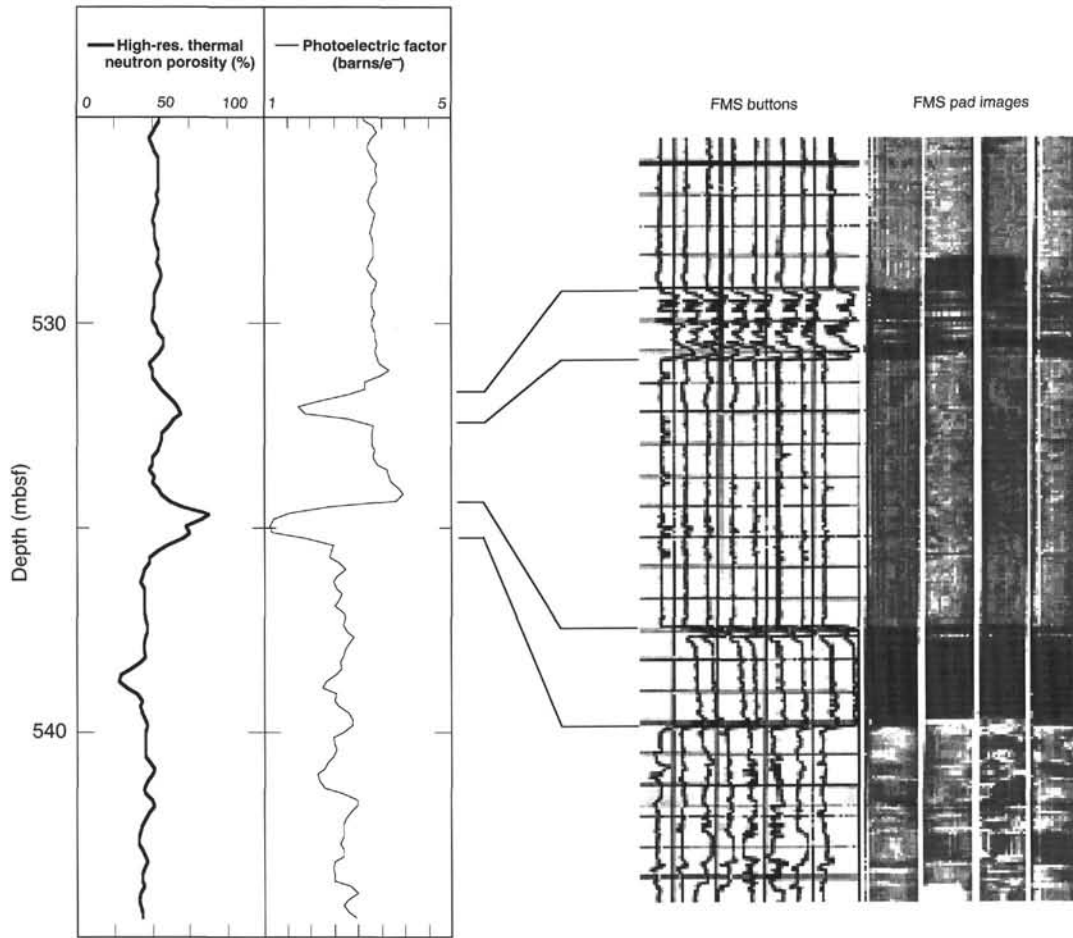


Figure 45 (continued).

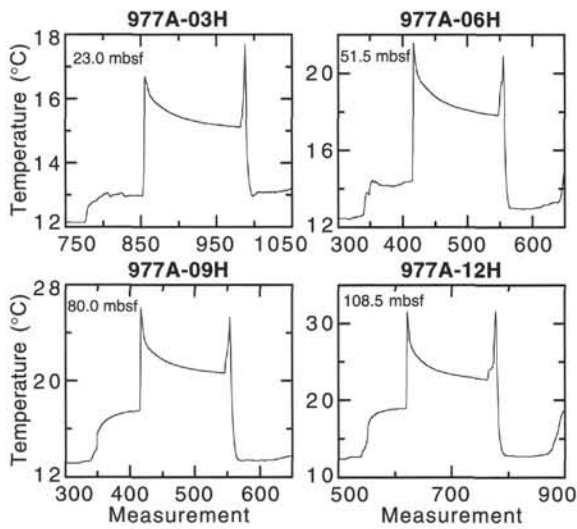


Figure 46. Temperature vs. time for the individual ADARA temperature tool runs at Hole 977A.

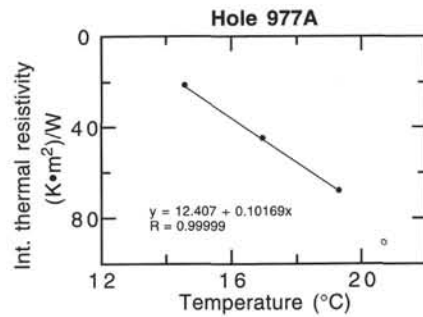


Figure 47. Temperature vs. integrated thermal resistivity for Hole 977A. The best-fitting linear regression to the upper three points is shown by the straight line.

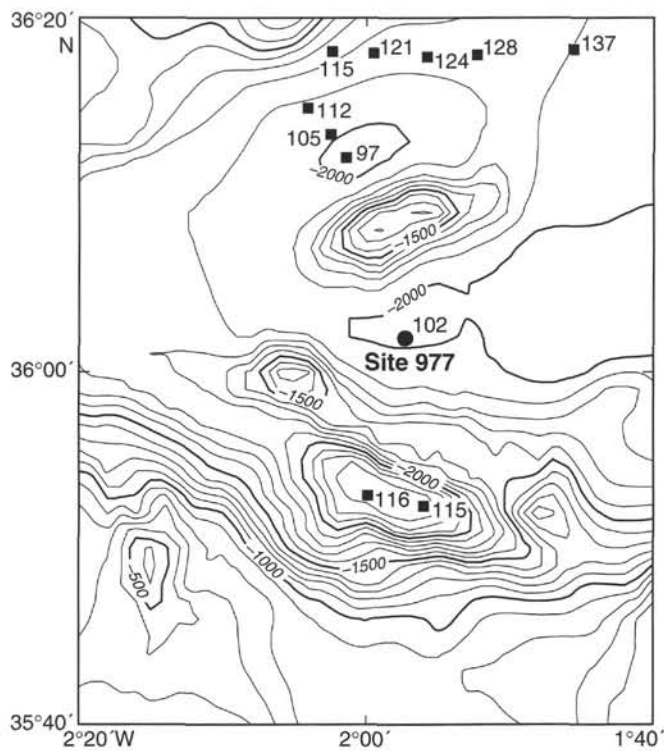


Figure 48. Heat-flow measurements with values in mW/m^2 in the vicinity of Site 977 (shown by the filled circle). Data shown by squares are from Polyak et al. (in press). Bathymetric contours at 100-m intervals.

SHORE-BASED LOG PROCESSING

Hole 977A

Bottom felt: 1995 mbrf (used for depth shift to seafloor)
Total penetration: 598.5 mbsf
Total core recovered: 545.5 m (91.1%)

Logging Runs

Logging String 1: DIT/SDT-LSS/HLDT/CNTG/NGT

Logging String 2: FMS/GPIT/NGT (2 passes)

Wireline heave compensator was used to counter ship heave.

Bottom-Hole Assembly

The following bottom-hole assembly depths are as they appear on the logs after differential depth shift (see "Depth shift" section) and depth shift to the seafloor. As such, there might be a discrepancy with the original depths given by the drillers onboard. Possible reasons for depth discrepancies are ship heave, use of wireline heave compensator, and drill string and/or wireline stretch.

DIT/SDT-LSS/HLDT/CNTG/NGT: Bottom-hole assembly at ~79.5 mbsf.

FMS/GPIT/NGT: Recorded open hole.

Processing

Depth shift: Reference run for depth shift: 2 passes of FMS/GPIT/NGT. All original logs have been interactively depth shifted with reference to the caliper logs from FMS/GPIT/NGT and to the seafloor (-1995 m).

Gamma-ray processing: NGT data have been processed to correct for borehole size and type of drilling fluid.

Acoustic data processing: The array sonic tool was operated in two modes: linear array mode, with the 8-receivers providing full waveform analysis (compressional and shear) and standard depth-derived borehole compensated mode, including long-spacing (8-10-10-12 ft) and short-spacing (3-5-5-7 ft) logs. The long-spacing sonic logs have been processed to eliminate some of the noise and cycle skipping experienced during the recording.

Quality Control

Data recorded through bottom-hole assembly, such as the neutron and gamma-ray data above 80 mbsf, should be used qualitatively only because of the attenuation on the incoming signal.

Hole diameter was recorded by the hydraulic caliper on the HLDT tool (CAL) and on the FMS string (C1 and C2).

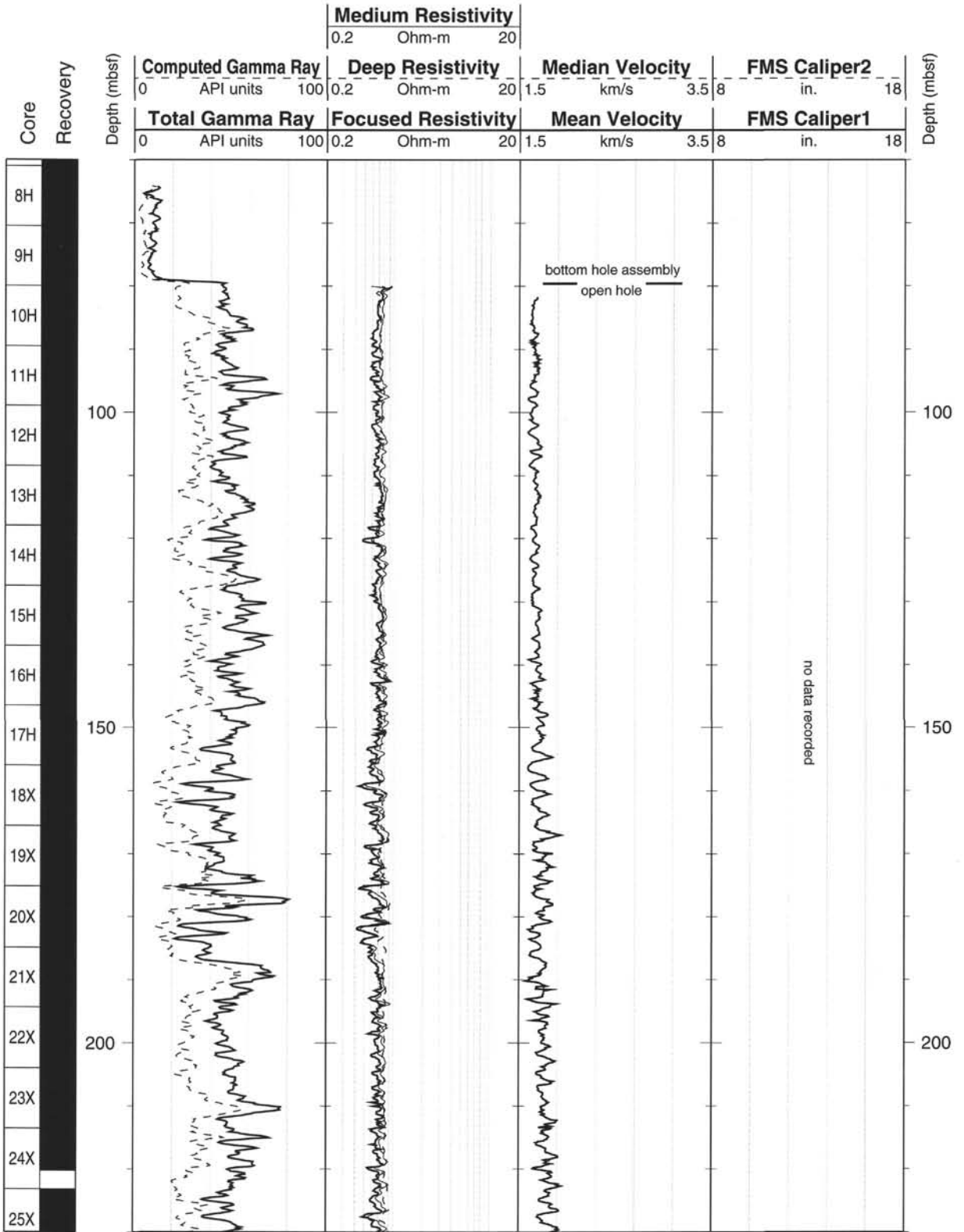
The quality of the density and neutron logs was affected by the very large hole (caliper often saturated at 18.5 in) and by the frequent washouts. The data should be used qualitatively only.

Note: Details of standard shore-based processing procedures are found in the "Explanatory Notes" chapter, this volume. For further information about the logs, please contact:

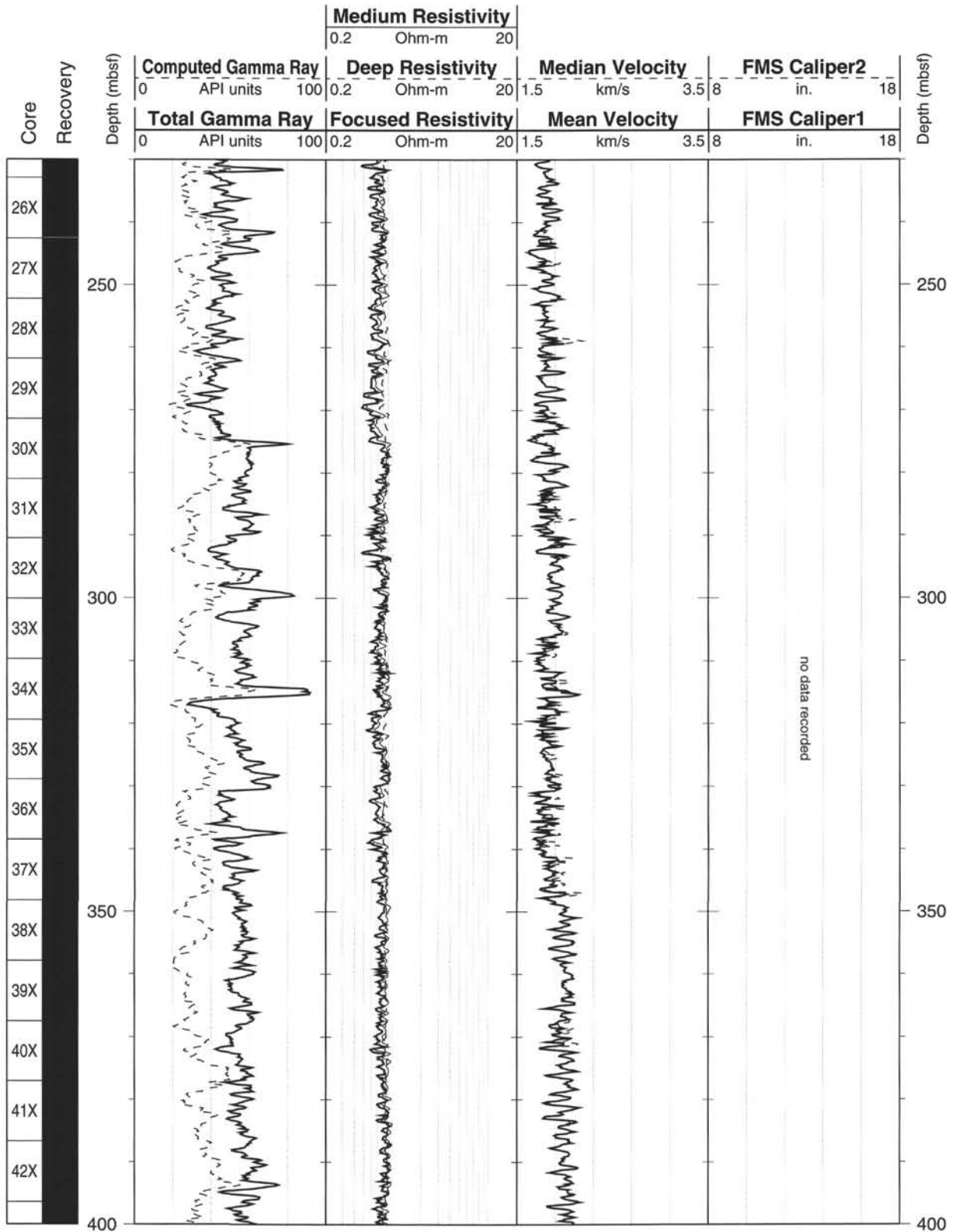
Cristina Broglia
 Phone: 914-365-8343
 Fax: 914-365-3182
 E-mail: chris@ldeo.columbia.edu

Elizabeth Pratson
 Phone: 914-365-8313
 Fax: 914-365-3182
 E-mail: beth@ldeo.columbia.edu

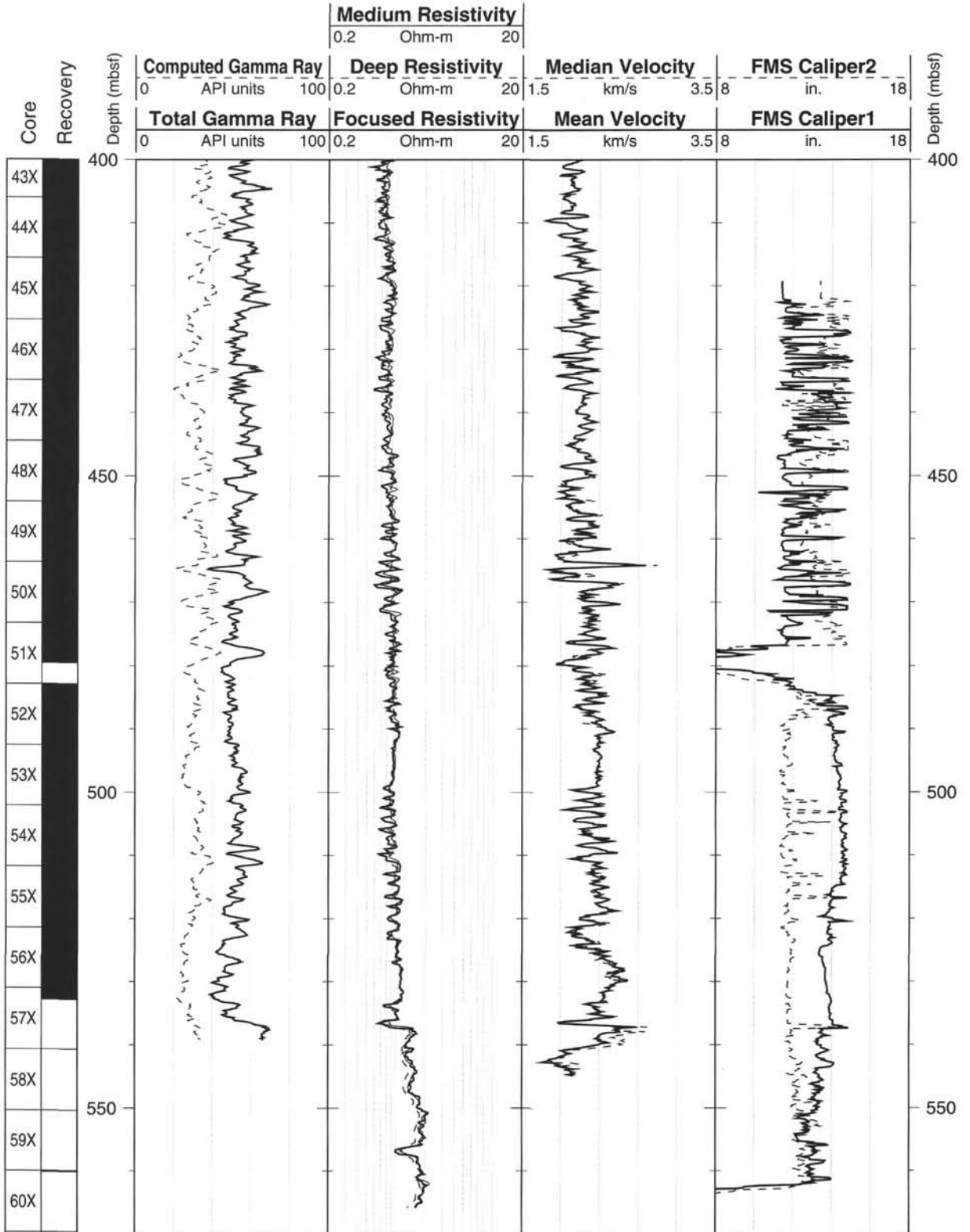
Hole 977A: Natural Gamma Ray-Resistivity-Sonic Logging Data



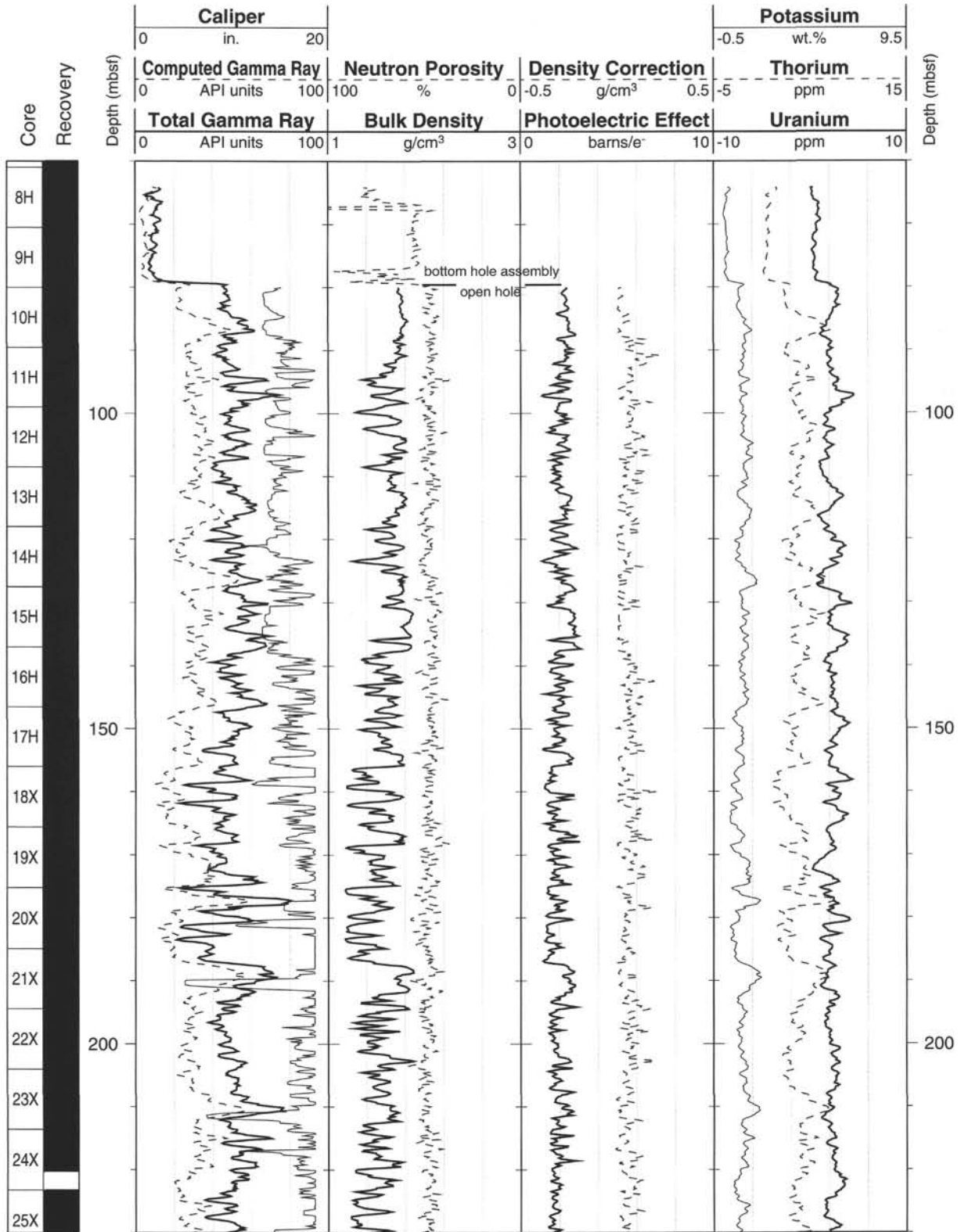
Hole 977A: Natural Gamma Ray-Resistivity-Sonic Logging Data (cont.)



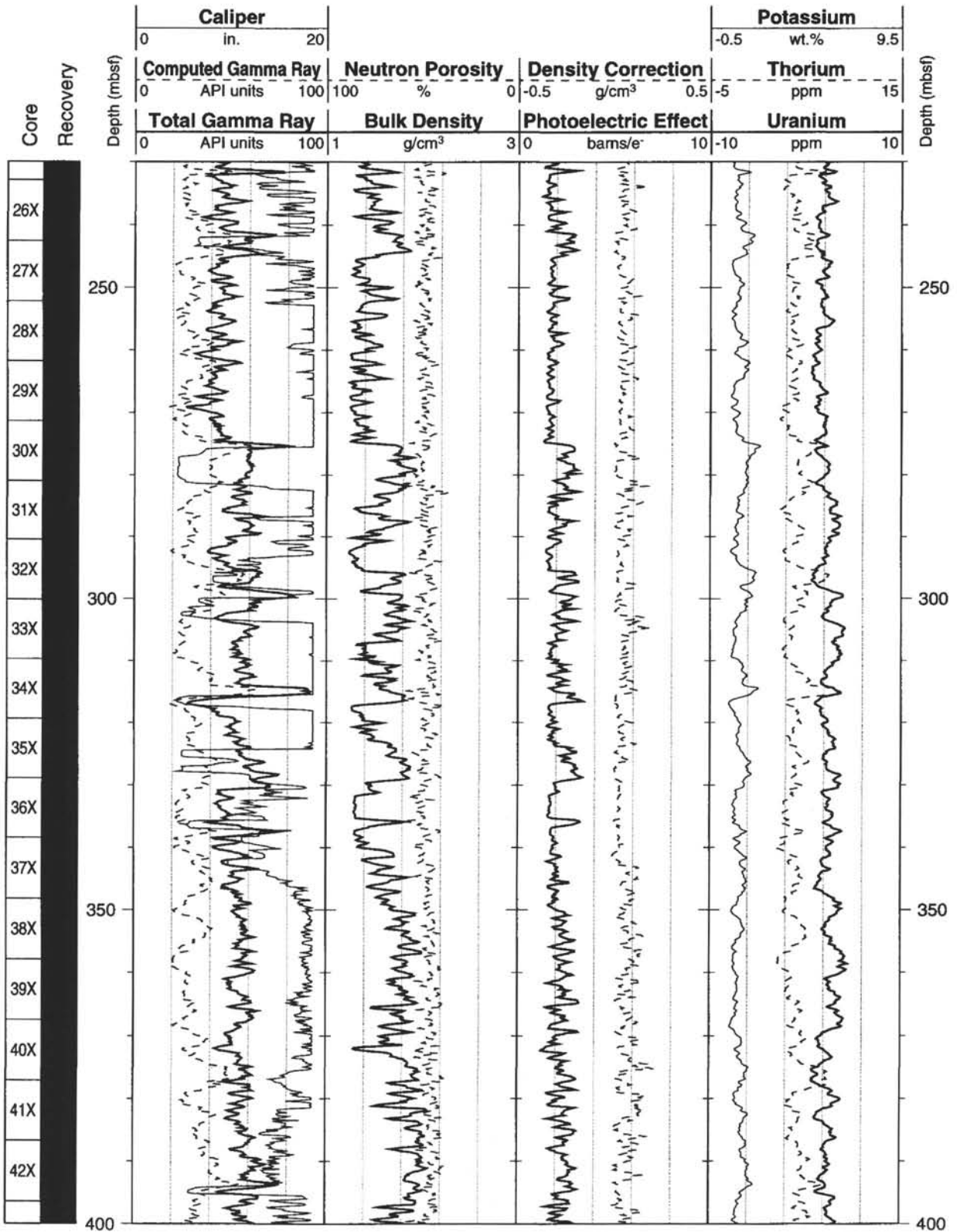
Hole 977A: Natural Gamma Ray-Resistivity-Sonic Logging Data (cont.)



Hole 977A: Natural Gamma Ray-Density-Porosity Logging Data



Hole 977A: Natural Gamma Ray-Density-Porosity Logging Data (cont.)



Hole 977A: Natural Gamma Ray-Density-Porosity Logging Data (cont.)

